TABLE OF CONTENTS

ABSTRACT

It is known experimentally that a jet in forward flight radiates less noise than the same jet in a static environment. At a forward flight Mach number of 0.2, the noise reduction, depending on the jet operating conditions, could be as large as 4-5 dB in the sideline directions. In the past, a way to predict flight effects was to use the method of relative velocity exponent. Another method was to extrapolate measured static jet noise to the flight condition by means of scaling formulas. Both methods are semi-empirical. The fine scale turbulence jet mixing noise theory of Tam and Auriault (AIAA Journal, Vol. 37, No.2, pp. 145-153, 1999) is extended for applications to jets in forward flight. The effect of forward flight on the sources of fine scale turbulent jet mixing noise is also investigated. The noise from the fine scale turbulence of high speed nonaxisymmetric jets is considered. A prediction method is developed by extending the work of Tam and Auriault. A set of improved numerical boundary conditions for use in nonaxisymmetric jet mean flow and turbulence calculations is developed. It is known that nonaxisymmetric mean flow has a significant impact on the radiated noise spectrum and directivity through refraction. In the Tam and Auriault theory, this effect is accounted for by means of the adjoint Green's function. Here the adjoint Green's function method is extended to nonaxisymmetric flows. Extensive comparisons between calculated and experimentally measured jet noise spectra are presented. Good agreements are found. The noise from a jet installed under a wing of an aircraft is considered.

A computational model for prediction of the radiated noise of the installed jet is developed. The parabolized Reynolds Averaged Navier-Stokes (RANS) equations supplemented by the $k - \epsilon$ model developed by Thies and Tam (AIAA Journal, Vol. 34, No.2, pp. 309-316, 1996) are modified and reformulated to compute the installed jet turbulent jet flow. The adjoint Green's function approach is extended to installed jets to include the flow effect and reflection from the wing.

CHAPTER I

INTRODUCTION

Aircraft noise level is highly regulated around most of the world's major airports. For the aircraft industry, before a new type of aircraft is certified, it must meet stringent FAA noise requirements. Needless to say, aircraft noise is currently an important environmental concern. It would be even more so in the future as aircraft traffic increases.

Jet noise is an important component of the total aircraft noise, especially, at take-off. Early experimental studies showed that the acoustic power radiated by high speed jets is a strong function of the intensity of turbulence. Based on such understanding, suppressor nozzles were designed to reduce the overall levels of turbulence by enhancing mixing [1]. However, this type of suppressor nozzle was soon found to cause significant decrease in engine thrust for modest reduction in noise. It then became clear that the only practical way to decrease the noise levels without adversely affecting the performance of the engine was to reduce the jet velocity [2]. This in turn led to the design of turbofan engines. Turbofan engines have larger air intakes, and have a much larger bypass ratio than turbojet engines. As a result, the jet velocity and temperature are lower. This results in higher trust and less noise [3]. Turbofan engines proved to be both more energy efficient and environmentally acceptable than turbojet engines. They have rapidly replaced turbojet engines in most commercial aircraft applications.

Most of the new airplane programs are growth versions of the existing aircrafts. This growth requires more thrust from existing engines. Typically, both primary and secondary velocities are increased and the resultant jet noise is higher. Higher bypass engines are currently being considered on these new airplane programs to reduce jet noise. These new engines are installed quite close to the wing. The proximity of the jet to the wing causes the emission of higher level of noise generally referred to as installation noise. Understanding of the dependence of jet noise on various installation parameters such as engine location, flap settings, etc. is important for controlling and reducing the installed jet noise.

1.1. The Basic Components of Jet Noise

Jet noise is known to consist of three main components : the turbulent mixing noise, the broadband shock-associated noise, and the screech tones [4,5]. The later two components are found only in imperfectly expanded supersonic jets. They are generated by the interaction between the shock cells in the jet plume and the jet turbulence [6,7]. Turbulent mixing noise is generated by the jet turbulence itself, and is present in both subsonic and supersonic jets.

Figure 1.1 is a typical noise spectrum from an imperfectly expanded supersonic jet. The microphone is placed at a 150 deg exhaust angle, measured from the downstream direction. All three noise components contribute to the spectrum with overlapping frequency ranges. However their individual contribution can be easily identified by their spectral characteristics.

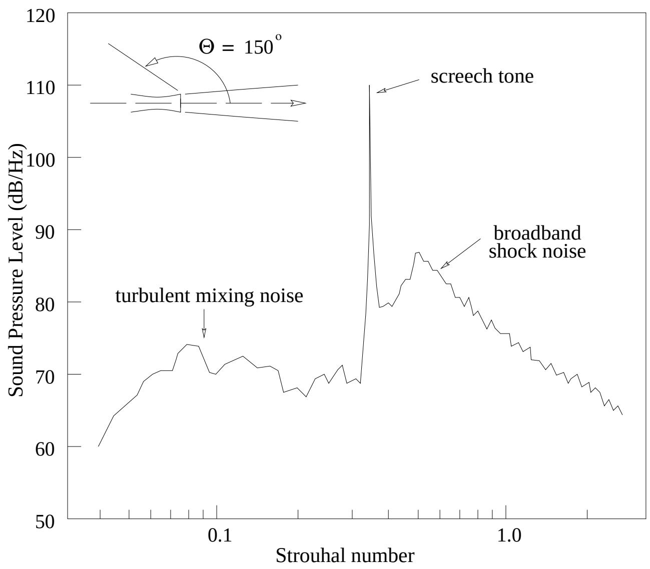

Figure 1.1. A typical far-field noise spectrum of an imperfectly expanded supersonic jet.

The relative intensity of the three noise components is a strong function of the direction of radiation. Shock-associated noise and screech tones are primarily radiated in the upstream direction. On the other hand, turbulent mixing noise is strongest in the downstream direction. Both the intensity and the directivity of jet noise are significantly modified by flight effects.

Present day commercial aircrafts operate at high subsonic Mach numbers. For these jets, turbulence mixing noise is the primary concern of the aircraft designers. It has been the main focus of most of present day jet noise research effort.

1.2. Tam and Auriault Jet Mixing Noise Theory

Jet noise research began in the fifties. Lighthill [8,9] was the first to develop a theory to quantify the source of jet noise. Lighthill used an analogy approach. He rearranged the governing equations for a compressible fluid into a simple wave equation with all the remaining terms put on the right hand side. He argued that since the left side of the equation described acoustic wave propagation, the right side must be the source of noise. He called the terms on the right side quadrupoles. Lighthill's acoustic analogy theory and its extensions by numerous investigators was the principal jet noise theory until the eighties. Because quadrupoles are not physical quantities, they have never been observed experimentally in a turbulent jet. Also quadrupoles are not turbulence quantities. The acoustic analogy theory offers no help or clue as how to reduce jet noise. From the stand point of noise prediction, a model of the quadrupole is needed if one wishes to calculate the radiated far field noise. For this purpose, many models were invented empirically and semi-empirically. Perhaps, because there are no real quadrupoles in a turbulent jet, none of the acoustic analogy theory could offer an accurate prediction of the jet noise spectrum over a reasonable range of Mach numbers and jet temperature ratio. The review article by Lilley [10] offers an in-depth documentation of the approach and results of the acoustic analogy theories for jet noise prediction.

Beginning in the late seventies and early eighties, a totally different approach to develop jet noise prediction theory emerged (see the review articles by Tam [11], [4], [13]). The motivation was that since jet noise was generated by turbulence, one should, therefore, base the formulation of the theory on turbulence and not acoustic wave propagation as Lighthill did. Earlier, the existence of large turbulence structures in jets and free shear flows was discovered by Brown and Roshko [14] and Crow and Champagne [15]. It was recognized that in the case of supersonic jets, the large turbulence structures were very important noise sources. Tam and Burton [16] modeled these large turbulence structures by a superposition of the instability waves of the jet flow. For supersonic jets, the instability waves would be moving downstream at supersonic speed relative to ambient speed of sound. This is very similar to a wavy wall moving supersonically. The result is strong Mach wave radiation in the downstream direction. Since the noise is generated by the large turbulence structures at the edge of the jet, it is not refracted by the jet flow and propagates directly to the far field, as shown in Figure 1.2. A comprehensive mathematical theory of Mach wave radiation generated by the instability waves of jet was developed by Tam and Burton using the method of matched asymptotic expansions. Their computed results were in good agreement with the measurements of Troutt and McLaughlin [17]. The instability waves/large turbulence structures jet noise theory has since been extended by Tam and Chen [18] to the full frequency spectrum for high temperature jets and by Dahl, Papamochou and Hixon [19] to supersonic coaxial jets.

Beginning near the end of the eighties, high quality narrow band jet noise data became available. Previously, all jet noise data were measured in 1/3 octave band. On examining carefully the entire jet noise data bank of the Jet Noise Laboratory of the NASA Langley Research Center (1900 spectra total), Tam, Golebiowski and Seiner [20] found the first definitive experimental evidence that jet mixing noise actually composed of two independent components.

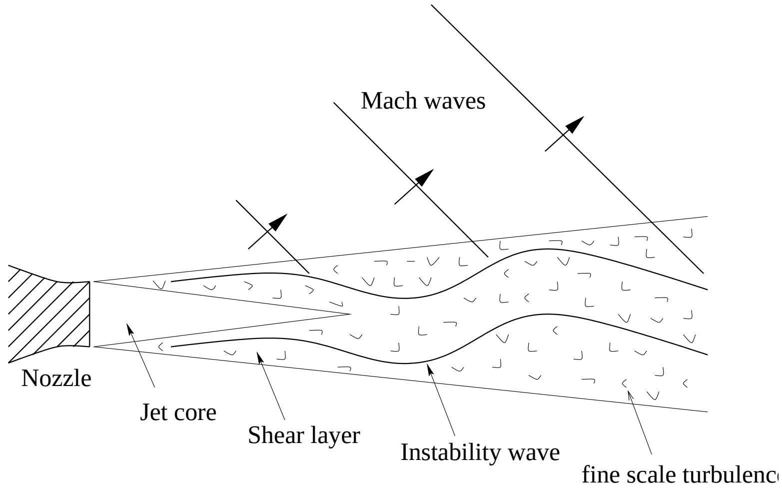

Figure 1.2. Schematic diagram of a jet flow showing Mach wave radiation generated by an instability wave traveling at supersonic phase velocity.

The idea of two independent components of turbulent jet mixing noise was proposed earlier by Tam and Chen [18] based on limited spectral and directivity jet noise data. One component of the noise is generated by the large turbulence structures of the jet flow in the form of Mach wave radiation. This noise component is dominant in the downstream direction. The other component is generated by the fine scale turbulence. This component is dominant in the sideline and upstream direction. Tam, Golebiowski and Seiner were able to identify empirically two self-similar spectra. These two spectra are very remarkable. One spectrum fits all the noise data from the large turbulence structures and the other fits all the noise data from the fine scale turbulence of the jet regardless of the jet Mach number, jet temperature ratio and the direction of radiation. The decomposition of turbulent mixing noise into a small-scale and a large- scale component is illustrated in Figure 1.3. Far-field jet noise spectra from a high speed jet are shown at four angles from the jet axis. The experimental data are from the data-bank of the Jet Noise Laboratory of the NASA Langley Research Center [20]. The similarity spectra of small-scale and large-scale mixing noise from Tam *et al.* [20] are fitted to the experimental data. As can be seen, the 100^o and the 80^o spectra (Figures 1.3a and 1.3b) consist only of small-scale mixing noise. The intensity of that noise increases slightly as the angle is decreased. This can be attributed to the effects of convective amplification. The 50 deg spectrum is made of a superposition of both small-scale and large-scale noise components. At lower radiation angle, the noise is dominated by that of the large turbulence structures. This is illustrated by the 30 deg spectrum. The spectrum fits the self-similarity spectrum of the large turbulence structures found by Tam *et al.* In a more recent work by Tam [21], it was shown that these same spectra also fitted the noise data of supersonic jets from rectangular, elliptic, plug and even suppressor nozzles well. Dahl, Papamochou and Hixon [19] also demonstrated that these spectra fitted the noise spectra from coaxial jets. Most recently, in a comprehensive investigation of subsonic jets, Tam and Zaman [63] showed that these similarity spectra also fitted the spectra from very large aspect ratio rectangular jets, elliptic jets, jets from lobed nozzle and tabbed nozzles well. The implication is that these spectra are far more universal than first believed and that the large turbulence structures and fine scale turbulence of all jets emit noise in a similar manner.

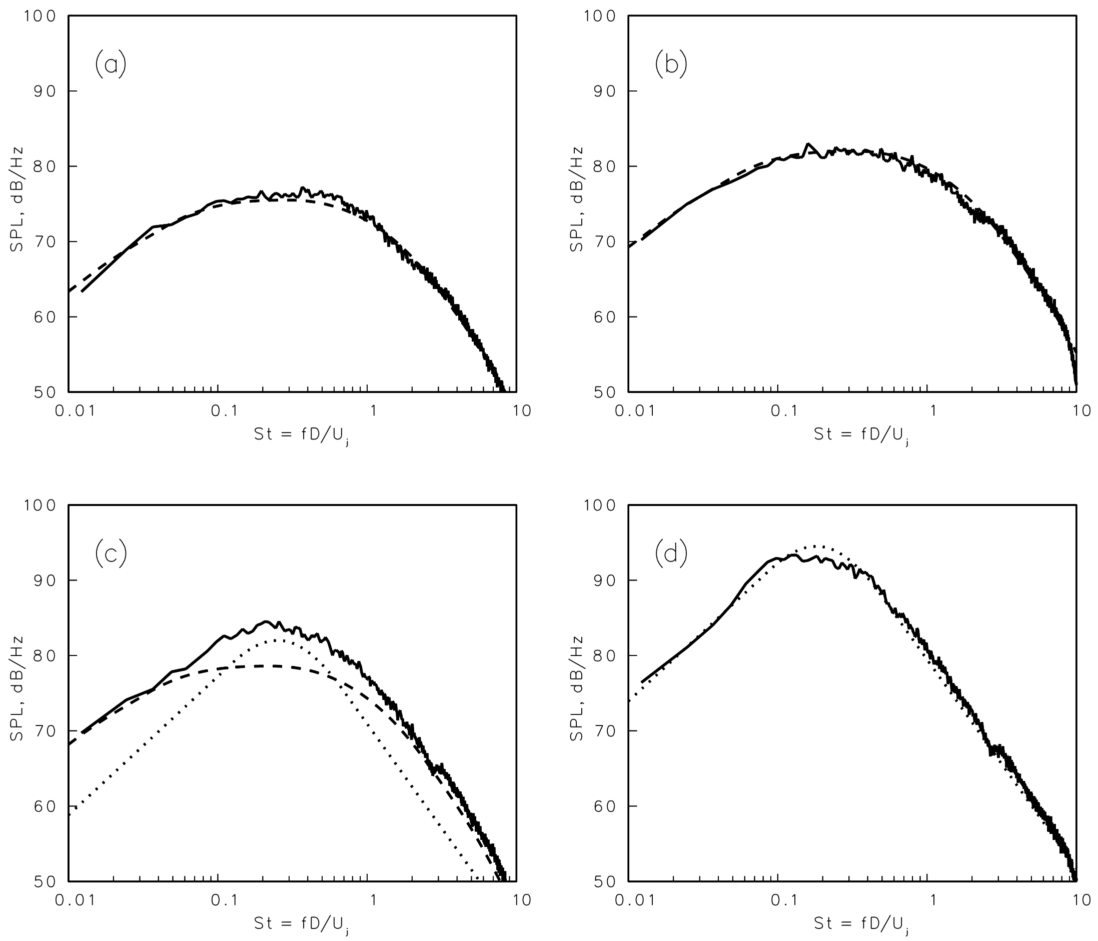

Figure 1.3. Jet noise spectra from a fully expanded Mach 2.0 cold jet measured at four angles from the jet axis, showing the relative contributions of the small-scale and large-scale mixing noise components. (a) $\Theta = 100^o$, (b) $\Theta = 80^o$, (c) $\Theta = 50^o$, (d) $\Theta = 30^o$. ———— : measurements,
· · · · · · · · : similarity spectrum for large-scale mixing noise (from Tam and al.[20]),
– – – – – : similarity spectrum for small-scale mixing noise.

A reliable prediction theory of jet noise from fine scale turbulence was not available until the recent work of Tam and Auriault [23]. Tam and Auriault examined how the kinetic energy of the random velocity fluctuations of a gas contributed to the pressure of the gas in kinetic theory of gases. They reasoned that in a turbulent flow, by analogy, pressure fluctuations can be generated by the time fluctuations of the turbulent kinetic energy of the fine-scale turbulence. The pressure fluctuations would give rise to compression and rarefaction in the fluid medium. This results in acoustic disturbances. Thus, the fluctuation of turbulence kinetic energy is the source of turbulent mixing noise in a jet. In nearly equilibrium flows, such as jets, the fluctuating part of the turbulence kinetic energy would scale with the time independent part. This allows one to use the $k - \epsilon$ model to provide the necessary turbulence information, for example, intensity, length, and timescales needed for noise prediction.

In the Tam and Auriault theory, a number of steps have to be carried out before the radiated noise can be calculated. The first major task is to calculate the mean flow and turbulence quantities through the $k-\epsilon$ model. The constants of the $k - \epsilon$ model are, however, not those of the standard model. Tam and Auriault chose to adopt the values suggested by Thies and Tam [24]. Thies and Tam observed that because the large turbulence structures of a flow having dimensions comparable to the mean flow would likely be affected by the the flow geometry and boundary conditions. Their dynamics and characteristics are, therefore, flow specific. In other words, the large scale turbulence is not universal. The constants of the standard model were calibrated by data from low speed boundary layer and two-dimensional mixing layers. Thus they are not necessarily suitable for high speed jets. Indeed, past attempts to use the standard model to predict jet mean flow profiles did not give satisfactory results. Thies and Tam, then, suggested that if one restricted one's consideration to a specific class of flows with similar characteristics, such as jet flows alone, it would be reasonable to expect a single set of constants to work for all the flows within the class. They recalibrated the constants for jet flows using a large data base.

As the sound waves propagate through the jet, refraction takes place due to the velocity and density gradient of the mean flow. The second task is to determine the mean flow refraction effect using the mean flow found in step one. In Tam and Auriault's work, this is done by the use of the adjoint Green's function following the method of ref. [25].

The fine scale turbulence is convected downstream by the jet flow. Thus the problem involves moving sources. It can be shown that moving sources tend to radiate more sound in the direction of motion [10]. This source convection effect is incorporated into the theory automatically through the use of the two-point space-time correlation function of the kinetic energy of the fine-scale turbulence. The third task is to determine the radiated noise spectrum by the use of a model two-point space-time correlation function. In this way, the following formulas for the far-field noise spectrum, $S(R, \Theta, \phi, fD_j/u_j)$, in decibel per Strouhal number (fD_j/u_j) are derived:

$$S(R, \Theta, \phi, \frac{fD_j}{u_j}) = 10\log\left[\frac{4\pi\hat{S}(R, \Theta, \phi, \omega)}{p_{ref}^2(D_j/u_j)}\right] \tag{1.1}$$

where

$$\hat{S}(R,\Theta,\phi,\omega) = 4\pi\left(\frac{\pi}{ln2}\right)^{\frac{3}{2}} \int\int\int_{-\infty}^{+\infty} \frac{\hat{q}_s^2 l^3{}_s}{c^2\tau_s} \frac{|p_a(\mathbf{x_2},\mathbf{x},\omega)|^2 e^{-\frac{\omega^2 l^2{}_s}{\overline{u}^2(4ln2)}}}{[1+\omega^2\tau_s{}^2(1-\frac{\overline{u}}{a_\infty}cos\Theta)^2]} d\mathbf{x_2} \tag{1.2}$$

Equations (1.1) and (1.2) are equations (35) and (36) of ref. [23]. Here $\mathbf{x_2}$ is the source point, and $\mathbf{x}$ is the far-field measurement point with spherical coordinates (R,Θ,ϕ). The spherical coordinate system is centered at the nozzle exit with the polar axis in the direction of the flow. Θ is the polar angle, and ϕ is the azimuthal angle. Also $\omega = 2\pi f$ is the angular frequency, and p_{ref} is the reference pressure for the decibel scale. D_j and u_j are the fully expanded jet diameter and velocity, respectively, and fD_j/u_j is the Strouhal number, $\bar{u}$ is the mean flow velocity at $\mathbf{x_2}$ and a_∞ is the ambient speed of sound. Here $p_a(\mathbf{x_2},\mathbf{x},\omega)$ is the adjoint Green's function (see ref. [25]). Equation (1.2) contains a number of turbulence quantities including $\hat{q}_s^2$, the fine-scale turbulence intensity; l_s, the eddy size; and τ_s, the eddy decay time. They are related to k, the turbulence kinetic energy, and ϵ, the dissipation rate, of the $k-\epsilon$ turbulence model as follows:

$$l_s = c_l l = c_l \frac{k^{3/2}}{\epsilon}, \qquad \tau_s = c_\tau \tau = c_\tau \frac{k}{\epsilon} \tag{1.3}$$

$$\frac{\hat{q}_s^2}{c^2} = A^2 q^2, \qquad q = \frac{2}{3}\bar{\rho}k \tag{1.4}$$

where $\bar{\rho}$ is the density of the jet mean flow at $\mathbf{x_2}$ and c_l and c_τ, and A are the three empirical constants of the theory. Their numerical values are

$$c_l = 0.256, \qquad c_\tau = 0.233, \qquad A = 0.755 \tag{1.5}$$

Aside from the inherent empirical constants of the $k-\epsilon$ model, the theory contains three empirical constants of its own, c_l, c_τ, and A. Two of these constants, c_l and

c_τ are used to establish the length and time scales of the fine scale turbulence. The turbulence kinetic energy computed by the $k - \epsilon$ model includes both the large and fine scale turbulence of the jet. The third constant, A, effectively assigns the proper fraction of the turbulence kinetic energy k to the fine scale turbulence. Thus the theory together with the $k - \epsilon$ model code form a self-contained noise prediction method. Tam and Auriault tested the prediction of their theory against four sets of jet noise data ranging from Mach 0.3 to 2.0. It is worthwile to point out that the sound pressure level (SPL) of a Mach 2.0 jet is about 60 dB higher than that of a Mach 0.3 jet. So the experimental data covers a very large range of sound pressure level. Excellent agreements are found not only in the shape of the noise spectra but also in the intensities and directivities. Tam and Auriault also compared the calculated noise spectra with hot supersonic jet noise data at Mach 1.5 and 2.0. The temperature ratio of the data varied from 1.0 to 4.9. This parameter range brackets the operating conditions of all commercial jet engines. Good agreements were again found. It is fair to say, there is now a theory capable of predicting accurately the noise of a simple circular jet over a wide range of jet operating conditions.

1.3. Scope of this Work

It has been known experimentally, since the late seventies, that a jet installed under a wing of an aircraft radiates more noise than the same jet in a stand-alone condition. The excess noise is the airframe-jet engine interaction noise, commonly referred to as the installation noise. When a jet is placed near a wing, there will be an increase in noise in the fly-over directions because of the reflection of sound by the wing. Here, installation noise includes not merely the noise increase due to the reflection of sound by the wing. The major part of this noise is generated aerodynamically by the nonlinear interaction between the flow around the wing/flap and the jet. Installation noise can increase substantially the total aircraft noise in the fly-over plane as well as in the sideline directions. It is especially important at landings when the flaps are down.

During the eighties, a number of experiments were carried out trying to quantify the characteristics and intensity of this airframe noise component [26], [27], [28]. Most of these experiments involved the measurements of the jet alone noise and the noise when the jet was placed near a model of an aircraft wing inside an anechoic chamber. The experimental measurements by Wang [27] were the most systematic. In his experiment a scaled model of the wing of a DC-10 aircraft was used. Noise increase as much as 12 dB was observed in the fly-over plane in the low frequency part of the spectrum. The increase in high frequency noise was less. In directions at small exhaust angles, the installation noise intensity was quite low. In the sideline planes, the radiated noise characteristics, on the other hand, were quite different. Overall, the measured data indicated that installation noise had a unique spectral shape and a directional pattern of its own.

Recently, there is a renewed interest in airframe-jet engine interaction noise in this country and abroad. In the United Kingdom, Mead & Strange [29] investigated the under-the-wing installation effects on jet noise with special emphasis on the sideline directions. Their interest in the sideline was motivated by the experience that it is generally more difficult to meet the legislative limit on sideline noise level requirements. They reported the measurement of installation noise level as high as 9 dB in the low frequency range.

One drawback of the Mead & Strange [29] experiment as well as most of the previous works is that the experiments were carried out in static conditions. Upon realizing that the effect of forward flight is extremely important in the interaction between the flow around the wing/flap and the jet, a series of new experiments on installation noise was conducted by engineers of the Boeing Company; Shivashankara & Blackner [30], Blackner & Bhat [31], [32]. They employed an open wind tunnel at M = 0.28 to simulate the forward motion of the aircraft. By using elliptic mirror microphones and the newly developed phase array microphones, they were able to obtain noise source location maps as well as far field noise data.

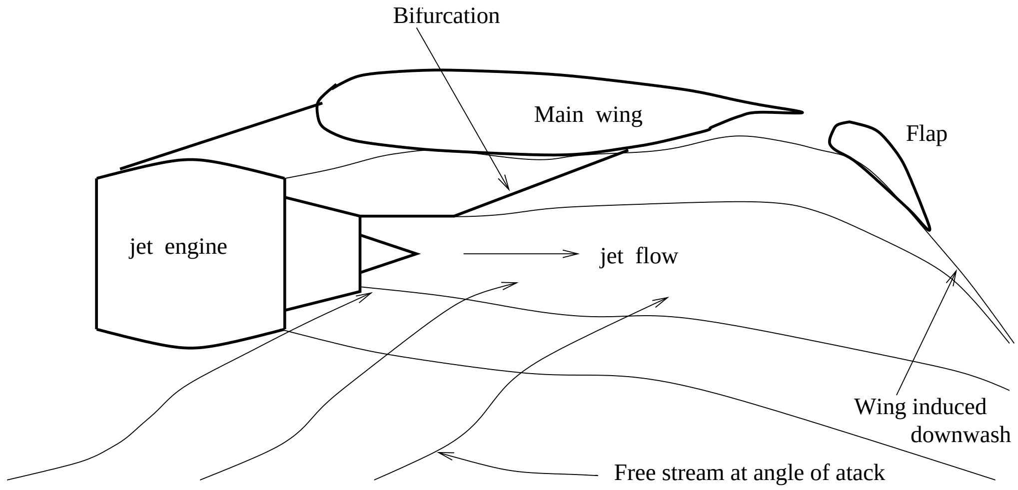

Figure 1.4. Geometry of the airframe and installed jet engine of the Boeing experiment [31], [32].

In the Boeing study, the variation and sensitivity of installation noise to a range of flow parameters, wing/flap settings, jet engine location and pitching angle were investigated. Figure 1.4 shows the geometry of the airframe and the installed jet engine of the experiments. Installation noise up to 6 dB across a wide band of frequency was measured. This is a very large increase in noise. It can easily negate the gains of recent successes in suppressing the other components of airframe noise.

Below is a summary of the important findings of the Boeing investigation.

1. The presence of the airframe increases jet noise significantly.

2. The noise increase follows monotonically with increasing flap deflection. Flap deflection has the largest effect on installation noise.

3. Noise levels are insensitive to engine installation location within Boeing's current envelope of possibilities at takeoff flap setting.

4. A wide bifurcation can contribute to a slight increase in noise level.

5. Pitching the nozzle up toward the wing can increase the noise levels, while pitching the nozzle away from the wing has little benefit.

Although airframe-jet engine integration noise has been recognized as an important airframe noise component for some time yet, even now, there is little basic understanding of the physical processes that are responsible for its generation. A better understanding of the fluid and turbulence physics involved in the nonlinear interaction between the wing/flap flow and the jet flow is essential to the development of an effective noise reduction scheme/strategy or device as well as a more accurate and less empirical noise prediction method.

We believe that there are two principal mechanisms responsible for the generation of the airframe-jet engine integration noise. Both mechanisms are important, the basis of these mechanisms is discussed below.

(a) Reduction of the forward flight effect

It is well known that a static jet emits more noise than the same jet in forward flight. The reason is quite simple. When a jet is in forward motion the velocity gradient across the mixing layer of the jet is reduced. This, in turn, reduces the turbulence intensity in the mixing layer of the jet, leading to a decrease in the noise radiated. Experimentally, a noise reduction of about 4 dB across the entire noise spectrum can be realized at typical takeoff or landing speed.

Now when a jet is installed under a wing, the presence of the wing, inevitably, slows down the velocity of the fluid surrounding the jet in the nozzle fixed frame of reference. This is especially so when the flaps are fully extended. Because of this, the effective forward flight speed is reduced resulting in a reduction of the beneficial effect of forward flight on jet noise. Physically, the turbulence level in the mixing layer of the jet increases relative to that of an isolated jet in flight. This increase leads to the emission of a higher level of jet noise.

(b) Distortion of the jet flow by the presence of the airframe

The flow around the wing/flap especially at large flap deflection angle creates steep velocity gradients and downwash below the wing and, in particular, downstream of the trailing edge of the flap. These steep gradients cause severe distortion of the jet flow. The cross-section of the jet is no longer circular nor symmetric but highly distorted as observed in the Boeing experiments by Blackner & Bhat [31], [32]. The large distortion leads to the generation of additional fine-scale turbulence and hence noise.

Shivashankara & Blackner [30] used elliptic mirror microphones to measure the distribution of jet noise sources for an isolated jet as well as an installed jet.

Their data show a large increase in jet noise source intensity directly below and downstream of the trailing edge of the wing/flap system. These observations are consistent and supportive of the jet flow distortion noise enhancement mechanism.

The purpose of this investigation is the development of a mathematical/computational model of the nonlinear interaction between the flow around the wing/flap and the jet flow. A brute force numerical computation of the combined wing/flap and the jet flow is not feasible because of the large number of mesh points required for adequate numerical resolution. Also, such an attempt will not be able to provide fine-scale turbulence information necessary for noise calculation. The proposed model divides the problem into two parts, namely, the wing/flap flow and the jet flow. The division allows a clear identification of the interaction of the two parts. It also allows the application of the recently developed fine-scale turbulence noise theory of Tam and Auriault [23] to the jet flow for computation of the radiated noise.

The proposed interaction model consists of first calculating the flow due to forward flight. This wing/flap flow is a good representation of the flow field surrounding the jet flow. Next, the jet flow is recomputed (with the $k-\epsilon$ turbulence model) using the wing/flap flow as the boundary condition outside the jet. In this way, the velocity gradients due to the downwash of the flow around the wing and the flap is incorporated into the flow and turbulence field of the jet. The jet is distorted by the imposed boundary conditions. Finally, the turbulence field (the k and the ϵ values) of the distorted jet will be used as an input into the fine-scale turbulence noise theory of Tam and Auriault to find the radiated noise of the installed jet. To develop the computation model, the following tasks will be carried out. In Chapter 2, the computational model of Thies and Tam [29] is extended, without any modification of the constants, to include forward flight effects. The Tam and Auriault [23] theory is used to predict the noise of high-speed jets in simulated forward flight. In Chapter 3, the theory of Tam and Auriault [23] is extended to predict the noise from the fine-scale turbulence of high-speed nonaxisymmetric jets. In Chapter 4, the flow around the wing/flap is calculated using the method of ref. [33]. In this chapter the governing equations used in Chapter 1 are modified and reformulated to compute the turbulent jet flow with the wing/flap flow as the boundary condition outside the jet. To predict the noise from installed jet, the fine-scale turbulence noise theory from Chapter 3 is extended further to include forward flight and reflection from the wing effects. Finally, a summary and conclusions of this work are given in Chapter 5.

CHAPTER II

THE EFFECTS OF FORWARD FLIGHT ON JET MIXING NOISE

Experimentally, it has been found that a jet in forward flight emits less noise than the same jet in a static environment. The decrease in noise intensity is quite substantial. For instance, at forward flight Mach number 0.2, there is a drop of 4-5 dB in the noise radiated to the sideline.

The standard practice to quantify the effect of forward flight on jet noise in a laboratory is to put the jet inside an open wind tunnel and measure the emitted noise by microphones mounted outside as shown in Figure 2.1. In this arrangement, the flow around the jet will be the same as that in actual forward flight viewed from the nozzle-fixed coordinate. In the literature, such data are referred to as simulated forward flight measurements. [34-37]. During the 1970s and early 1980s, two methods were established for predicting the effects of forward flight on the noise of high-speed jets. Both were semi-empirical methods. One method used was the so-called relative velocity exponent [38], [39] whereby the noise intensity was taken to be proportional to a high power of the relative velocity between the jet and the outside flow. The velocity exponent was found empirically. The other was a scaling method [40], [41]. In this case, the measured noise of a static jet was extrapolated to the forward flight condition by semi-empirical formulas.

In this chapter, the Tam and Auriault theory [23] is extended, without any modification of the constants, to the flow configurations of a high-speed jet in an open wind tunnel to determine the effects of forward flight on jet mixing noise. Because the theory as used involves no additional adjustable constants, the calculated jet noise spectra in simulated forward flight may be regarded as absolute predictions, i.e. both amplitude and spectral characteristics of the far field noise can be predicted.

Another objective of this investigation is to study the effects of forward flight on the sources of fine-scale jet mixing noise. Of particular interest are the noise intensity and location. Information of this kind is useful for noise suppression purposes.

2.1. Open Wind Tunnel Simulation of Forward Flight

Forward flight effects on jet noise may be assessed by outdoor flyover measurements. However, such experiments are expensive and difficult to control. To provide a controllable and repeatable experimental environment, most forward flight experiments are done using an open wind tunnel inside an anechoic chamber. The jet is mounted in the potential core of the wind tunnel. Far-field microphones are placed outside the wind-tunnel flow, as showed in Figure 2.1. By measuring the jet noise with and without the wind-tunnel flow on, one can obtain quantitative changes in jet mixing noise due to forward flight. In the nozzle-fixed coordinate system, the flow around the jet in a simulated forward flight experiment is no different from that of the jet in actual flight. In terms of possible source modification by the ambient flow, the flow physics is completely reproduced in a simulated forward flight experiment. Because of the presence of an outer shear layer surrounding the open wind tunnel, the mean flow refraction effect, however, is not the same. This difference should be borne in mind when interpreting the measured or computed data.

Note that one advantage of using the adjoint Green's function method to calculate the noise of jets in simulated forward flight is that the refraction effect of the outer shear layer of the open wind tunnel is automatically included in the computation. No (traditional) shear layer correction is needed.

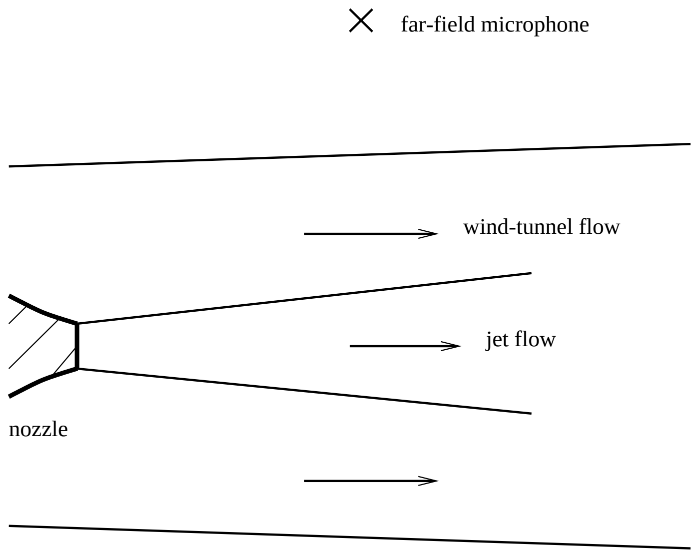

Figure 2.1. Open wind-tunnel simulation set-up.

2.2. Mathematical Model for Forward Flight Effects

In this work, the Tam and Auriault [23] jet mixing noise theory is extended for the open wind-tunnel simulated forward flight flow configuration. The first step of the theory involves the prediction of the jet mean flow and the basic turbulence quantities. This is carried out using the algorithm and computer code of Thies and Tam [29]. In their work, Thies and Tam made extensive comparisons with experimental data for isolated jets, however they didn't consider jets in forward flight and coaxial jets. The second task is to determine the mean flow refraction effect using the mean flow found in step one. In this work, this is done by the use of the adjoint Green's function following the method of Ref. [18]. The third task is to determine the radiated noise spectrum by the use of a model two-point space-time correlation function of the time fluctuation of the kinetic energy of the fine-scale turbulence. The far-field noise spectrum is given by the equations (1.1) and (1.2).

2.3. Jet Exit Conditions

In the work of Tam and Auriault [23], the mean flow of the jet as well as the values of k and ϵ are calculated by a parabolized spatial marching algorithm developed by Thies and Tam [29]. The marching algorithm uses the the Dispersion-Relation-Preserving (DRP) scheme [42] and starts the computation at the nozzle exit plane. To initialize the computation, the velocity and temperature profiles at the nozzle exit plane must be given. In all of the present computations, the velocity and temperature profiles of Figures 2.2 and 2.3 are used as initial condition.

Figure 2.2 shows the radial profile of the jet exit velocity. In Figure 2.2, r is the radial coordinate of a cylindrical coordinate system centered at the nozzle exit. The jet exit velocity is u_j, the open wind tunnel velocity is u_f, and the radius of the uniform core region of the jet is r_j. The uniform core region of the open wind tunnel extends from $r = r_3$ to r_4. Between the two core regions is the wake region formed just downstream of the nozzle lip. The minimum velocity is u_e, which may be equal to zero, at r_2. Analytically, the mean flow profile $\bar{u}(r)$ is assumed to have the form

$$\bar{u} = \begin{cases} u_j, & r \leq r_1 \\ u_1 + (u_j - u_1)\exp\{-(\ln 2)[(r - r_1)/b_1]^2\}, & r_1 \leq r \leq r_2 \\ u_2 + (u_f - u_2)\exp\{-(\ln 2)[(r - r_3)/b_2]^2\}, & r_2 \leq r \leq r_3 \\ u_f, & r_3 \leq r \leq r_4 \\ u_f\exp\{-(\ln 2)[(r - r_4)/b_3]^2\}, & r_4 \leq r \end{cases} \tag{2.1}$$

where

$$u_1 = \frac{u_l - u_j\exp\{-(\ln 2)[(r_2 - r_1)/b_1]^2\}}{1 - \exp\{-(\ln 2)[(r_2 - r_1)/b_1]^2\}}$$

$$u_2 = \frac{u_l - u_f\exp\{-(\ln 2)[(r_2 - r_3)/b_2]^2\}}{1 - \exp\{-(\ln 2)[(r_2 - r_3)/b_2]^2\}}$$

Velocity profile (2.1) is characterized by the parameters $r_1, r_2, r_3, r_4, b_1, b_2, b_3$, and u_e, in addition to u_j and u_f. These parameters are chosen such that computed data fit best to the measured velocity profile at the first station near the nozzle exit. The computation will continue downstream without further adjustment. Typically, $r_1 = 0.485D, b_1 = b_2 = 0.015D$, where D is the inner nozzle diameter. r_4 is the radius of the wind tunnel used in the experiment and b_3 is typically 2% of r_4.

Figure 2.3 is the radial profile of jet temperature at the nozzle exit plane. T_j, T_f , and T_a are the jet, the wind tunnel, and the ambient temperature, respectively. The analytical form of the temperature profile used in the computation is

$$T = \begin{cases} T_j, & r \leq r_1 \\ T_1 + (T_f - T_1)\exp\{-(\ln 2)[(r_3 - r)/b_1]^2\}, & r_1 \leq r \leq r_3 \\ T_f, & r_3 \leq r \leq r_4 \\ T_a + (T_f - T_a)\exp\{-(\ln 2)[(r - r_4)/b_2]^2\}, & r_4 \leq r \end{cases} \tag{2.2}$$

where

$$T_1 = \frac{T_j - T_f\exp\{-(\ln 2)[(r_3 - r_1)/b_1]^2\}}{1 - \exp\{-(\ln 2)[(r_3 - r_1)/b_1]^2\}}$$

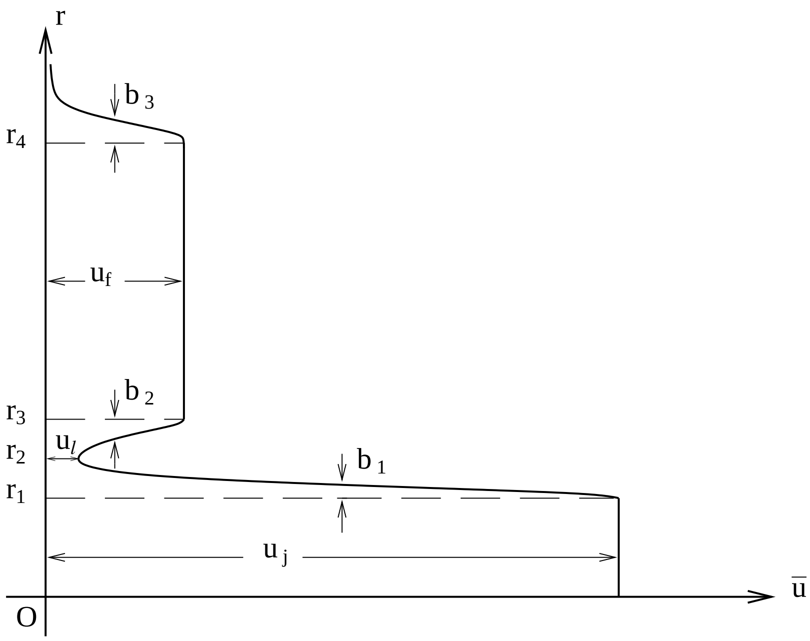

Figure 2.2. Radial profile of jet velocity at the nozzle exit plane.

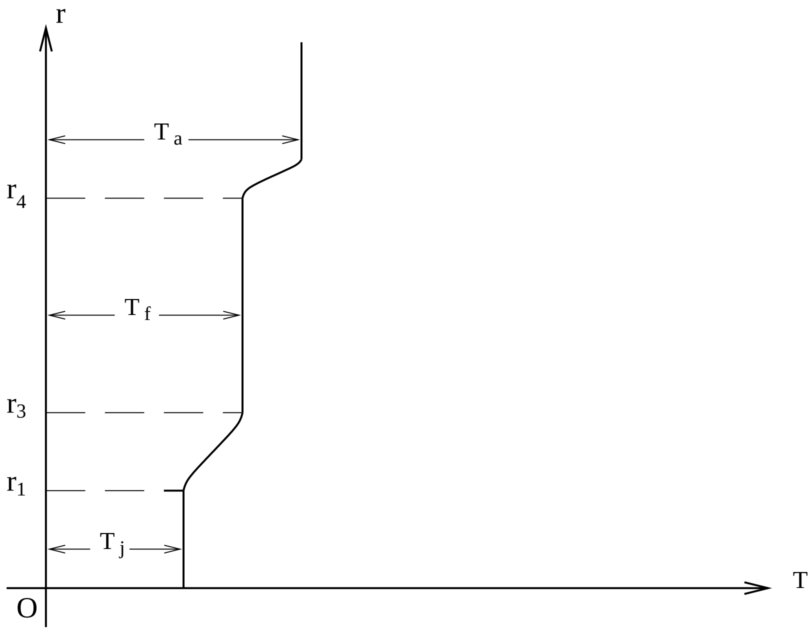

Figure 2.3. Radial profile of jet temperature at the nozzle exit plane.

2.4. Comparison Between Calculated Mean Flow Profiles and Experiment

As stated before, the first step in implementing the Tam and Auriault [23] theory is to calculate the jet mean flow as well as the distributed values of k and ϵ throughout the jet. This is carried out using the algorithm and computer code of Thies and Tam [29]. The initial conditions of equations (2.1) and (2.2) are used at the nozzle exit plane. In this section, the detailed comparisons between the calculated velocity profiles and experimental measurements is presented. For this purpose, the parameters of equations (2.1) and (2.2) are chosen so that the computed profile matches that of the experiment at the first measurement station closest to the nozzle exit.

Figure 2.4 compares the computed and measured centerline velocity distribution of a Mach 0.47 cold jet at 10% and 20% forward velocity ratio (u_f/u_j). The data are from ref. [43]. Figures 2.5a and 2.5b show the corresponding radial profiles of jet velocity at four locations downstream.

Figure 2.6 shows the measured and the computed centerline velocity distribution of two high-speed jets. One is a coaxial jet from ref. [44]. The inner jet is hot, operating at 657 K. The jet exit velocity is 411 m/s. The outer jet is cold at 292 K and has a velocity of 274 m/s. The outer jet is a cold Mach 0.9 jet at 10% forward flight speed from ref. [43]. Figure 2.7a shows the radial profile of the coaxial jet velocity. Close to the nozzle exit, the difference in velocity between the outer jet and inner jet is very distinct. This is captured by the computed result. As the coaxial jet evolves downstream, the inner and outer jet merge to form a smooth profile. Figure 2.7b compares the measured and calculated radial profiles of the axial velocity of the Mach 0.9 jet at 10% forward flight speed.

Figure 2.8 provides comparisons between measurements and predictions for two supersonic jets at Mach 1.37 and 1.67 at 10% forward flight velocity. The experimental data are taken from refs. [43] and [45]. Figure 2.9a shows the radial distribution of the axial velocity of the Mach 1.37 jet. Figure 2.9b shows the corresponding velocity profiles for the Mach 1.67 jet.

Finally, Figure 2.10 shows the measured velocity distribution of a hot coaxial jet with an inverted velocity profile from ref. [46]. Shown also are the computed velocity profiles. The inverted velocity profile, very prominent near the nozzle exit, diminishes in the downstream direction. At sufficiently far downstream, the merged jet exhibits a profile indistinguishable from that of a regular jet. In all of the preceding comparisons, there is excellent agreement in each case (the maximal error never exceeds 5%).

2.5. Comparison Between Calculated Far-Field Noise Spectra and Measurements

Once the mean flow velocity as well as the k and ϵ turbulence quantities are computed, the next step is to calculate the adjoint Green's function according to ref. [25]. To find the far-field noise spectrum, all of those quantities are substituted into equations (1.1) and (1.2). On performing the volume integration over the noise source region, the radiated noise spectrum in the far field is obtained.

2.5.1 Experimental Data

The experimental data used to compare with the calculated noise spectra are from refs. [68] and [43]. The noise measurements in ref. [43] are reported in one-third octave band. The data are converted to narrowband before being compared with calculated spectra.

Some of the mixing noise data from Norum and Brown [68] were slightly contaminated by high-frequency broadband shock associated noise. The Tam and Auriault model is based on the $k - \epsilon$ predictions of fully expanded jet flows.

Thus the results computed in the present work do not take into account the presence of shock cells inside the jets. However, Tam and Golebiowsky [20] showed that the presence of a shock-cell structure in a supersonic jet does not influence the intensity and spectral characteristics of turbulent mixing noise. The mixing noise spectra from imperfectly expanded supersonic jets can therefore be calculated using the mean flow of the corresponding fully expanded jet. The only exception is when intense screech tones are present. For such a jet, the flow as well as the turbulence level are drastically changed. Generally, this may lead to the phenomenon of "broadband noise amplification" under which the noise intensity is greatly enhanced.

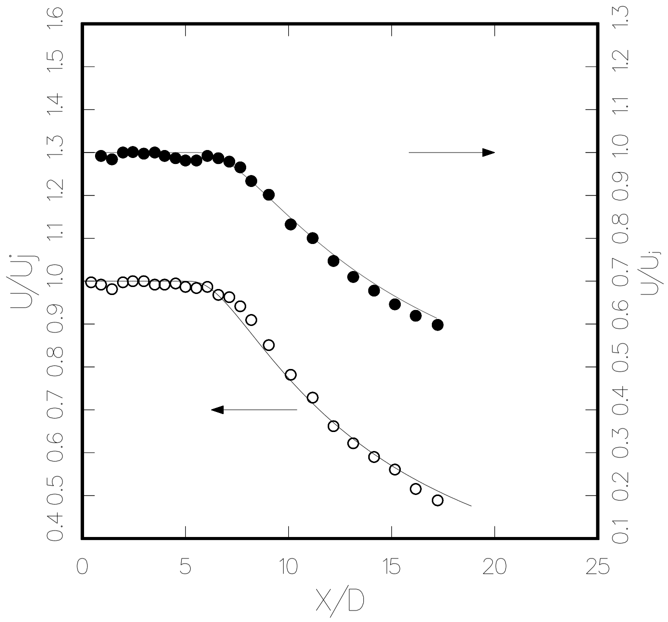

Figure 2.4. Comparison between computed and measured centerline velocity distributions of a Mach 0.47 cold jet. Experiment, Ref. [43], $\circ$ $U_f/U_j = 0.1$, $\bullet$ $U_f/U_j = 0.2$; ———— numerical result.

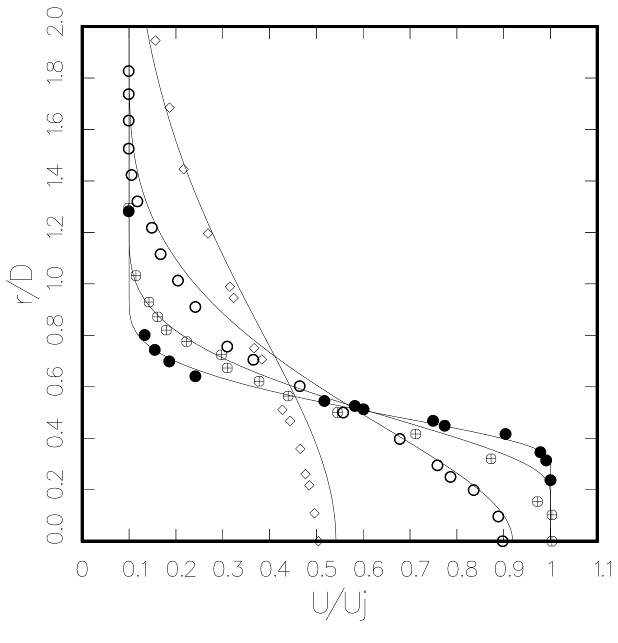

Figure 2.5a. Comparison between computed and measured axial velocity profiles of a Mach 0.47 cold jet at $U_f/U_j = 0.1$. Experiment, Ref. [43], $\bullet$ $x/D = 1.63$, $\oplus$ $x/D = 3.25$, $\circ$ $x/D = 7.50$, $\diamond$ $x/D = 16.0$; ———— numerical result.

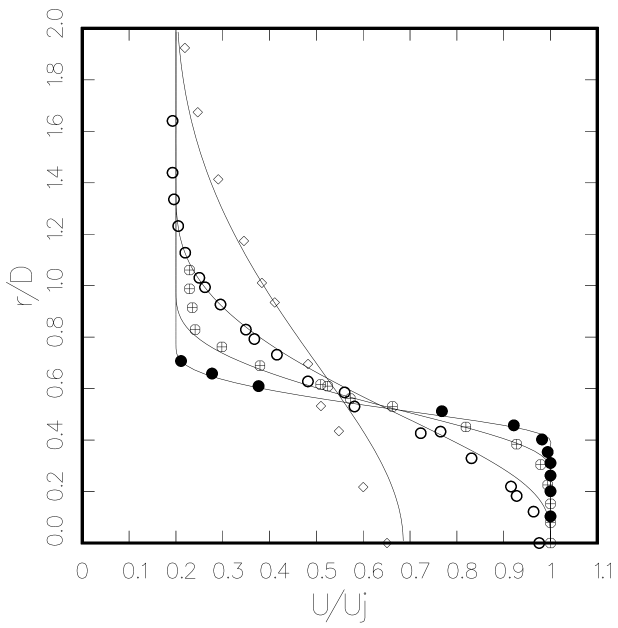

Figure 2.5b. Comparison between computed and measured axial velocity profiles of a Mach 0.47 cold jet at $U_f/U_j = 0.2$. Experiment, Ref. [43], $\bullet$ $x/D = 1.63$, $\oplus$ $x/D = 3.5$, $\circ$ $x/D = 7.0$, $\diamond$ $x/D = 16.0$; ———— numerical result.

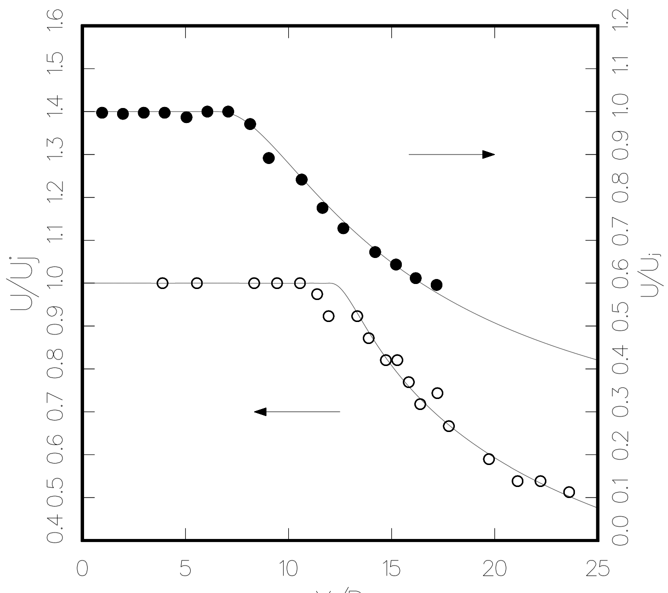

Figure 2.6. Comparison between computed and measured centerline velocity distributions of a coaxial jet of Ref [44] and a Mach 0.9 cold jet of Ref. [43] and [45] at $U_f/U_j = 0.1$. Experimental data, Ref. [44], $\circ$, Ref. [43], [45], $\bullet$; ———— numerical result.

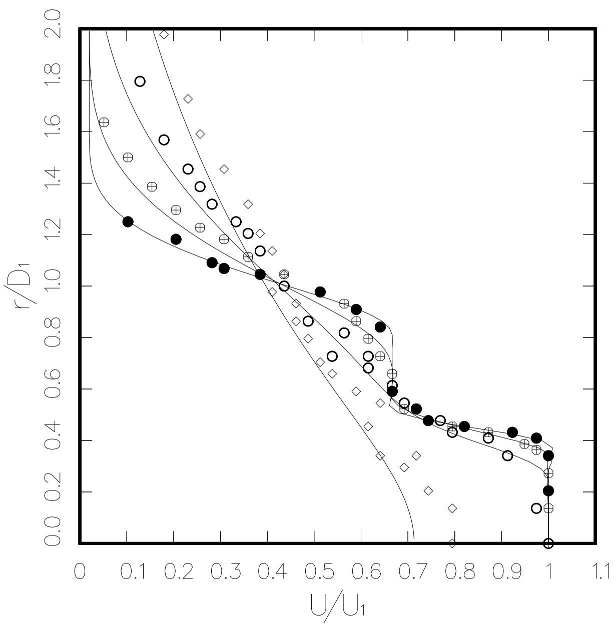

Figure 2.7a. Comparison between computed and measured axial velocity profiles of a coaxial jet with $U_1 = 411$ m/s, $T_1 = 657$ K, $D_1 = 3.92$ cm, $U_2 = 274$ m/s, $T2 = 292$ K, $D_2 = 7.82$ cm . Experiment, Ref. [44], $\bullet\ x/D_1 = 2.0$, $\oplus\ x/D_1 = 4.0$, $\circ\ x/D_1 = 8.0$, $\diamond\ x/D_1 = 16.0$; ———— numerical result.

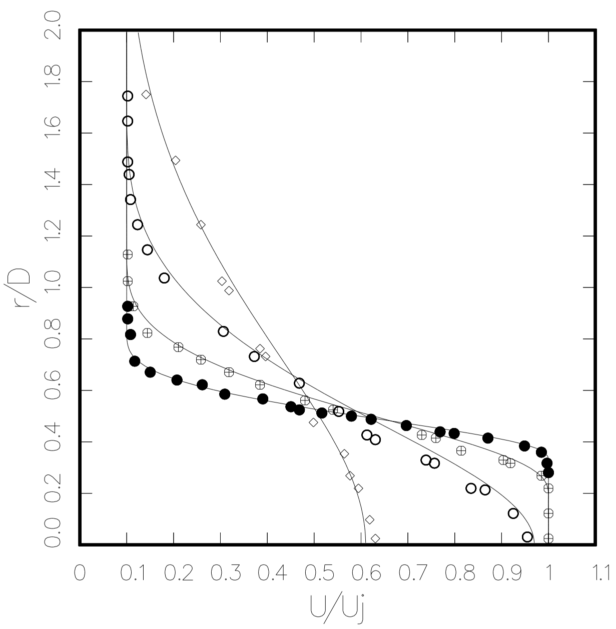

Figure 2.7b. Comparison between computed and measured axial velocity profiles of a Mach 0.9 cold jet at $U_f/U_j = 0.1$. Experiment, Ref. [43], $\bullet\ x/D = 2.0$, $\oplus\ x/D = 4.0$, $\circ\ x/D = 8.0$, $\diamond\ x/D = 16.0$; ———— numerical result.

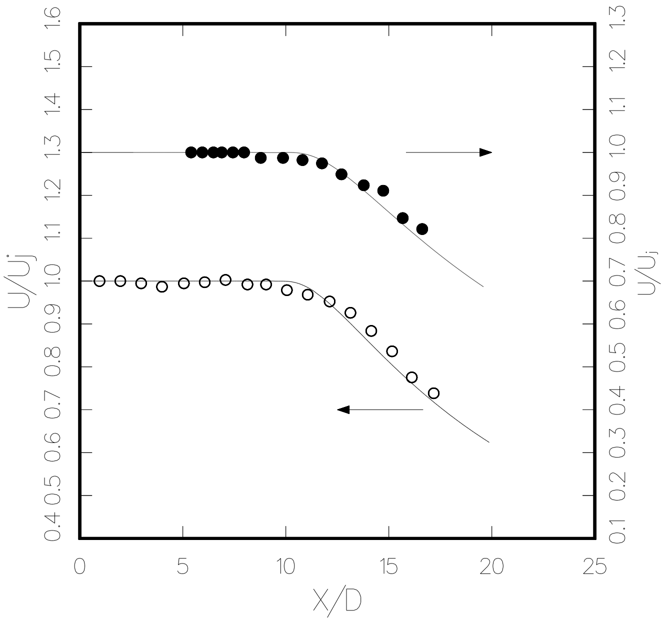

Figure 2.8. Comparison between computed and measured centerline velocity distributions at $U_f/U_j = 0.1$. Experiment, Ref. [43], [45], ∘ Mach 1.37, • Mach 1.67 cold jet; ——— numerical result.

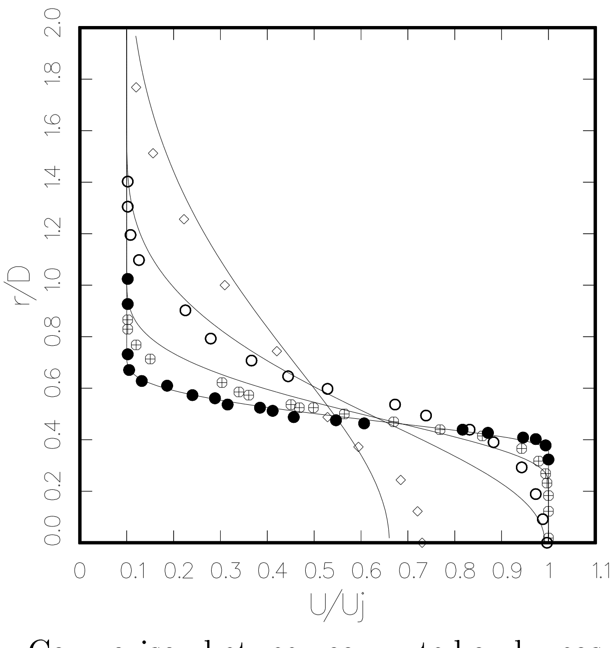

Fig 2.9a. Comparison between computed and measured axial velocity profiles of a Mach 1.37 cold jet at $U_f/U_j = 0.1$. Experiment, Ref. [43], • $x/D = 2.0$, ⊕ $x/D = 4.0$, ∘ $x/D = 8.0$, ⋄ $x/D = 16.0$; ——— numerical result.

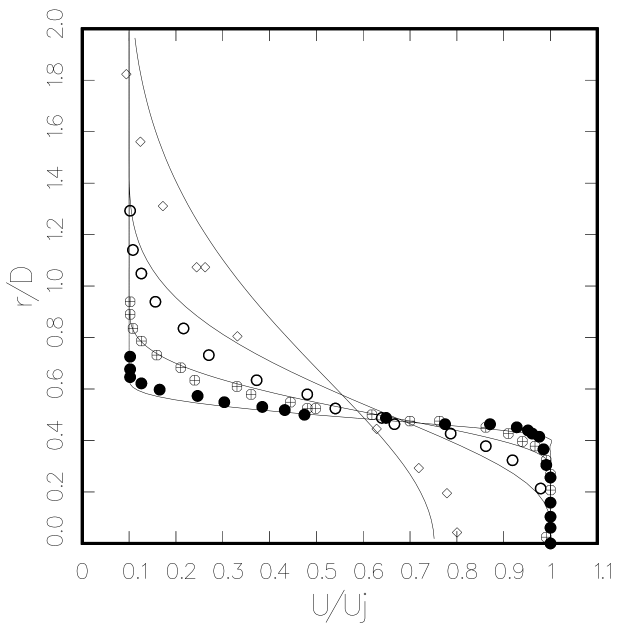

Fig 2.9b. Comparison between computed and measured axial velocity profiles of a Mach 1.67 cold jet at $U_f/U_j = 0.1$. Experiment, Ref. [43], $\bullet$ $x/D = 2.0$, $\oplus$ $x/D = 4.0$, $\circ$ $x/D = 8.0$, $\diamond$ $x/D = 16.0$; ——— numerical result.

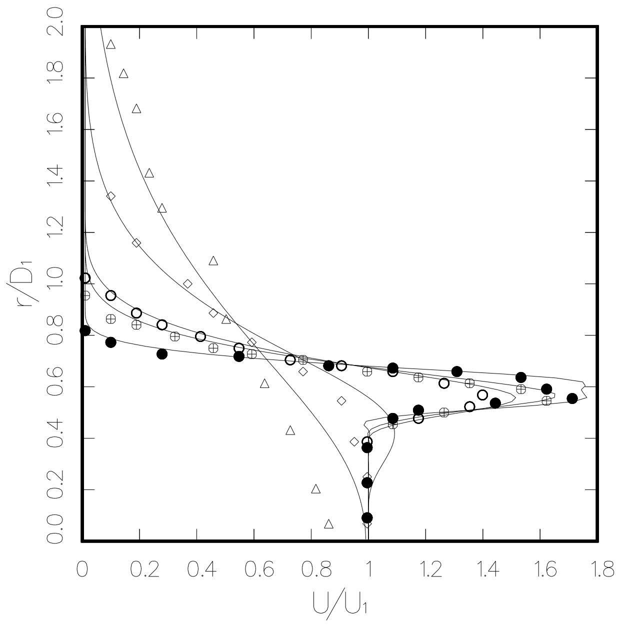

Figure 2.10. Comparison between computed and measured axial velocity profiles of an inverted profile coaxial jet at $U_1 = 273$ m/s, $T_1 = 434$ K, $D_1 = 5.22$ cm, $U_2 = 477$ m/s, $T2 = 758$ K, $D_2 = 7.14$ cm. Experiment, Ref.[46], $\bullet$ $x/D_1 = 0.19$, $\oplus$ $x/D_1 = 1.35$, $\circ$ $x/D_1 = 1.90$, $\diamond$ $x/D_1 = 5.75$, $\triangle$ $x/D_1 = 11.5$; ——— numerical result.

2.5.2 Normalization of Experimental Data

The nozzle sizes and the microphone distances to the nozzle used in the experiments are not the same. In order to facilitate comparisons, the experimental data need to be normalized to a standard condition. Here, all spectral densities are normalized to $R = 100D_j$, and nondimensionalized by $\frac{u_j}{D_j}$ and p_{ref} of the decibel scale. The noise spectra are plotted as a function of the Strouhal number $St = \frac{fD_j}{u_j}$.

In dimensionless form, the far-field mixing noise spectrum depends only on three parameters. They are the jet velocity ratio $\frac{u_j}{a_\infty}$, the jet temperature ratio $\frac{T_j}{T_\infty}$ and the angle of radiation Θ. The reservoir temperature T_r is related to the fully expanded jet temperature by the condition of constant total enthalpy

$$\frac{T_r}{T_j} = 1 + \frac{\gamma - 1}{2} {M_j}^2 \tag{2.3}$$

where M_j is the jet Mach number. For supersonic jets, the fully expanded jet diameter D_j is related to the nozzle exit diameter D by the formula

$$D_j = D \left[\frac{1 + (\gamma - 1)\frac{M_j^2}{2}}{1 + (\gamma - 1)\frac{M_d^2}{2}} \right]^{\frac{\gamma+1}{4(\gamma-1)}} \left(\frac{M_d}{M_j} \right)^{\frac{1}{2}} \tag{2.4}$$

where M_d is the nozzle design Mach number. For subsonic jets, D_j is equal to D.

2.5.3 Jet Noise Spectrum Comparisons

Figure 2.11 shows the calculated and measured noise spectra of a Mach 1.5 jet from a convergent-divergent nozzle operating at design condition at three simulated forward flight Mach numbers. The data are from the work of Norum and

Brown [68]. Figure 2.11a shows the spectra at $\Theta = 60$ deg measured from the jet exhaust direction. The top curve is for zero flight Mach number. The second curve is for flight Mach number 0.2. The bottom curve is for flight Mach number 0.4. It is easily seen that the calculated spectra are in good agreement (within 1%) with measurements. For each 0.2 increase in flight Mach number, there is approximately a 4.5-dB decrease in the measured peak noise level. This drop in the measured noise level is matched well by the computed results. At simulated forward flight Mach number 0.4, the jet noise is greatly reduced. This exposes the low-frequency mixing noise from the open wind tunnel. In fig 2.11a, the wind-tunnel noise is responsible for the low frequency hump of the noise spectrum. This hump is predicted quite accurately by the theory.

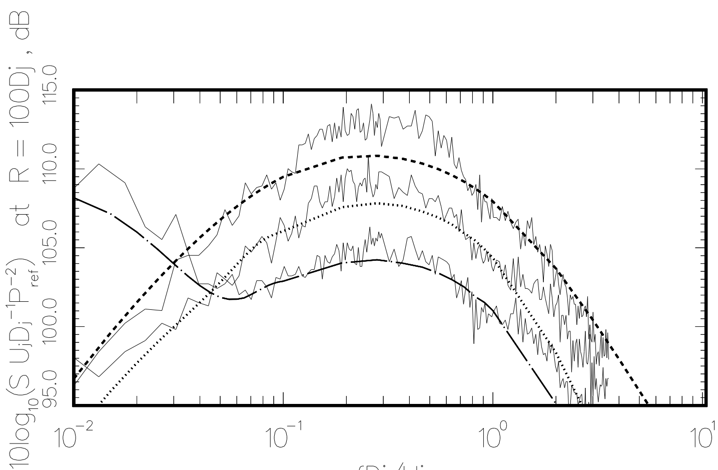

Figure 2.11a. Comparisons between measured and computed far field noise spectra of a Mach 1.5 cold jet at $\Theta = 60$ deg: ——— experimental data, Ref. [68]; computed results, - - - - - - - $M_f = 0.0$, ... $M_f = 0.2$, — · — · — · — $M_f = 0.4$.

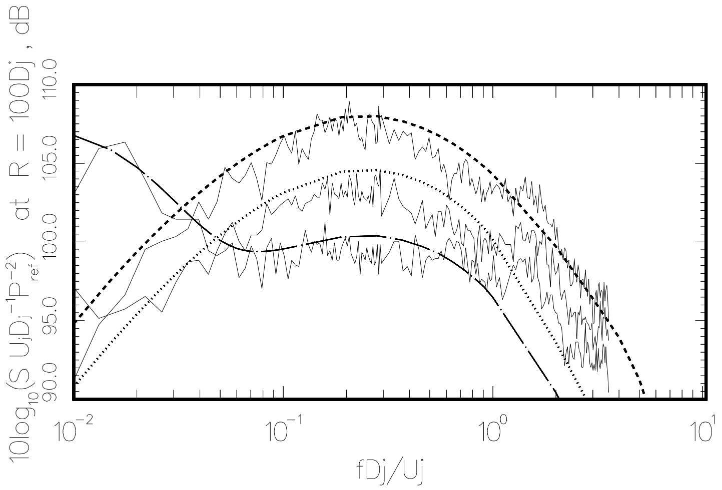

Figure 2.11b. Comparisons between measured and computed far field noise spectra of a Mach 1.5 cold jet at $\Theta = 90$ deg: ———— – experimental data, Ref. [68]; computed results, - - - - - - - $M_f = 0.0$, ... $M_f = 0.2$, — · — · — · — $M_f = 0.4$.

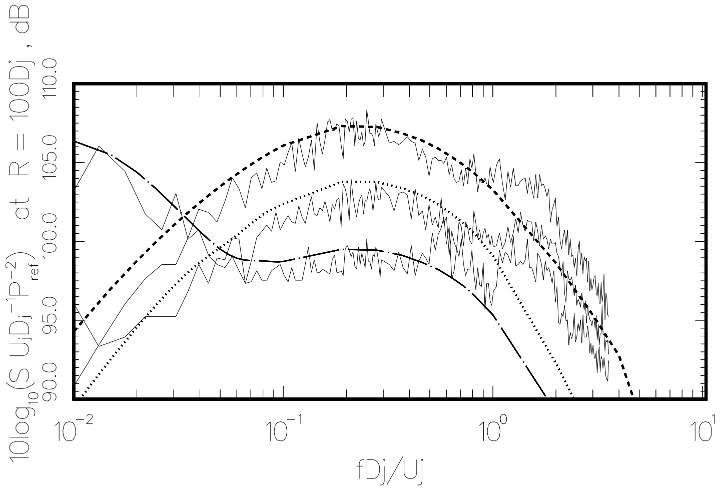

Figure 2.11c. Comparisons between measured and computed far field noise spectra of a Mach 1.5 cold jet at $\Theta = 100$ deg: ———— — experimental data, Ref. [68]; computed results, - - - - - - - $M_f = 0.0$, ... $M_f = 0.2$, — · — · — · — $M_f = 0.4$.

Figures 2.11b and 2.11c show similar comparisons at $\Theta = 90$ deg and $\Theta = 100$ deg, respectively. Again, there is good overall agreement between the measured and calculated spectra. The high-frequency broadband shock associated noise explains why the agreement at high frequencies is not as good (5% error).

Figure 2.12 shows the measured and calculated jet noise spectra for subsonic jets at various jet and flight Mach numbers, M_j, and M_f. The data are from ref. [21]. Figure 2.12a is for spectra measured at $\Theta = 90$ deg. The jets are at Mach numbers 0.98, 0.73, and 0.51. For the particular facility used in the experiment, the open wind tunnel has to be turned on all the time to avoid certain kinds of resonance. The static case is represented by the case with a very small forward flight Mach number. It is clear from the Figure 2.12a that the predictions match the measurements quite well (within 1% at low frequencies and near the peak regions) for all Mach numbers. At subsonic jet Mach number, it appears that there is a 5 dB decrease in the noise spectrum for a 0.2 increase in forward flight Mach number. This reduction is reproduced well by the theory (the error less than 1%.

Figure 2.12b shows the corresponding change in the noise spectrum at $\Theta = 60$ deg. Because of noise source convection and mean flow refraction effects, the spectra at $\Theta = 60$ deg are consistently 2-3 dB higher than those at $\Theta = 90$ deg. On considering that the theoretical predictions are tantamount to absolute predictions, it is deemed that there are good agreements between measurements and theory near the peak regions of the spectra. It is not clear whether the discrepancies at high frequencies are due to contamination of the measured data (including the error involved in converting one-third octave band data to narrowband) or a deficiency of the theory. However, the $\triangle$ decibel changes between different flight Mach numbers appear to be quite accurately predicted.

2.6. Effects of Forward Flight on Turbulence and Noise Source Positions

The effects of forward flight on the mean flow of a high-speed jet are relatively well known. Obviously the presence of an outside flow reduces the shear gradient across the mixing layer of the jet [43]. This then leads to a reduction in the jet spreading rate. With a smaller spreading rate, the potential core of the jet is lengthened.

The changes in the mean flow due to forward flight, in turn, alter the turbulence and the source of noise in the jet. In this section, the effects of forward flight on the noise source distribution are investigated quantitatively by means of equations (1.1) and (1.2). Equation (1.2) provides the formula by which the far-field noise spectrum of a jet can be calculated. It has the form of a volume integral over the source location $\mathbf{x}_2$. A simple interpretation of this formula suggests that the integrand is the noise source. In the notation of the formula, the source is located at $\mathbf{x}_2$ and is responsible for radiating sound to the far-field observation point at $\mathbf{x}$ at frequency $f(\omega = 2\pi f$ is the angular frequency). Equation (1.2) contains the effects of mean flow refraction. Here our interest is on the source modification effects due to forward flight alone. For this purpose, we will restrict the observation point to $\Theta = 90$. At this angle of radiation, the mean flow refraction effects are minimal.

When the preceding interpretation of equation (1.2) is followed, the formula for the axial distribution of noise sources for a slice of the jet between x_2 and $x_2 + dx_2$ is $S_x(\mathbf{x}, x_2, \omega)dx_2$, where

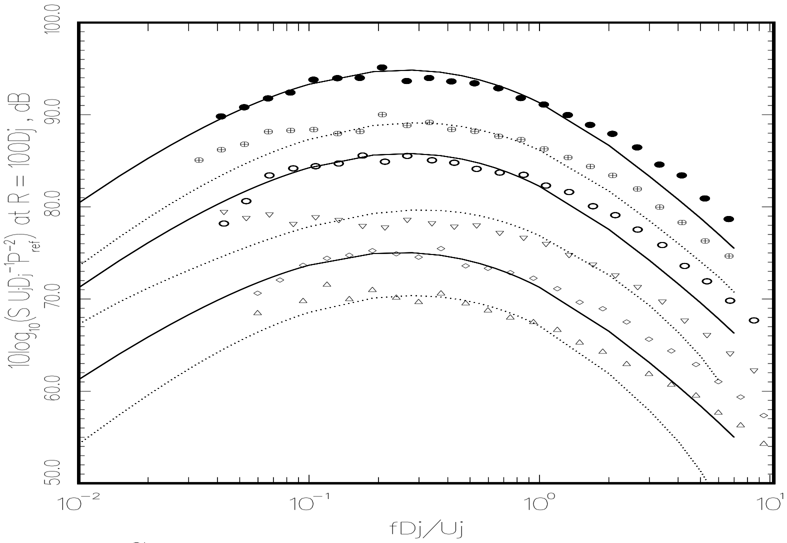

Figure 2.12a. Comparisons between measured and computed data for cold jets at $\Theta = 90$ deg; Experiment, Ref. [43], $\bullet$ $M_j = 0.98$ $M_f = 0.05$ $\oplus$ $M_j = 0.98$ $M_f = 0.20$ $\circ$ $M_j = 0.73$ $M_f = 0.04$ $\bigtriangledown$ $M_j = 0.74$ $M_f = 0.20$ $\diamond$ $M_j = 0.51$ $M_f = 0.02$ $\triangle$ $M_j = 0.51$ $M_f = 0.10$; Computed results, ... and ——— .

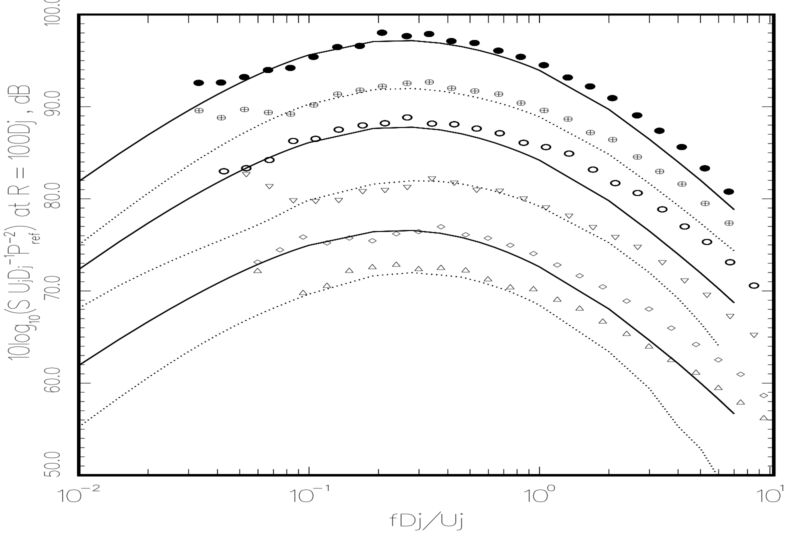

Figure 2.12b. Comparisons between measured and computed data for cold jets at $\Theta = 60$ deg; Experiment, Ref. [43], $\bullet$ $M_j = 0.98$ $M_f = 0.05$ $\oplus$ $M_j = 0.98$ $M_f = 0.20$ $\circ$ $M_j = 0.73$ $M_f = 0.04$ $\bigtriangledown$ $M_j = 0.74$ $M_f = 0.20$ $\diamond$ $M_j = 0.51$ $M_f = 0.02$ $\triangle$ $M_j = 0.51$ $M_f = 0.10$; Computed results, ... and ——— .

$$S_x(\mathbf{x}, x_2, \omega) = 4\pi\left(\frac{\pi}{ln2}\right)^{\frac{3}{2}} \int_0^{2\pi}\int_0^{\infty} \frac{\hat{q}_s^2 l^3{}_s}{c^2\tau_s} \frac{|p_a(\mathbf{x}_2, \mathbf{x}, \omega)|^2 e^{-\frac{\omega^2 l^2{}_s}{\overline{u}^2(4ln2)}}}{[1+\omega^2\tau_s{}^2(1-\frac{\overline{u}}{a_\infty}cos\Theta)^2]} r_2 dr_2 d\phi_2 \tag{2.5}$$

$$SPL_x(\mathbf{x}, x_2, \frac{fD_j}{u_j}) = 10\text{log}\left[\frac{4\pi S_x(\mathbf{x}, x_2, \omega)}{(p_{ref}^2/u_j)}\right] \tag{2.6}$$

where $\mathbf{x} = (R, \pi/2, \phi)$ is the observation point and $\mathbf{x}_2 = (r_2, \phi_2, x_2)$ is the source point. Sound pressure level (SPL_x) has the dimension of decibel per Stouhal number per unit axial length of the jet.

Another formula that is of interest to us is the azimuthally integrated noise source distribution, S_ϕ. This is the noise source distribution in the $x_2 - r_2$ plane with ϕ_2 integrated from 0 to 2π. When starting from equation (1.2), the following expression for S_ϕ can easily be found:

$$S_\phi(\mathbf{x}, x_2, r_2, \omega) = 4\pi\left(\frac{\pi}{ln2}\right)^{\frac{3}{2}} \int_0^{2\pi} \frac{\hat{q}_s^2 l^3{}_s}{c^2\tau_s} \frac{|p_a(\mathbf{x}_2, \mathbf{x}, \omega)|^2 e^{-\frac{\omega^2 l^2{}_s}{\overline{u}^2(4ln2)}}}{[1+\omega^2\tau_s{}^2(1-\frac{\overline{u}}{a_\infty}cos\Theta)^2]} d\phi_2 \tag{2.7}$$

$$SPL_\phi = 10\text{log}\left[\frac{4\pi S_\phi D_j^2}{(p_{ref}^2/u_j)}\right] \tag{2.8}$$

S_ϕ provides a measure of the radial distribution of the noise sources in a jet where the radial distance is measured in units of D_j.

2.6.1. Effects on Turbulence

Because the change in noise sources due to forward flight is a direct consequence of the change in jet turbulence, we will first examine the changes in turbulence intensity, the size of eddies responsible for noise radiation, and the eddy decay time. Figure 2.13a shows a contour map of the turbulence intensity (nondimensionalized by the square of the jet velocity), $k/u^2{}_j$, in the $x_2 - r_2$ plane for a Mach 1.5 cold jet in static condition. For convenience, the subscript 2 will be dropped and the plane labeled as $x - r$ plane so no confusion should arise. It is clear that the intensity is highest in the initial jet mixing layer. The intensity decreases in the downstream direction. Figure 2.13b shows contour map for the same jet at 0.3 forward flight Mach number. When compared with Figure 2.13a it is evident that forward flight at $M_f = 0.3$ reduces the turbulence intensity greatly. Also because the jet spreading is decreased, the jet turbulence is confined to a thinner mixing layer.

Figure 2.14a shows the contours of l_s/D_j in the $x - r$ pane for the Mach 1.5 cold jet in static condition, where l_s is the typical size of noise producing eddies. Along the lip line where k is most intense, it is easy to see from Figure 2.14a that l_s increases almost linearly with downstream distance. The increase in eddy size in the downstream direction is expected on physical grounds. The linear increase is an indication of the self-similarity property of jet flows. Figure 2.14b shows the contours for the same jet at Mach 0.3 forward flight. A simple comparison of Figures 2.14a and 2.14b indicates that the eddy size at the same location downstream is smaller with forward flight. The rate of increase in the eddy size is also reduced. If one associates higher frequency sound to smaller eddies, then one expects an increase in high-frequency sound and simultaneously a decrease in low-frequency noise resulting in a slight shift of the noise spectrum to higher frequency. This is consistent with experimental measurements (Figures 2.11, 2.12).

Figure 2.15a is a contour map of $\tau_s U_j/D_j$, the eddy decay time for the Mach

1.5 jet in a static condition. The eddy decay time increases in the downstream direction. Physically, it means that smaller eddies in the initial mixing layer of the jet decay much faster than the large eddies in the developed region of the jet. Figure 2.15b shows the contours at 0.3 forward flight Mach number. When the contours along the lip line of the jet are compared, it is clear that, up to 20 jet diameters downstream, the decay time is nearly unchanged by forward flight. This is somewhat unexpected.

Although Figures 2.13-2.15 show only the effects of forward flight on the turbulence characteristics of a Mach 1.5 jet, the trends are the same for jets at other Mach numbers, including subsonic jets. Qualitatively, one may use the relative changes indicated in Figures 2.13-2.15 to estimate the corresponding changes for jets at other operating conditions.

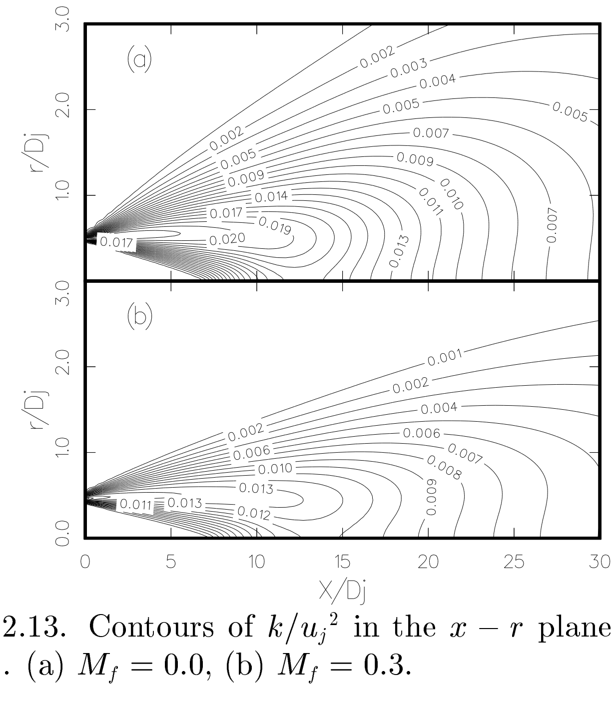

Figure 2.13. Contours of $k/{u_j}^2$ in the $x-r$ plane for a Mach 1.5 cold jet. (a) $M_f = 0.0$, (b) $M_f = 0.3$.

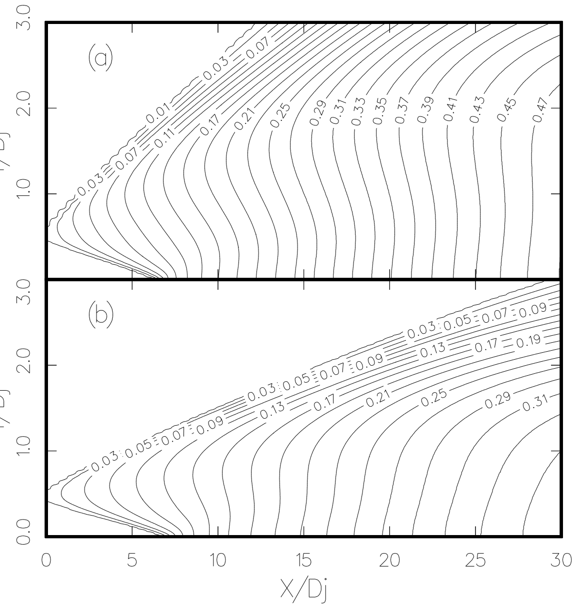

Figure 2.14. Contours of l_s/D_j in the $x - r$ plane for a Mach 1.5 cold jet. (a) $M_f = 0.0$, (b) $M_f = 0.3$.

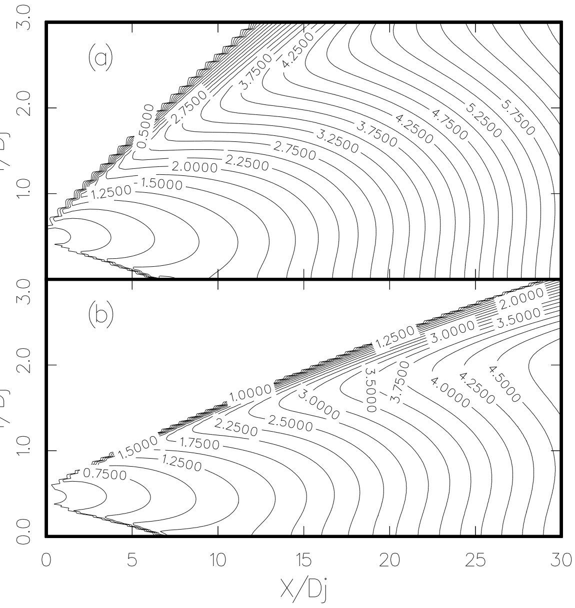

Figure 2.15. Contours of $\tau_s u_j/D_j$ in the $x - r$ plane for a Mach 1.5 cold jet. (a) $M_f = 0.0$, (b) $M_f = 0.3$.

2.6.2. Effects on Jet Noise Source Distribution

In order to separate the effects of forward flight on the sources of jet noise from mean flow refraction effect, the observer's coordinates are fixed to be at $R = 100D_j$ and $\Theta = 90$ deg as before. The mean flow refraction effect is minimal at 90-deg radiation [23].

Figure 2.16a shows the calculated axial noise source distribution [see equations (2.5) and (2.6)] of a Mach 1.5 cold jet in static condition for a number of Strouhal numbers. Figure 2.16a indicates that the high-frequency noise sources are located very close to the nozzle exit. The low-frequency noise sources are located much farther downstream and extend well beyond the potential core of the jet. The noise source intensity peaks around Strouhal number 0.3. Spatially, the peak intensity is located near the end of the potential core. Figure 2.16b shows the distribution at 0.3 forward flight Mach number. It is evident from Figures 2.16a and 2.16b that forward flight moves all of the noise sources downstream. The noise source intensity is significantly reduced for all frequencies.

Figure 2.17 is a comparison of the measured and calculated peak source strength location as a function of Strouhal number for high subsonic jets. The experimental data are from references [47] and [48]. Experimentally, noise source location measurements are difficult to perform and are usually subjected to a high degree of uncertainty. Figure 2.17 shows good agreement between theory and experiment over a large range of Strouhal number (0.1-10). The good agreement lends confidence in the original jet noise theory of Tam and Auriault [23] from which equations (2.5) and (2.6) are derived.

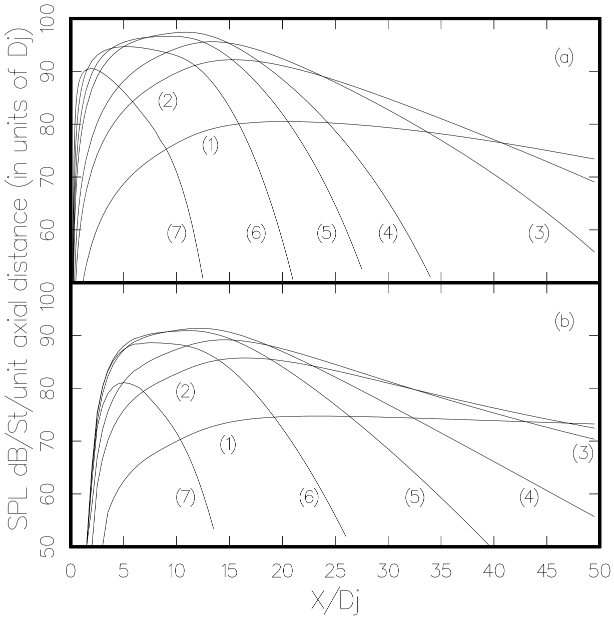

Figure 2.16. Axial noise source distribution for an observer at $\Theta = 90^{\circ}$ and $R = 100D_j$. Mach 1.5 cold jet. (1) St = 0.01, (2) St = 0.05, (3) St = 0.1, (4) St = 0.3, (5) St = 0.5, (6) St = 1.0, (7) St = 3.0. (a) $M_f = 0.0$, (b) $M_f = 0.3$.

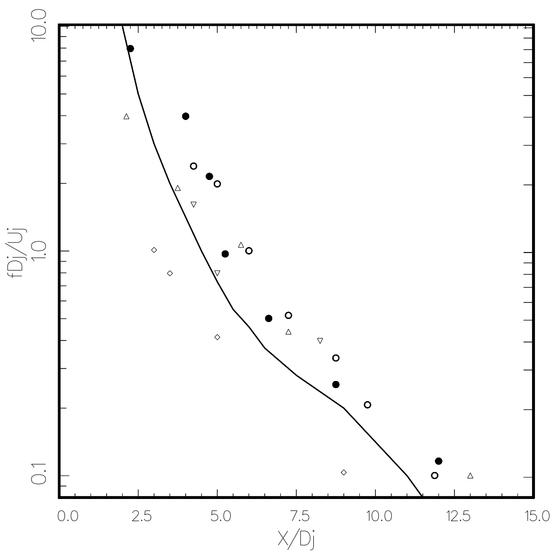

Figure 2.17. Calculated and measured peak source strength locations. Experiment: $\bullet$ Acoustic mirror, $D = 20$ mm, $M_j = 1.0$, $\bigtriangledown$ Acoustic mirror, $D = 25$ mm, $M_j = 1.0$, $\circ$ Polar correlation, $D = 25$ mm, $M_j = 0.86$, $\triangle$ Polar correlation, $D = 51$ mm, $M_j = 0.86$, Ref. [47] ; $\diamond$ Polar correlation, full scale engine, 80% rpm, Ref. [48].

Figures 2.18-2.20 provide a measure of the changes in noise source distribution in the $x - r$ plane due to forward flight. Figure 2.18 is for Strouhal number 0.01. It is representative of the low-frequency part of the spectrum. Figure 2.19 is for Strouhal number 0.3 (frequency at maximum noise level). Figure 2.20 is for Strouhal number 1.0, representative of the high-frequency part of the spectrum. Figures 2.18-2.20 again indicate that the high-frequency noise sources are located close to the nozzle exit, whereas the low-frequency noise sources are located much farther downstream. The effect of forward flight is to move all of the noise sources downstream. In the radial direction the noise sources are most intense around the nozzle lip line, where the shear gradient of the mean velocity is largest. This is true even in forward flight. The sources are confined radially to the jet mixing layer both in the static condition and in flight.

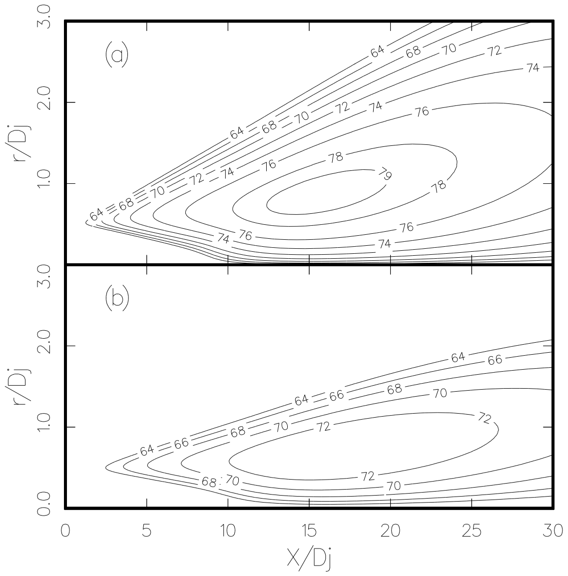

Figure 2.18. Contours of azimuthally integrated noise source intensity in the $x - r$ plane for an observer at $\Theta = 90°$ and $R = 100D_j$. Mach 1.5 cold jet. St = 0.0 1 Contours in units of SPL dB/St/unit area of $x - r$ plane (length scale = D_j). (a) $M_f = 0.0$, (b) $M_f = 0.3$.

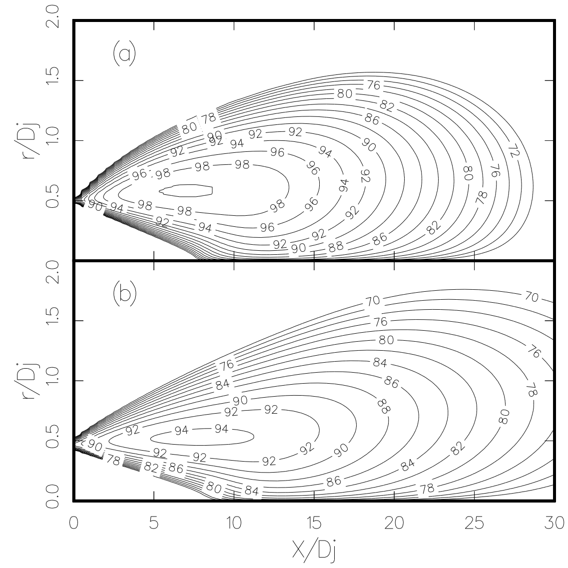

Figure 2.19. Contours of azimuthally integrated noise source intensity in the $x-r$ plane for an observer at $\Theta = 90^\circ$ and $R = 100D_j$. Mach 1.5 cold jet. St = 0.3 Contours in units of SPL dB/St/unit area of $x-r$ plane (length scale = D_j). (a) M_f = 0.0, (b) $M_f = 0.3$.

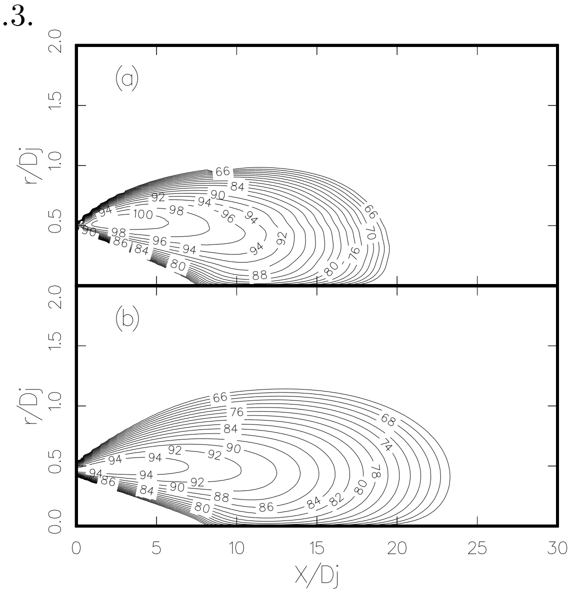

Figure 2.20. Contours of azimuthally integrated noise source intensity in the $x-r$ plane for an observer at $\Theta = 90^\circ$ and $R = 100D_j$. Mach 1.5 cold jet. St = 1.0 Contours in units of SPL dB/St/unit area of $x-r$ plane (length scale = D_j). (a) M_f = 0.0, (b) $M_f = 0.3$.

One important point is that jet noise source distribution is not completely dependent on the turbulence intensity (k) distribution of the jet flow alone. This is clear by comparing Figures 2.13 and 2.18. The obvious difference in the patterns of Figures 2.13 and 2.18 indicates that the noise source is influenced not only by k but also by the eddy size and decay time of the eddies. The relationship is quite complex. It would be wrong to regard the noise of a jet as simply a function of k. Other aspects of jet turbulence are also important in the sound generation process.

CHAPTER III

NOISE FROM THE FINE SCALE TURBULENCE OF NONAXISYMMETRIC JETS

A search through literature reveals that there is no reliable nonaxisymmetric jet noise prediction theory at the present time. In this chapter the jet noise theory of Tam and Auriault [23] is extended to nonaxisymmetric jets. In the original work, only axisymmetric jets were considered.

To calculate the noise from nonaxisymmetric jets, two crucial requirements must be met. First, one must compute the mean flow and the turbulence quantities needed for the noise source model. Second, a method to calculate the flow refraction effects over the entire frequency spectrum of jet noise has to be developed.

The Tam and Auriault theory relies on the $k-\epsilon$ turbulence model for input on jet mean flow, noise source intensity and the characteristic length and time scales of the turbulence. To calculate the mean flow Thies and Tam [24] solved the parabolized Reynolds Averaged Navier-Stokes (RANS) equations supplemented by the $k-\epsilon$ model. They employed the highly accurate Dispersion-Relation-Preserving (DRP) scheme [42] for numerical solution. In this work, the mean flows of nonaxisymmetric jets are calculated essentially by the same procedure except that an improved set of boundary conditions are imposed. The new boundary conditions are developed to allow the computation to be carried out in a smaller computational domain.

The nonaxisymmetric mean flow of a jet, undoubtedly, has a significant impact on the noise directivity through refraction alone. Since low frequency sound having long acoustic wave length is less affected by refraction while high frequency sound does, the nonaxisymmetric mean flow will modify the noise spectrum in the far field. In the past, there have been many investigations on how best to quantify mean flow effects. Most of the approaches used asymptotic analysis based either on the low frequency limit; e.g. Goldstein [50], [51], or the high frequency limit; e.g., Balsa [52], Goldstein [53]. Durbin [54], [55], Khavaran and Krejsa [56], [57] considered the zero wavelength limit of geometric acoustics and ray tracing. But jet noise is broadband, extending over a frequency range of almost three decades. It is difficult to justify the use of asymptotic results over such a broad frequency range. Typically, the Strouhal number, fD/u_j, at the peak of the noise spectrum is approximately equal to 0.3. For commercial jet engines, u_j is roughly equal to the speed of sound. Thus the acoustic wavelength is as long as 3 jet diameters. This is definitely not in the high frequency limit. Moreover, Khavaran [58] stated that the use of ray tracing was too computationally intensive to be practical.

In this work, the flow effect is included in the theory through an extension of the adjoint Green's function approach of Tam and Auriault [25]. The adjoint Green's function problem is recast into a two-dimensional sound scattering problem. The sound scattering problem is then solved computationally in the time domain by the DRP scheme [24]. A perfectly matched layer (PML) boundary condition [12] is enforced around the finite computation domain. The PML absorbs the scattered sound waves and thus prevents their reflection back into the computation domain (see Appendix A). In this way, possible contamination of the numerical solution is avoided.

3.1. Mean Flow and Turbulence Computation

In this section, the formulation of the new boundary conditions is presented. In this investigation, the mean flow and turbulence kinetic energy of nonaxisymmetric jets are calculated by the procedure used by Thies and Tam [24]. Thies and Tam solved the parabolized RANS equations by means of DRP scheme [42]. The solution starts at the nozzle exit plane and marches downstream. It is well known that the parabolized RANS equations are numerically unstable in regions without a mean flow in the downstream direction [24]. To stabilize the numerical solution, a small forward flight velocity, 2% or less of the jet exit velocity, is added outside the static jet. The computation is carried out in a finite domain in the $y-z$ plane at each x-station. x is taken to be the flow direction. Because a finite domain is used, a set of boundary conditions must be imposed at the external boundaries. In the present investigation, a new set of boundary conditions are used. This set of boundary conditions is derived without invoking the far-field assumption $r \to \infty$. This allows the computation to be done in a smaller computational domain. The numerical results are found to be in good agreement with those obtained by the original code of Thies and Tam. But the computation time is reduced.

The parabolized RANS equations with respect to a Cartesian coordinate centered at the nozzle exit with the x-axis pointing in the flow direction are,

$$u\frac{\partial u}{\partial x} = -v\frac{\partial u}{\partial y} - w\frac{\partial u}{\partial z} - \frac{1}{\rho}\Big[\frac{\partial(\rho\tau_{xy})}{\partial y} + \frac{\partial(\rho\tau_{xz})}{\partial z}\Big]$$

$$u\frac{\partial v}{\partial x} = -v\frac{\partial v}{\partial y} - w\frac{\partial v}{\partial z} - \frac{1}{\rho}\Big[\frac{\partial(\rho\tau_{yy})}{\partial y} + \frac{\partial(\rho\tau_{yz})}{\partial z} + \frac{\partial p}{\partial y}\Big]$$

$$u\frac{\partial w}{\partial x} = -v\frac{\partial w}{\partial y} - w\frac{\partial w}{\partial z} - \frac{1}{\rho}\Big[\frac{\partial(\rho\tau_{yz})}{\partial y} + \frac{\partial(\rho\tau_{zz})}{\partial z} + \frac{\partial p}{\partial z}\Big]$$

$$\begin{aligned}
u\frac{\partial T}{\partial x} &= -v\frac{\partial T}{\partial y} - w\frac{\partial T}{\partial z} - (\gamma-1)T\Big(\frac{\partial u}{\partial x} + \frac{\partial v}{\partial y} + \frac{\partial w}{\partial z}\Big) + \gamma(\gamma-1){M_j}^2\epsilon \\
&\quad + \frac{1}{\rho\sigma_T}\Big[\frac{\partial}{\partial y}(\rho\nu_t\frac{\partial T}{\partial y}) + \frac{\partial}{\partial z}(\rho\nu_t\frac{\partial T}{\partial z})\Big] \\
u\frac{\partial k}{\partial x} &= -v\frac{\partial k}{\partial y} - w\frac{\partial k}{\partial z} - \epsilon - \tau_{xy}\frac{\partial u}{\partial y} - \tau_{xz}\frac{\partial u}{\partial z} - \tau_{yy}\frac{\partial v}{\partial y} - \tau_{yz}\frac{\partial v}{\partial z} - \tau_{zy}\frac{\partial w}{\partial y} \\
&\quad -\tau_{zz}\frac{\partial w}{\partial z} + \frac{1}{\rho\sigma_k}\Big[\frac{\partial}{\partial y}(\rho\nu_t\frac{\partial k}{\partial y}) + \frac{\partial}{\partial z}(\rho\nu_t\frac{\partial k}{\partial z})\Big] \qquad (3.1) \\
u\frac{\partial \epsilon_s}{\partial x} &= -\frac{C_{\epsilon_1}\epsilon_s}{k}\Big[{\tau^s}_{xy}\frac{\partial u}{\partial y} + {\tau^s}_{xz}\frac{\partial u}{\partial z} + {\tau^s}_{yy}\frac{\partial v}{\partial y} + {\tau^s}_{yz}\frac{\partial v}{\partial z} + {\tau^s}_{zy}\frac{\partial w}{\partial y} + {\tau^s}_{zz}\frac{\partial w}{\partial z}\Big] \\
&\quad -v\frac{\partial \epsilon_s}{\partial y} - w\frac{\partial \epsilon_s}{\partial z} - (C_{\epsilon_2} - C_{\epsilon_3}\chi)\frac{{\epsilon_s}^2}{k} + \frac{1}{\rho\sigma_\epsilon}\Big[\frac{\partial}{\partial y}(\rho{\nu^s}_t\frac{\partial \epsilon_s}{\partial y}) + \frac{\partial}{\partial z}(\rho{\nu^s}_t\frac{\partial \epsilon_s}{\partial z})\Big] \\
u\frac{\partial p}{\partial x} &= -v\frac{\partial p}{\partial y} - w\frac{\partial p}{\partial z} - p\Big(\frac{\partial u}{\partial x} + \frac{\partial v}{\partial y} + \frac{\partial w}{\partial z}\Big) + \frac{p}{T}\Big(u\frac{\partial T}{\partial x} + v\frac{\partial T}{\partial y} + w\frac{\partial T}{\partial z}\Big)
\end{aligned}$$

$$\rho = \frac{\gamma M_j^2 p}{T}, \qquad \epsilon = \epsilon_s(1+\alpha M_t^2), \quad M_t^2 = \frac{2k}{T}M_j^2$$

$$\nu_t = C_\mu\frac{k^2}{\epsilon+\epsilon_0}, \qquad {\nu^s}_t = C_\mu\frac{k^2}{\epsilon_s+\epsilon_0}$$

$$\tau_{ij} = -\nu_t\Big(\frac{\partial u_i}{\partial x_j} + \frac{\partial u_j}{\partial x_i} - \frac{2}{3}\frac{\partial u_k}{\partial x_k}\delta_{ij}\Big) + \frac{2}{3}k\delta_{ij}$$

$$\tau^s{}_{ij} = -\nu^s{}_t\Big(\frac{\partial u_i}{\partial x_j} + \frac{\partial u_j}{\partial x_i} - \frac{2}{3}\frac{\partial u_k}{\partial x_k}\delta_{ij}\Big) + \frac{2}{3}k\delta_{ij}$$

$$\text{all} \quad \frac{\partial}{\partial x} \to 0 \quad \text{in} \quad \tau_{ij} \quad \text{and} \quad \tau^s{}_{ij}$$

$$\chi = -\frac{1}{4}\Big(\frac{k}{\epsilon_s}\Big)^3\Big[\frac{\partial v}{\partial y}\frac{\partial u}{\partial y}\frac{\partial u}{\partial y} + \frac{\partial w}{\partial z}\frac{\partial u}{\partial z}\frac{\partial u}{\partial z} + \Big(\frac{\partial v}{\partial z} + \frac{\partial w}{\partial y}\Big)\frac{\partial u}{\partial y}\frac{\partial u}{\partial z}\Big]$$

The constants are

$$C_\mu = 0.087, C_{\epsilon 1} = 1.4, C_{\epsilon 2} = 2.0, C_{\epsilon 3} = 0.822\sigma_k = 0.32, \sigma_\epsilon = 0.38, \sigma_T = 3.32$$

$$\alpha = 0.52, k_0 = 10^{-6}, \epsilon_0 = 10^{-4}$$

Outside the jet, the flow velocity, pressure and temperature perturbations are small. It is, therefore, sufficient to use the linearized form of (3.1). Also, it is to be noted that in this region there is no turbulence so $k = \epsilon = 0$. Let

$$\begin{aligned} u &= u_\infty + u' \\ v &= v' \\ w &= w' \\ p &= p_\infty + p' \\ T &= T_\infty + T' \end{aligned} \tag{3.2}$$

Substitution of (3.2) into (3.1) and on retaining only lowest order terms, the linearized equations are,

$$u_\infty \frac{\partial u'}{\partial x} = 0 \tag{3.3}$$

$$u_\infty \frac{\partial v'}{\partial x} = -\frac{1}{\rho_\infty}\frac{\partial p'}{\partial y} \tag{3.4}$$

$$u_\infty \frac{\partial w'}{\partial x} = -\frac{1}{\rho_\infty}\frac{\partial p'}{\partial z} \tag{3.5}$$

$$u_\infty \frac{\partial T'}{\partial x} + (\gamma - 1)T_\infty\Big(\frac{\partial u'}{\partial x} + \frac{\partial v'}{\partial y} + \frac{\partial w'}{\partial z}\Big) = 0 \tag{3.6}$$

$$u_\infty \frac{\partial p'}{\partial x} - \frac{u_\infty p_\infty}{T_\infty}\frac{\partial T'}{\partial x} + p_\infty\Big(\frac{\partial u'}{\partial x} + \frac{\partial v'}{\partial y} + \frac{\partial w'}{\partial z}\Big) = 0 \tag{3.7}$$

The integral of (3.3) is

$$u' = 0 \tag{3.8}$$

(3.6) and (3.7) may be integrated, by making use of (3.8), to yield the integral,

$$T' = \frac{\gamma - 1}{\gamma}\frac{T_\infty}{p_\infty}p' \tag{3.9}$$

On account of (3.9), the remaining unknown variables, v', w', and p' are governed by (3.4), (3.5) and the following equation,

$$u_\infty \frac{\partial p'}{\partial x} + \gamma p_\infty\Big(\frac{\partial v'}{\partial y} + \frac{\partial w'}{\partial z}\Big) = 0 \tag{3.10}$$

At some distance away from the jet, the velocity and pressure fields are expected to be small and approximately axisymmetric. In this region, (3.4), (3.5) and (3.10) when written in cylindrical coordinates (r, θ, x) have the form

$$u_\infty \frac{\partial v_r'}{\partial x} + \frac{1}{\rho_\infty}\frac{\partial p'}{\partial r} = 0 \tag{3.11}$$

$$u_\infty \frac{\partial p'}{\partial x} + \gamma p_\infty\Big(\frac{\partial v_r'}{\partial y} + \frac{v_r'}{r}\Big) = 0 \tag{3.12}$$

where v_r' is the radial velocity. If r is large, the last term of (3.12) may be neglected. In this case (3.11) and (3.12) become the simple wave equation and the solution is a function of $\xi = x - \frac{u_\infty}{a_\infty}r$ where $a_\infty = \left(\frac{\gamma p_\infty}{\rho_\infty}\right)^{\frac{1}{2}}$ is the sound speed.

For r not too far from the jet, the last term of (3.12) should be retained. Let us change the independent variables of (3.11) and (3.12) to ξ and r. The equations become,

$$u_\infty \frac{\partial v_r'}{\partial \xi} + \frac{1}{\rho_\infty}\frac{\partial p'}{\partial r} - \frac{u_\infty}{\rho_\infty a_\infty}\frac{\partial p'}{\partial \xi} = 0 \tag{3.13}$$

$$u_\infty \frac{\partial p'}{\partial \xi} + \gamma p_\infty \Big(\frac{\partial v_r'}{\partial r} - \frac{u_\infty}{a_\infty}\frac{\partial v_r'}{\partial \xi} + \frac{v_r'}{r}\Big) = 0 \tag{3.14}$$

Since u_∞ is small, the solution may be expanded as a series in u_∞; i.e.,

$$v_r' = v_0 + u_\infty v_1 + u_\infty^2 v_2 + ..., \qquad p' = p_0 + u_\infty p_1 + u_\infty^2 p_2 + ... \tag{3.15}$$

It is easy to find by substituting (3.15) into (3.13) and (3.14) and after simple integrations, the following formulas for the first two terms of (3.15),

$$v_0 = \frac{\hat{v}_0(\xi)}{r}, \qquad v_1 = \frac{1}{a_\infty}\frac{d\hat{v}_0}{d\xi}, \qquad p_0 = 0, \qquad p_1 = -\rho_\infty \frac{d\hat{v}_0}{d\xi}(\ln r) \tag{3.16}$$

where $\hat{v}_0(\xi)$ is an arbitrary function. By differentiating (3.15) and (3.16) to eliminate $\hat{v}_0(\xi)$, it is straightforward to derive the boundary conditions,

$$\frac{u_\infty}{a_\infty}\frac{\partial v_r'}{\partial x} + \frac{\partial v_r'}{\partial r} + \frac{v_r'}{r} = 0 \tag{3.17}$$

$$\frac{u_\infty}{a_\infty}\frac{\partial p'}{\partial x} + \frac{\partial p'}{\partial r} - \frac{p'}{r(\ln r)} = 0 \tag{3.18}$$

In summary, the boundary conditions for all the flow variables, to be imposed in the jet near field, are

$$u = u_\infty$$

$$\left(\frac{u_\infty}{a_\infty}\frac{\partial}{\partial x} + \frac{\partial}{\partial r} + \frac{1}{r(\ln r)}\right)\begin{bmatrix} v \\ w \end{bmatrix} = 0 \tag{3.19}$$

$$\left(\frac{u_\infty}{a_\infty}\frac{\partial}{\partial x}+\frac{\partial}{\partial r}+\frac{1}{r(\ln r)}\right)\begin{bmatrix} p-p_\infty \\ T-T_\infty \end{bmatrix}=0$$

$$k=\epsilon=0$$

3.2. Mean Flow Refraction Effects

To account for mean flow refraction effect on the radiated sound, Tam and Auriault [23] made use of the adjoint Green's function. The computation of the adjoint Green's function for axisymmetric jets was discussed in detail by Tam and Auriault [25]. Here the method is generalized for application to nonaxisymmetric jets.

Jets evolve slowly in the flow direction. A natural approximation is to regard the mean flow as locally parallel. Tam and Auriault [25] investigated the accuracy of the locally parallel flow approximation and concluded that the approximation would yield good results outside the cone of silence. Since fine-scale turbulence noise is dominant in the sideline and upstream directions that are not in the cone of silence, the locally parallel flow approximation will be used throughout this work.

3.2.1. Adjoint Green's function Formulation

Let $\bar{u}(y,z), \bar{\rho}(y,z)$ and $\bar{p}(y,z)$ be the mean flow velocity, density and pressure distribution of a jet. Let us consider the time harmonic adjoint Green's function, denoted by a subscript 'a'. The governing equations for the adjoint Green's function are (see ref. [25]).

$$
\begin{aligned}
-i\omega u_a - \overline{u}\frac{\partial u_a}{\partial x} - \gamma\overline{p}\frac{\partial p_a}{\partial x} &= 0 \\
-i\omega v_a - \overline{u}\frac{\partial v_a}{\partial x} + u_a\frac{\partial \overline{u}}{\partial y} - \gamma\overline{p}\frac{\partial p_a}{\partial y} &= 0 \\
-i\omega w_a - \overline{u}\frac{\partial w_a}{\partial x} + u_a\frac{\partial \overline{u}}{\partial z} - \gamma\overline{p}\frac{\partial p_a}{\partial z} &= 0 \\
-i\omega p_a - \overline{u}\frac{\partial p_a}{\partial x} - \frac{\partial}{\partial x}\left(\frac{u_a}{\overline{\rho}}\right) - \frac{\partial}{\partial y}\left(\frac{v_a}{\overline{\rho}}\right) - \frac{\partial}{\partial z}\left(\frac{w_a}{\overline{\rho}}\right) &= \frac{1}{2\pi}\delta(\mathbf{x}-\mathbf{x_o})
\end{aligned} \tag{3.20}
$$

where $\mathbf{x_o}$ is the far field observation point at which jet noise is to be measured.

Outside the jet $\bar{u}$ is zero. It is straightforward to find from (3.20) that p_a satisfies the equation

$$
\bigtriangledown^2 p_a + \frac{\omega^2}{a_\infty^2} p_a = \frac{i\omega}{2\pi a_\infty^2}\delta\left(\mathbf{x}-\mathbf{x_o}\right) \tag{3.21}
$$

The solution of (3.21) is

$$
p_a = -\frac{i\omega}{8\pi^2 a_\infty^2}\frac{e^{\frac{i\omega}{a_\infty}|\mathbf{x}-\mathbf{x_o}|}}{|\mathbf{x}-\mathbf{x_o}|} \tag{3.22}
$$

where $|\mathbf{x}-\mathbf{x_o}|$ is the distance between $\mathbf{x}$ and $\mathbf{x_o}$.

For convenience, let the spherical coordinates of $\mathbf{x_o}$ be (R, Θ, ϕ) see Figure 3.1. The polar axis of the spherical coordinate system coincides with the x axis. Θ is the polar angle and ϕ is the azimuthal angle. Here our interest is confined to the far field, namely $R \to \infty$. For large R, we have

$$
|\mathbf{x}-\mathbf{x_o}| \simeq R - \mathbf{x}\cdot\mathbf{x_o}/R = R - \cos\Theta x - \sin\Theta\cos\phi y - \sin\Theta\sin\phi z
$$

By means of the above far field approximation, it is easy to find, from (3.22) and the corresponding formulas for the velocity components, the solution for the adjoint Green's function, as $R \to \infty$, to be

$$\begin{bmatrix} \tilde{u}_a \\ \tilde{v}_a \\ \tilde{w}_a \\ \tilde{p}_a \end{bmatrix} = \frac{-i\omega}{8\pi^2 a_\infty^2 R} \begin{bmatrix} \rho_\infty a_\infty \cos\Theta \\ \rho_\infty a_\infty \sin\Theta\cos\phi \\ \rho_\infty a_\infty \sin\Theta\sin\phi \\ 1 \end{bmatrix} e^{\frac{i\omega}{a_\infty}\left(R - x\cos\Theta - \sin\Theta\cos\phi y - \sin\Theta\sin\phi z - a_\infty t\right)} \tag{3.23}$$

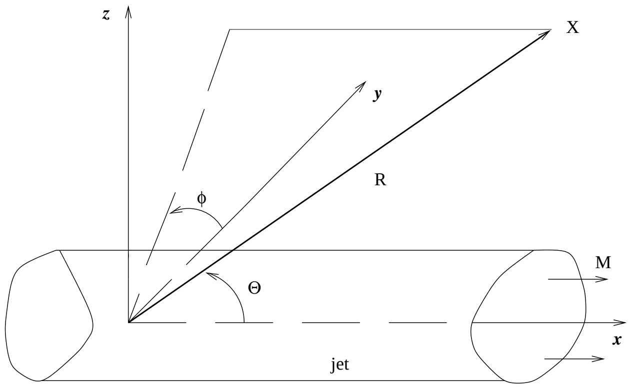

Figure 3.1. Relationship between spherical coordinates (R, Θ, ϕ) and the Cartesian coordinates.

Now the adjoint Green's function of (3.20) may be found as a wave scattering problem by solving the homogeneous equation of (3.20) with (3.23) as the incident wave. This task is greatly simplified by noting that under the locally parallel flow approximation the coefficients of (3.20) are independent of x. Thus the solution must have the same $x-$dependence as the incident wave. In other words,

$$u_a(x, y, z, \omega)e^{-i\omega t} = \tilde{u}_a(y, z, t)e^{-i\frac{\omega}{a_\infty}\cos\Theta x} \tag{3.24}$$

and similarly for the other variables.

By factoring out $e^{-i\frac{\omega}{a_\infty}cos\Theta x}$ and by replacing $-i\omega$ by $\frac{\partial}{\partial t}$ in equation (3.20) to make the equations time dependent, the adjoint Green's function problem becomes a two-dimensional sound scattering problem. The governing equations and the incident waves are as follows,

$$\begin{aligned}
\frac{\partial \tilde{v}_a}{\partial t} + \frac{i\omega\overline{u}\cos\Theta}{a_\infty}\tilde{v}_a + \frac{\partial \overline{u}}{\partial y}\frac{\cos\Theta\gamma\overline{p}}{(a_\infty - \overline{u}\cos\Theta)}\tilde{p}_a - \gamma\overline{p}\frac{\partial \tilde{p}_a}{\partial y} &= 0 \\
\frac{\partial \tilde{w}_a}{\partial t} + \frac{i\omega\overline{u}\cos\Theta}{a_\infty}\tilde{w}_a + \frac{\partial \overline{u}}{\partial z}\frac{\cos\Theta\gamma\overline{p}}{(a_\infty - \overline{u}\cos\Theta)}\tilde{p}_a - \gamma\overline{p}\frac{\partial \tilde{p}_a}{\partial z} &= 0 \\
\frac{\partial \tilde{p}_a}{\partial t} + \frac{i\omega\overline{u}\cos\Theta}{a_\infty}\tilde{p}_a + \frac{i\omega}{a_\infty}\frac{\cos^2\Theta\ \overline{a}^2}{(a_\infty - \overline{u}\cos\Theta)}\tilde{p}_a - \frac{\partial}{\partial y}\left(\frac{\tilde{v}_a}{\overline{\rho}}\right) - \frac{\partial}{\partial z}\left(\frac{\tilde{w}_a}{\overline{\rho}}\right) &= 0
\end{aligned} \tag{3.25}$$

Outside the jet, the incident wave is

$$\begin{bmatrix} \tilde{v}_a \\ \tilde{w}_a \\ \tilde{p}_a \end{bmatrix} \rightarrow \frac{-i\omega}{8\pi^2 a_\infty^2 R}\begin{bmatrix} \rho_\infty a_\infty \sin\Theta\cos\phi \\ \rho_\infty a_\infty \sin\Theta\sin\phi \\ 1 \end{bmatrix} e^{\frac{i\omega}{a_\infty}\left(R - \sin\Theta\cos\phi y - \sin\Theta\sin\phi z - a_\infty t\right)} \tag{3.26}$$

In deriving (3.25), the relationship

$$\tilde{u}_a = \frac{\cos\Theta\gamma\overline{p}}{(a_\infty - \overline{u}\cos\Theta)}\tilde{p}_a \tag{3.27}$$

which is the integral of the first equation of (3.20), has been used.

3.2.2 Numerical Implementation

For a given $\bar{u}(y,z)$, $\bar{\rho}(y,z)$ and $\bar{p}(y,z)$ the sound scattering problem of (3.25) and (3.26) may be solved computationally. For this purpose, (3.25) is discretized according to the 7-point stencil DRP scheme [42], [59] in a rectangular computational domain as shown in Figure 3.2. The outer boundary of the computational domain is taken to be where the mean flow $\bar{u}$ differs from u_∞ by 0.1% of u_j.

This choice assures that a larger computational domain is used for $x-$stations further downstream from the nozzle exit. The mesh size is set by the smaller of two criteria. To ensure the DRP scheme has sufficient spatial resolution for the incident and the scattered acoustic waves, no less than 7 mesh spacings per acoustic wavelength is used. That is, a finer mesh is automatically used for high frequency waves. To make certain that the refraction of sound by the mixing layer of the jet is accurately computed, a minimum of 8 mesh spacings is used per half-width of the layer. To eliminate spurious numerical waves that may inadvertently be generated at the boundaries of the computational domain, artificial selective damping terms [59], [60] are added to the discretized equations. The artificial selective damping terms damp the short waves without affecting the physical (long) waves. The inverse mesh Reynolds number of the damping terms is given a value of 0.05. This value has been found to yield very satisfactory results.

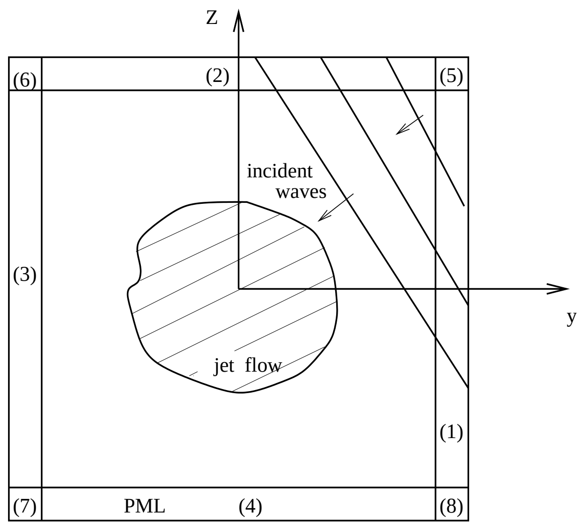

Figure 3.2. Computational domain showing the jet flow, incident sound waves and the perfectly matched layer (PML).

As shown in Figure 3.2, the computational domain is surrounded by a perfectly matched layer (PML). The PML has a thickness of 15 mesh points. In this layer the flow variables are split into two parts: the split variable method [61]. One part of the variables will be assigned the values of the incident wave given by (3.26). The other part is the scattered waves. The scattered waves are damped by the built-in damping of the PML. The layer is called perfectly matched because, in principle, there is no reflected wave back into the computation domain. The construction of the PML is discussed in the Appendix A.

For a given direction of radiation and frequency, the incident wave (3.26) is completely specified. To start the computation, initial conditions are required. In this work, the incident wave is used as the starting condition. The solution is marched in time until a time periodic state is attained. At this time, the maximum absolute value of $\tilde{p}_a$ over a cycle is measured at every point in the jet. This is the absolute value of the adjoint Green's function $|p_a|$ needed for noise computation.

3.3. Comparisons with Experimental Measurements

The first step in implementing formula (1.1) and (1.2) is to compute the mean flow using (3.1), the parabolized RANS equations. To start the calculation at the nozzle exit, it is assumed that the mean flow is uniform surrounded by a thin mixing layer with a Gaussian profile. The half-width of the mixing layer is taken to be 1.5% to 2% of the equivalent diameter, D_{eq}, of the nozzle. The equivalent diameter is the diameter of a circular nozzle with the same area. Experience indicates that a small variation of the initial half-width of the mixing layer has little effect on the radiated noise (a 50% change in half-width results in 0.5 dB noise level change). It affects only slightly the high frequency part of the spectrum.

It is well known that a nonaxisymmetric jet tends to become less asymmetric in the downstream direction. This is confirmed in the present numerical results. Figure 3.3 shows the computed contours of the axial velocity component of a Mach 2 jet at a temperature ratio 1.8 (reservoir to ambient temperature) from a rectangular nozzle of aspect ratio 7.6. The first quadrant is for the flow at $x = 1D_{eg}$ downstream. The second, third and fourth quadrants are for the mean flow at 5, 10 and 15 D_{eq} downstream. The contours clearly show the tendency to become more and more circular. Figure 3.4 shows a similar plot for a cold subsonic jet at Mach 0.8 from an aspect ratio 8 rectangular nozzle. Again, the velocity contours tend to evolve into a circular shape. A comparison between Figure 3.3 and 3.4 confirms the expectation that a subsonic rectangular jet would transform into a circular jet faster than a supersonic jet. This is not surprising since the axial scale for a jet is the core length. The potential core of a supersonic jet is much longer than that of a subsonic jet in terms of equivalent nozzle diameter.

Only a limited number of sets of nonaxisymmetric jet noise data are available for comparisons with predictions. Here two sets of supersonic Mach number data will be used. One from an elliptic jet of aspect ratio 3, the other from a rectangular jet of aspect ratio 7.6, measured by Seiner and coworkers [62] at the jet Noise Laboratory of the NASA Langley Research Center. The design Mach number of the nozzles of these jets is 2.0. The data are of high quality, comparable to the axisymmetric jet noise data used for comparison in references [20] and [23]. Zaman [63] measured subsonic jet noise spectra from an elliptic nozzle of aspect ratio 3 and rectangular nozzles of aspect ratios 3 and 8 along the major and minor axis directions. Since the facility used was only semi-anechoic, the quality of the data is less good but still acceptable. The above are the experimental data available to us for comparisons with theoretical predictions.

Figures 3.5a, b and c show comparisons between calculated and measured noise spectra [62] for the aspect ratio 3, Mach 2 elliptic jet at a temperature ratio 1.0. The polar angle Θ (exhaust angle) of the measurement microphone is at 90 degrees. Figure 3.5a is the spectrum measured in the major axis plane ($\phi = 90^o$). Figure 3.5b is the noise spectrum radiated in the direction of the minor axis plane ($\phi = 0^o$). Figure 3.5c is the noise spectrum at $\phi = 58^o$.

Figures 3.6a, b and c are for the same jet as Figure 3.5. Here Θ is 72 degrees. Figure 3.6a is for radiation in the major axis plane ($\phi = 90^o$). Figure 3.6b is for radiation in the minor axis plane ($\phi = 0^o$). Figure 3.6c is the noise spectrum radiated in the $\phi = 58^o$ direction.

Figure 3.7 gives the comparisons between the calculated noise spectra and the experimental measurements [62] of a Mach 2 aspect ratio 7.6 rectangular jet at temperature ratio 1.8. The data are for $\Theta = 90^o$ plane. Figure 3.7a is the spectrum of the noise radiated in the major axis plane direction. Figure 3.7b is that in the minor axis plane direction.

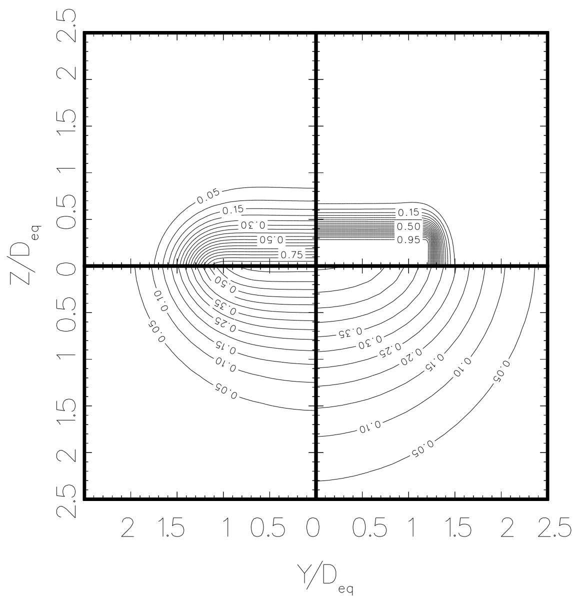

Figure 3.3. Contours of the axial velocity component of a Mach 2 jet at temperature ratio 1.8 from a rectangular nozzle of aspect ratio 7.6. First, second, third and fourth quadrant are for cross sections at $X/D_{eq} = 1, 5, 10, 15$.

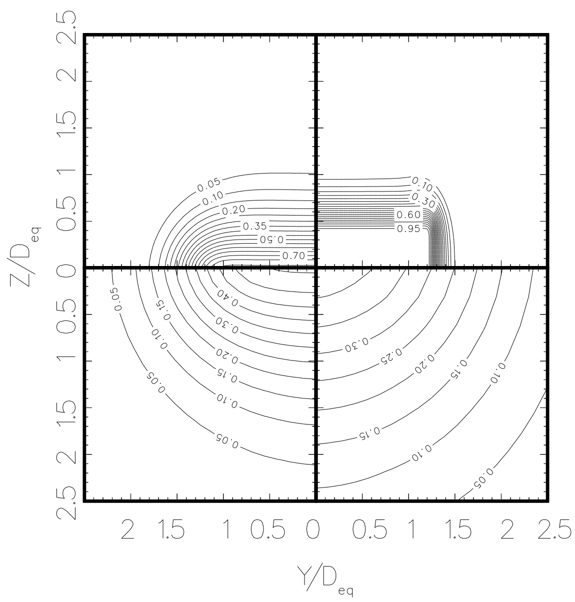

Figure 3.4. Contours of the axial velocity component of a Mach 0.82 cold jet from a rectangular nozzle of aspect ratio 8. First, second, third and fourth quadrant are for cross sections at $X/D_{eq} = 1, 5, 10, 15$.

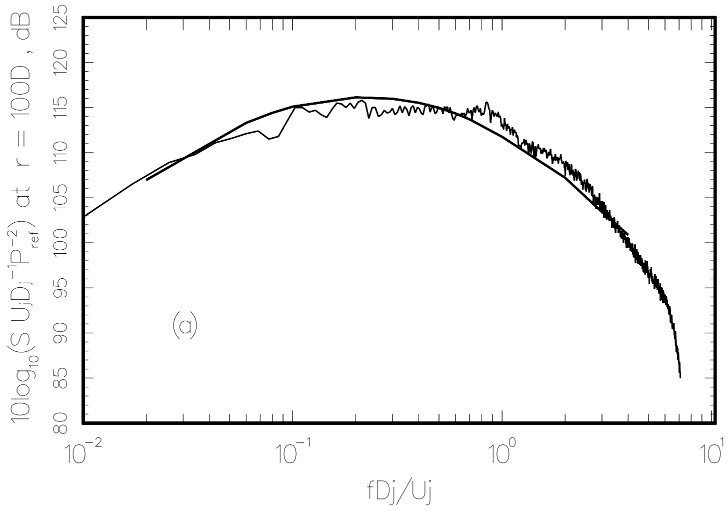

Figure 3.5a. Noise spectra of an aspect ratio 3 elliptic jet at Mach 2.0, $T_r/T_\infty = 1.0$. Data from *Seiner*[62], ——— computed spectra. $\Theta = 90°$. a. Major axis plane ($\phi = 90°$), b. Minor axis plane ($\phi = 0°$), c. $\phi = 58°$ plane.

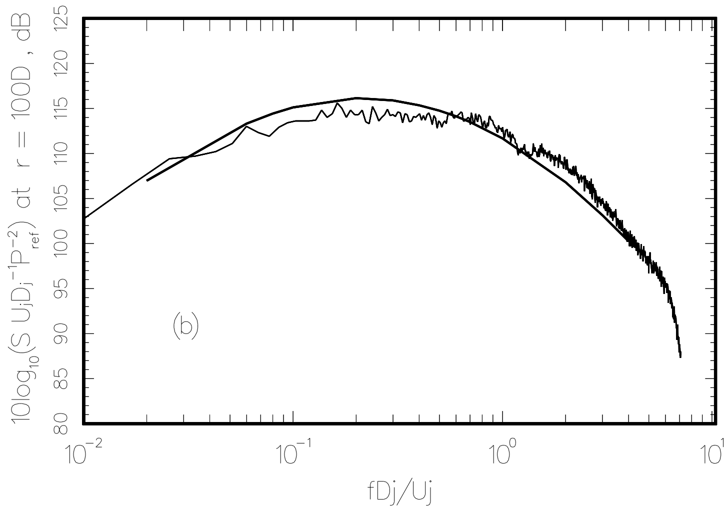

Figure 3.5b. Minor axis plane ($\phi = 0^o$).

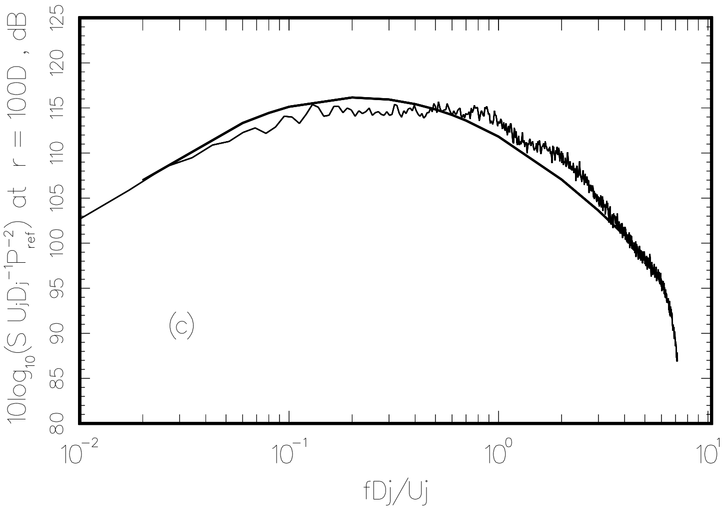

Figure 3.5c. ($\phi = 58^o$) plane.

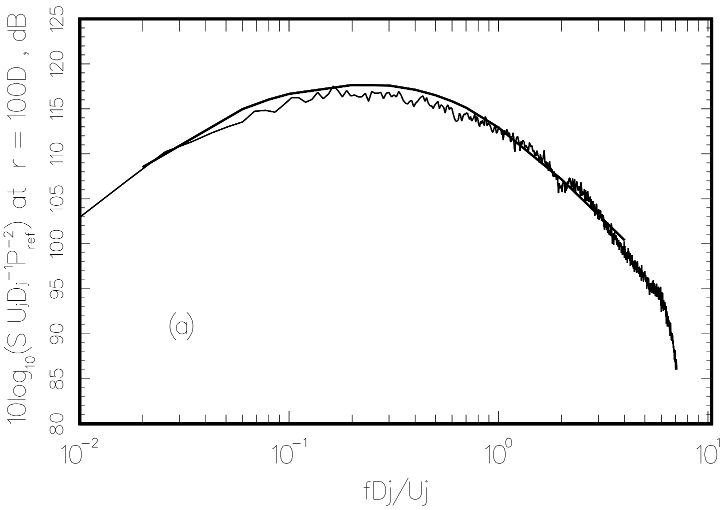

Figure 3.6a. Noise spectra of an aspect ratio 3 elliptic jet at Mach 2.0, $T_r/T_\infty = 1.0$. Data from *Seiner*[62], ——— computed spectra. $\Theta = 72°$. a. Major axis plane ($\phi = 90°$), b. Minor axis plane ($\phi = 0°$), c. $\phi = 58°$ plane.

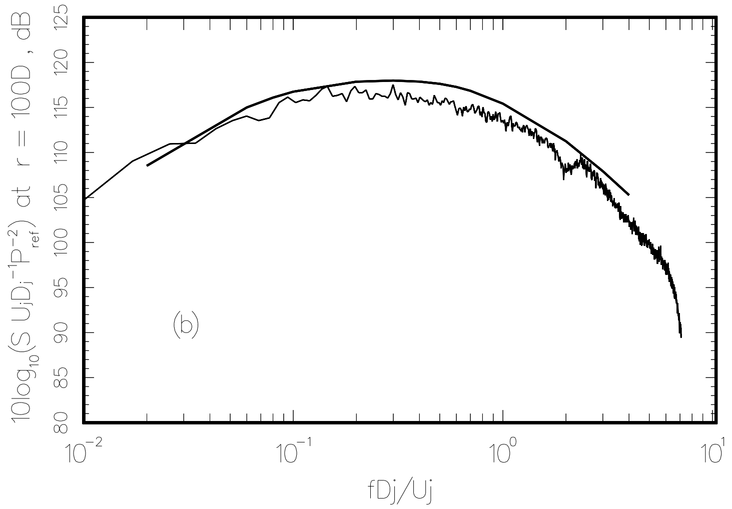

Figure 3.6b. Minor axis plane ($\phi = 0^o$).

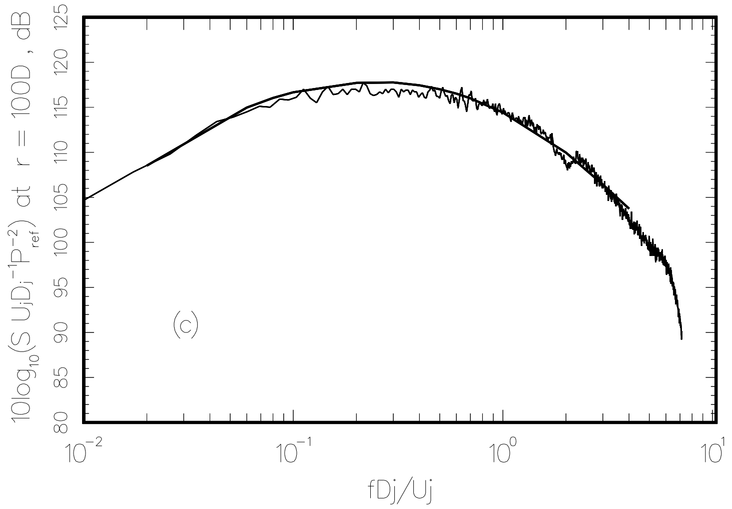

Figure 3.6c. ($\phi = 58^o$) plane.

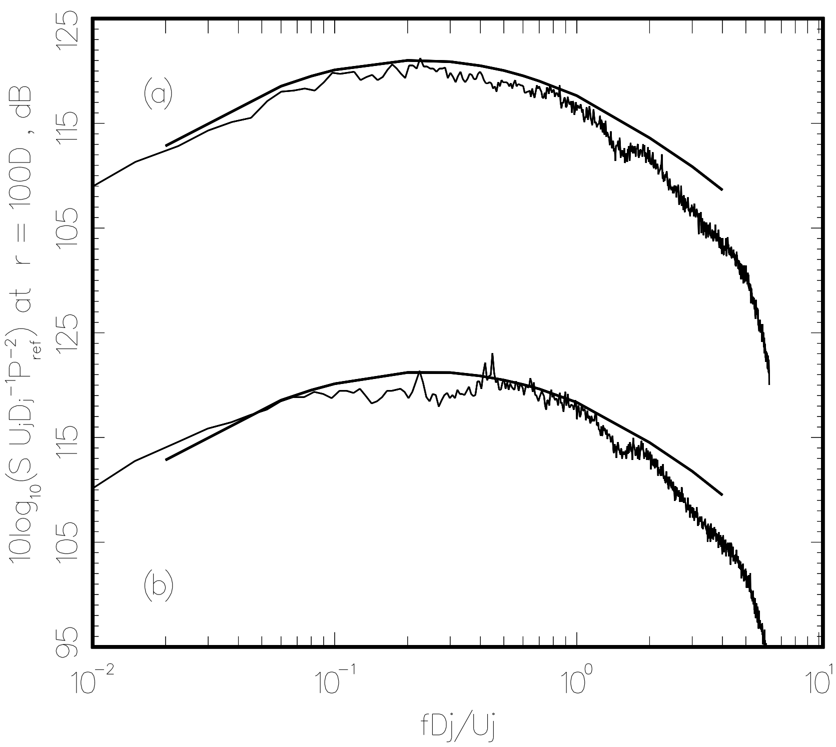

Figure 3.7. Noise spectra of an aspect ratio 7.6 rectangular jet at Mach 2.0, $T_r/T_\infty = 1.8$. Data from $Seiner$[62], ——— computed spectra. $\Theta = 90°$. a. Major axis plane , b. Minor axis plane .

Figure 3.8 is for the same jet as Figure 3.7. In this case the polar angle is $\Theta = 72^o$. The full curve is the calculated noise spectrum in the major axis direction, $\phi = 90^o$. The dotted curve is the predicted spectrum in the minor axis direction ($\phi = 0^o$). It is quite clear that at this polar angle, the directivity is nonaxisymmetric with more noise radiated in the minor axis plane. The main reason for the asymmetry is the mean flow refraction effect. Surrounding the two ends of the major axis of a large aspect ratio rectangular jet are thick mixing layers. They cause strong refraction to sound radiation. This contributes to a reduction of noise radiation in those directions. As can be seen, the calculated results seem to follow the measured data except at very high frequencies.

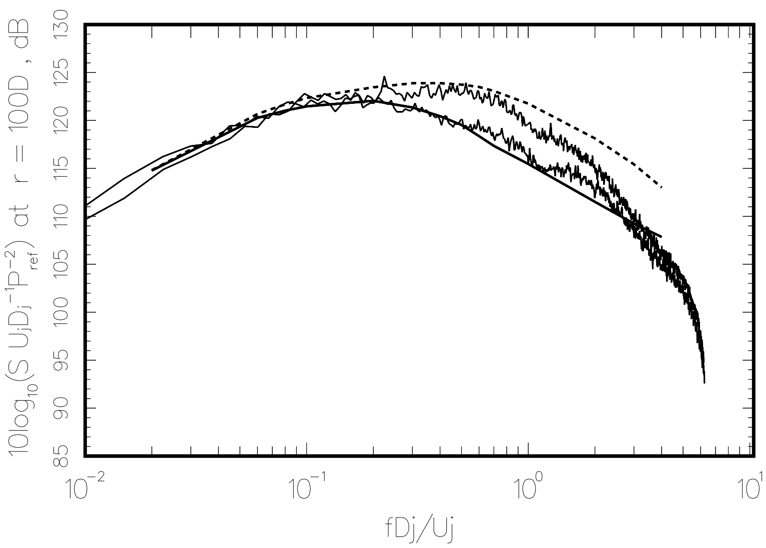

Figure 3.8. Noise spectra of an aspect ratio 7.6 rectangular jet at Mach 2.0, $T_r/T_\infty = 1.8$. Data from $Seiner$[62]. $\Theta = 72°$. Computed spectra, ——— major axis plane ; - - - - minor axis plane .

Figure 3.9 shows the noise spectra for the aspect ratio 3 elliptic jet at temperature ratio 1.0 and Mach number 0.82 measured by Zaman [63]. Shown in this figure also are the calculated noise spectra. Curve "a" is the noise spectrum at $\Theta = 90^o$ and $\phi = 90^o$ (the major axis plane). Curve "b" is the noise spectrum at $\Theta = 90^o$ and $\phi = 0^o$ (the minor axis plane). Figure 3.10 shows the measured spectra for a similar rectangular jet (same aspect ratio, temperature ratio and Mach number). The calculated noise spectra are also provided.

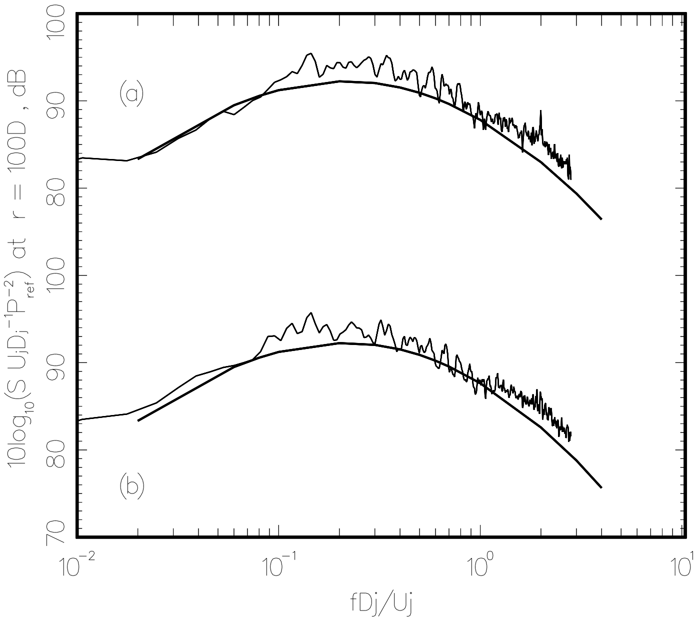

Figure 3.9. Noise spectra of an aspect ratio 3 elliptic jet at Mach 0.82, $T_r/T_\infty = 1.0$. Data from *Zaman*[63], ——— computed spectra. $\Theta = 90°$. a. Major axis plane , b. Minor axis plane .

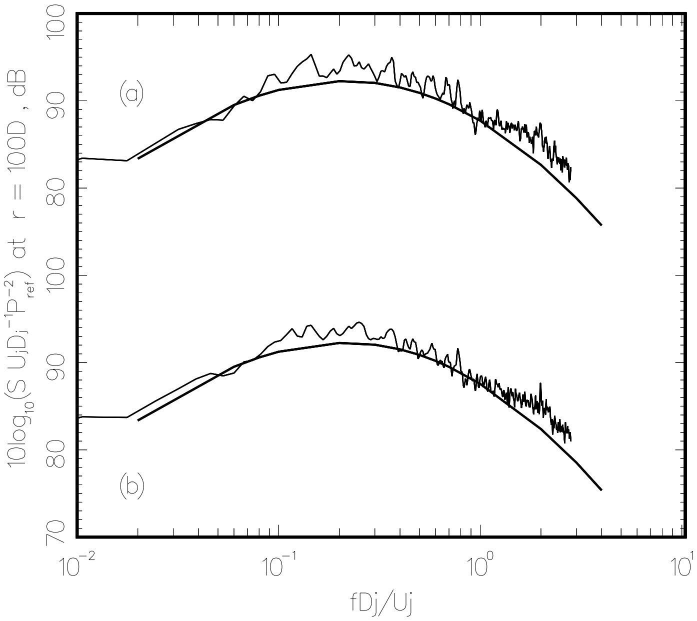

Figure 3.10. Noise spectra of an aspect ratio 3 rectangular jet at Mach 0.82, $T_r/T_\infty = 1.0$. Data from *Zaman*[63], ——— computed spectra. $\Theta = 90°$. a. Major axis plane , b. Minor axis plane .

Finally, Figure 3.11 shows the noise spectra of a large aspect ratio rectangular jet (aspect ratio 8) at Mach 0.82 and temperature ratio 1.0. The smooth curves in the figures are the calculated noise spectra. Both the calculated and measured spectra are for noise radiation in the $\Theta = 90^o$ plane. Curve a is for radiation in the major axis plane ($\phi = 90^o$) while curve b is for radiation in the minor axis plane ($\phi = 0^o$). Overall, there is good agreement (within 2%) between the spectrum calculated by equations (1.1) and (1.2) of the Tam and Auriault theory [23] and the measured spectrum in each of the above cases.

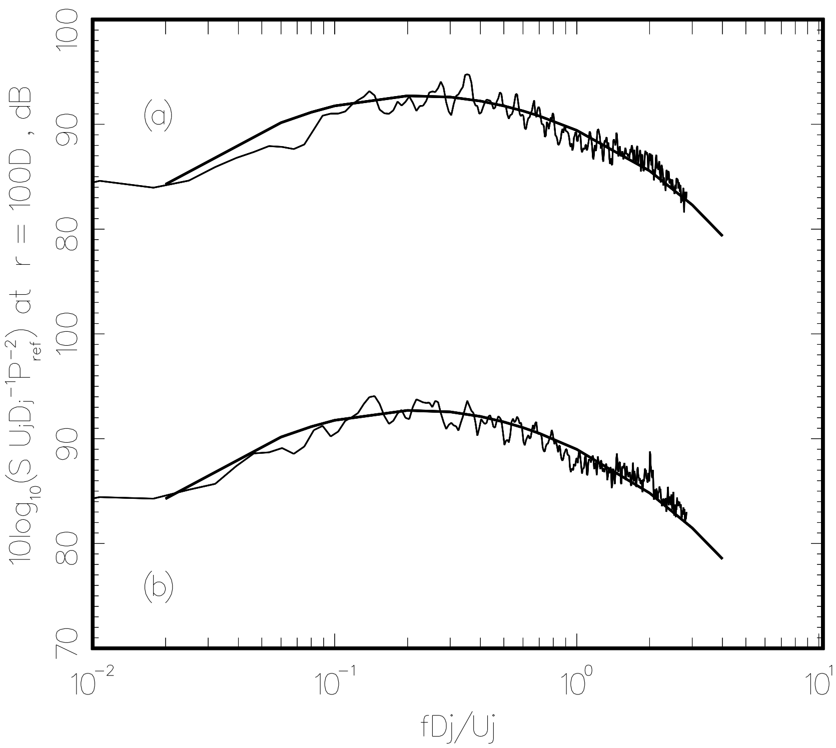

Figure 3.11. Noise spectra of an aspect ratio 8.0 rectangular jet at Mach 0.82, $T_r/T_\infty = 1.0$. Data from $Zaman$[63], ——— computed spectra. $\Theta = 90°$. a. Major axis plane , b. Minor axis plane .

CHAPTER IV

NOISE FROM THE FINE SCALE TURBULENCE OF AN INSTALLED JET

A jet installed under a wing of an aircraft radiates more noise than the same jet in the stand-alone condition [26-32]. There have been lots of activities, in the recent past, focussed on developing jet noise reduction concept with no significant performance loss. All these studies have focused on isolated jets. Several investigators have studied the problem of jet and wing/flap interaction noise [26-28], [64-67] involving model-scale testing under both static conditions and simulated flight condition in an open wind tunnel. For example, Wang [27] conducted a static model-scale study of jet-wing interaction noise (flaps retracted). Sengupta [65] studied the noise from 1/3 scale model, simulating the 757 wing-flap system, and a single flow nozzle simulating the engine under static conditions. Miller [66] looked at the flight effects on the same airplane model used by Sengupta. He used a dual flow jet instead of a single stream jet. Brown and Ahuja [67] conducted an extensive parametric study of installation effects. The test configuration consisted of a two-dimensional wing with a single slotted flap and a detached circular nozzle to simulate the engine. However, none of these studies involved realistic airplane and engine configurations.

Recently, as a part of NASA's Advanced Subsonic Technology Noise Reduction Program, a series of experiments on installation noise was performed by engineers of the Boeing Company [30-32]. They employed an open wind tunnel at Mach 0.28 to stimulate the forward motion of the airplane. Based in the data from the experiment, an empirical prediction procedure of installed jet noise was developed. However, the prediction has little flow physics and performs poorly at high Strouhal numbers. At the present time this is the only available installed jet noise prediction method.

In this chapter, the jet noise theory of Tam and Auriault [23] is extended to installed jets. The flow effect and reflection from the wing are included in the theory through extension of the adjoint Green's function approach of Chapter 3. The equations used in Chapter 1 are reformulated to account for the downwash of the turbulent jet flow around the wing and the flap.

4.1. Wind Tunnel Simulation of Installation Effects

Figure 4.1 shows the Boeing experimental set-up. The airplane model is mounted in the potential core of the open wind tunnel inside an anechoic chamber. Far-field elliptic mirror microphones and the newly developed phase array microphones are placed outside the wind-tunnel flow. The jet is issued from a separated flow nozzle with a bypass ratio of about 6. The scale of the airplane model used in the experiment is 0.048. The left wing of the model consists of a cruise wing (flap deployed at 0 deg) with no nacelles. The right wing consists of an adjustable flap and a flow-through nacelle. The flaps were positioned to simulate the cruise wing, a take-off flap setting and a landing flap setting. In the nozzle-fixed coordinate system, the flow around the jet is no different from that of the jet in actual flight. However, because of the presence of an outer shear layer surrounding the wind tunnel, there is a flow refraction effect. The refraction effect of the outer shear layer is taken into account through the adjoint Green's function.

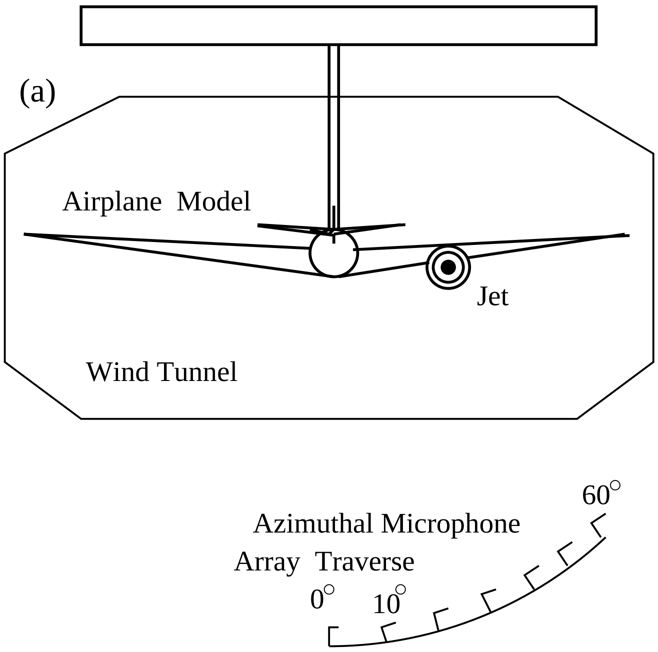

Figure 4.1a. The Boeing experimental set-up [30-32]. a. End Viev, b. Side view.

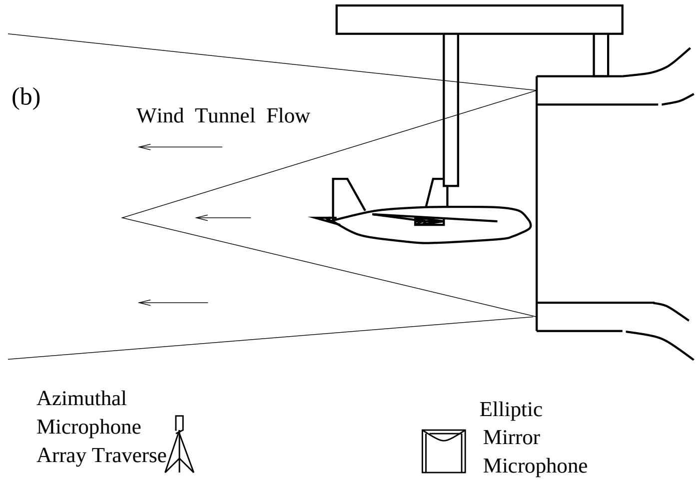

Figure 4.1b. Side view.

4.2. Mathematical Model for the Prediction of Installation Effects

The geometry of the installed jet engine system is quite complicated (Figure 1.4). Experimental measurements indicate, however, that the noise levels are insensitive to the engine installation location and the width of the bifurcation.

Figure 4.2 shows the installed jet model used in the present work. It is assumed that the nozzle exit is aligned with the tip of the wing, with the jet axis parallel to the chord line of the wing. The coaxial jet used in the experiment is modeled by a single circular jet with equivalent mass flow. The nozzle diameter is $0.22c$, where c is the chord length. The wing is assumed to be two-dimensional as its aspect ratio is very large.

To compute the far-field installation noise noise, the problem is divided into three parts. First, the flow around the wing/flap is calculated (without the jet). Next, the jet flow is computed, using the $k-\epsilon$ turbulence model, with the wing/flap flow as the boundary condition outside the jet. Finally, the turbulence field of the distorted jet is used as input into the Tam and Auriault [23] fine-scale turbulence noise theory to find the radiated noise.

4.3. Computation of Mean Flow and Turbulence

As stated before, the first step in implementing the computational model, is to calculate the flow around the wing/flap due to the forward flight. The purpose of the calculation is to determine the downwash. The downwash is responsible for distorting the cross section of the jet. Since the distance between the outer edge of the jet shear layer and the wing/flap is never less than a quarter of the chord length (even for the undisturbed jet, without downwash), inviscid Euler equations are used to calculate the wing/flap flow.

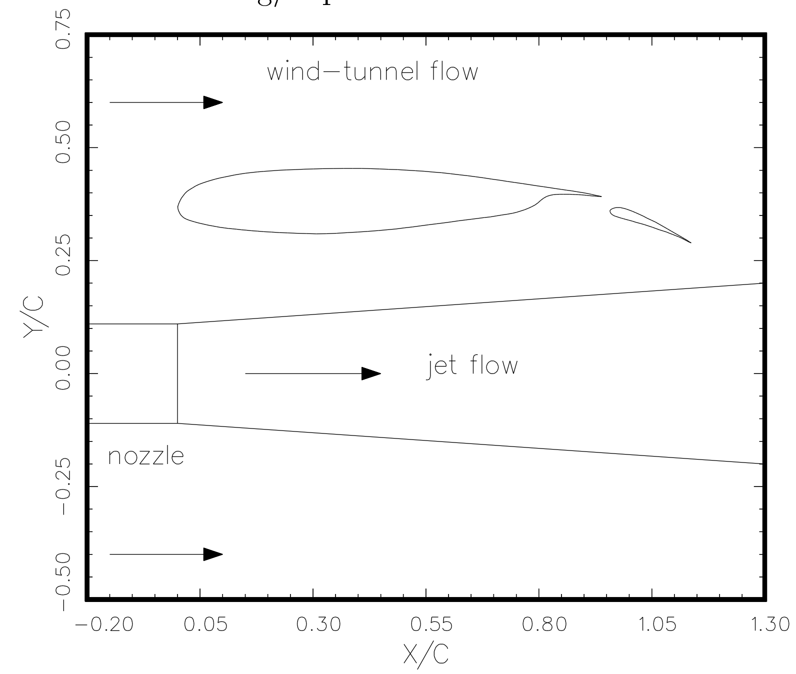

Figure 4.2. Installed jet model.

Let us denote the wing-flap flow by a superscript 'a'. The governing equations are

$$\begin{aligned}
\frac{\partial \rho^{(a)}}{\partial t} + \frac{\partial \rho^{(a)} u^{(a)}}{\partial x} + \frac{\partial \rho^{(a)} v^{(a)}}{\partial y} &= 0 \\
\frac{\partial u^{(a)}}{\partial t} + u^{(a)} \frac{\partial u^{(a)}}{\partial x} + v^{(a)} \frac{\partial u^{(a)}}{\partial y} &= -\frac{1}{\rho^{(a)}} \frac{\partial p^{(a)}}{\partial x} \\
\frac{\partial v^{(a)}}{\partial t} + u^{(a)} \frac{\partial v^{(a)}}{\partial x} + v^{(a)} \frac{\partial v^{(a)}}{\partial y} &= -\frac{1}{\rho^{(a)}} \frac{\partial p^{(a)}}{\partial y} \\
\frac{\partial p^{(a)}}{\partial t} + u^{(a)} \frac{\partial p^{(a)}}{\partial x} + v^{(a)} \frac{\partial p^{(a)}}{\partial y} + \gamma p^{(a)} \Big(\frac{\partial u^{(a)}}{\partial x} + \frac{\partial v^{(a)}}{\partial y} \Big) &= 0
\end{aligned} \tag{4.1}$$

The solution is obtained by means of the DRP scheme [42]. Using an initial condition of zero flow, the solution is marched in time until a steady state is attained. Radiation and outflow boundary conditions [37] are imposed on the outer boundaries of the computational domain. On the wall surface of the wing and flap the wall boundary condition is enforced by means of the ghost point method. Details of the ghost point method can be found in reference [33].

Figure 4.3 shows streamlines around the wing/flap at various flap settings. The forward flight Mach number is 0.2. For illustration purposes, an undisturbed jet with temperature ratio 2.8 at Mach 0.9 is included in the figure. Figure 4.3a shows the streamlines for the case of the flap deployed at 0^o (cruise configuration). It can be seen that the wing/flap flow exerts very little influence on the jet. However, there exists a small positive pressure gradient in the y direction. Therefore, the jet is expected to be circular and slightly shifted towards the wing.

Figure 4.3b is for the flap angle set at 23^o (typical take-off configuration). Here steep velocity gradients and a strong downwash downstream of the trailing edge of the flap are created. The installed jet is expected to be somewhat distorted as compared to an isolated jet. This effect will be even more pronounced in the case where the flap is deployed at 35^o (typical landing configuration). This is shown in Figure 4.3c.

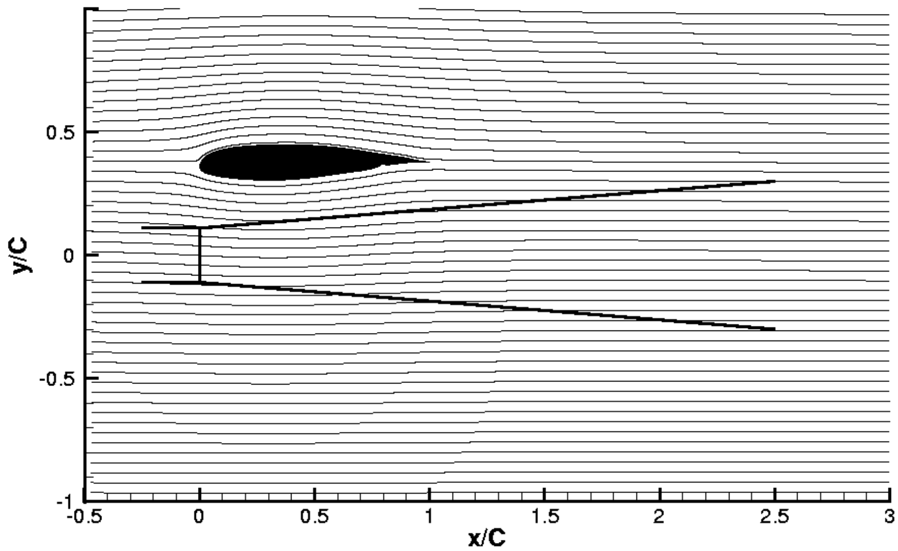

Figure 4.3a. Streamlines around the wing/flap due to forward flight at Mach 0.2. Flap deflection angle 0^o.

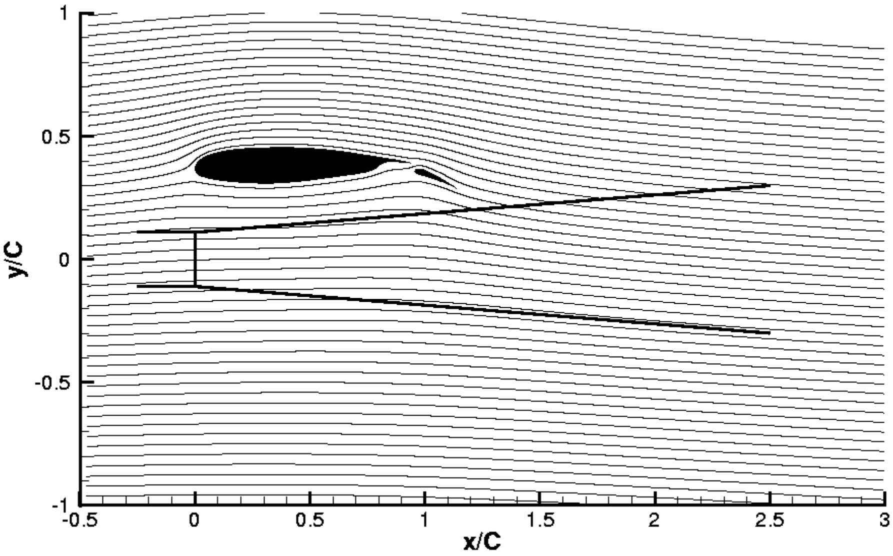

Figure 4.3b. Streamlines around the wing/flap due to forward flight at Mach 0.2. Flap deflection angle 23^o.

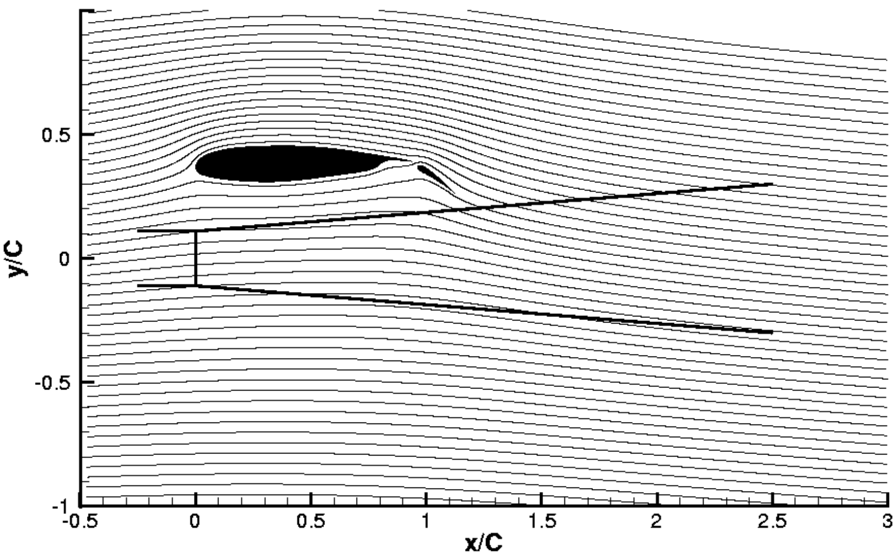

Figure 4.3c. Streamlines around the wing/flap due to forward flight at Mach 0.2. Flap deflection angle 35^o.

4.3.1. The Governing Equations for Installed Jet

In this section the parabolized RANS equations (3.1) are modified and reformulated to compute the turbulent jet flow. Let ρ_j, T_j, and u_j be the mean density, temperature and axial velocity, respectively, at the center of the nozzle exit. On scaling ρ by ρ_j, u_k by u_j, T by T_j, p by $\rho_j u_j^2$, k by u_j^2, and ϵ and ϵ_s by u_j^3/D, x_j by D, where D is the nozzle diameter, the nondimensional steady state RANS equations are:

$$\frac{\partial \rho u}{\partial x} + \frac{\partial \rho u}{\partial y} + \frac{\partial \rho w}{\partial z} = 0$$

$$\rho\Big[u\frac{\partial u}{\partial x} + v\frac{\partial u}{\partial y} + w\frac{\partial u}{\partial z}\Big] = -\frac{\partial p}{\partial x} - \frac{\partial(\rho\tau_{xx})}{\partial x} - \frac{\partial(\rho\tau_{xy})}{\partial y} - \frac{\partial(\rho\tau_{xz})}{\partial z}$$

$$\rho\Big[u\frac{\partial v}{\partial x} + v\frac{\partial v}{\partial y} + w\frac{\partial v}{\partial z}\Big] = -\frac{\partial p}{\partial y} - \frac{\partial(\rho\tau_{yx})}{\partial x} - \frac{\partial(\rho\tau_{yy})}{\partial y} - \frac{\partial(\rho\tau_{yz})}{\partial z}$$

$$\rho\Big[u\frac{\partial w}{\partial x} + v\frac{\partial w}{\partial y} + w\frac{\partial w}{\partial z}\Big] = -\frac{\partial p}{\partial z} - \frac{\partial(\rho\tau_{zx})}{\partial x} - \frac{\partial(\rho\tau_{zy})}{\partial y} - \frac{\partial(\rho\tau_{zz})}{\partial z}$$

$$\rho\Big[u\frac{\partial T}{\partial x} + v\frac{\partial T}{\partial y} + w\frac{\partial T}{\partial z}\Big] = -\gamma(\gamma-1){M_j}^2 p\Big(\frac{\partial u}{\partial x} + \frac{\partial v}{\partial y} + \frac{\partial w}{\partial z}\Big) + \gamma(\gamma-1){M_j}^2\rho\epsilon$$
$$+\frac{1}{\sigma_T}\Big[\frac{\partial}{\partial x}(\rho\nu_t\frac{\partial T}{\partial x}) + \frac{\partial}{\partial y}(\rho\nu_t\frac{\partial T}{\partial y}) + \frac{\partial}{\partial z}(\rho\nu_t\frac{\partial T}{\partial z})\Big] \tag{4.2}$$

$$u\frac{\partial k}{\partial x} + v\frac{\partial k}{\partial y} + w\frac{\partial k}{\partial z} = -\epsilon - \tau_{xx}\frac{\partial u}{\partial x} - \tau_{xy}\frac{\partial u}{\partial y} - \tau_{xz}\frac{\partial u}{\partial z} - \tau_{yx}\frac{\partial v}{\partial x} - \tau_{yy}\frac{\partial v}{\partial y} - \tau_{yz}\frac{\partial v}{\partial z}$$
$$-\tau_{zx}\frac{\partial w}{\partial x} - \tau_{zy}\frac{\partial w}{\partial y} - \tau_{zz}\frac{\partial w}{\partial z} + \frac{1}{\rho\sigma_k}\Big[\frac{\partial}{\partial x}(\rho\nu_t\frac{\partial k}{\partial x}) + \frac{\partial}{\partial y}(\rho\nu_t\frac{\partial k}{\partial y}) + \frac{\partial}{\partial z}(\rho\nu_t\frac{\partial k}{\partial z})\Big]$$

$$u\frac{\partial \epsilon_s}{\partial x} + v\frac{\partial \epsilon_s}{\partial y} + w\frac{\partial \epsilon_s}{\partial z} = -\frac{C_{\epsilon_1}\epsilon_s}{k}\Big[{\tau^s}_{xx}\frac{\partial u}{\partial x} + {\tau^s}_{xy}\frac{\partial u}{\partial y} + {\tau^s}_{xz}\frac{\partial u}{\partial z} + {\tau^s}_{yx}\frac{\partial v}{\partial x} + {\tau^s}_{yy}\frac{\partial v}{\partial y}\Big]$$
$$+{\tau^s}_{yz}\frac{\partial v}{\partial z} + {\tau^s}_{zx}\frac{\partial w}{\partial x} + {\tau^s}_{zy}\frac{\partial w}{\partial y} + {\tau^s}_{zz}\frac{\partial w}{\partial z} - (C_{\epsilon_2} - C_{\epsilon_3}\chi)\frac{{\epsilon_s}^2}{k}$$
$$+\frac{1}{\rho\sigma_\epsilon}\Big[\frac{\partial}{\partial x}(\rho{\nu^s}_t\frac{\partial \epsilon_s}{\partial x}) + \frac{\partial}{\partial y}(\rho{\nu^s}_t\frac{\partial \epsilon_s}{\partial y}) + \frac{\partial}{\partial z}(\rho{\nu^s}_t\frac{\partial \epsilon_s}{\partial z})\Big]$$

$$\rho = \gamma {M_j}^2 \frac{p}{T}$$

$$\epsilon = \epsilon_s(1 + \alpha M_t^2), \quad M_t^2 = \frac{2k}{T} M_j^2$$

$$\nu_t = C_\mu \frac{k^2}{\epsilon + \epsilon_0}, \qquad {\nu^s}_t = C_\mu \frac{k^2}{\epsilon_s + \epsilon_0}$$

$$\tau_{ij} = -\nu_t\Big(\frac{\partial u_i}{\partial x_j} + \frac{\partial u_j}{\partial x_i} - \frac{2}{3}\frac{\partial u_k}{\partial x_k}\delta_{ij}\Big) + \frac{2}{3}k\delta_{ij}$$

$${\tau^s}_{ij} = -{\nu^s}_t\Big(\frac{\partial u_i}{\partial x_j} + \frac{\partial u_j}{\partial x_i} - \frac{2}{3}\frac{\partial u_k}{\partial x_k}\delta_{ij}\Big) + \frac{2}{3}k\delta_{ij}$$

$$\chi = \omega_{ij}\omega_{jk}s_{ki}$$

$$\omega_{ij} = \frac{1}{2}\frac{k}{\epsilon_s}\left(\frac{\partial u_i}{\partial x_j} - \frac{\partial u_j}{\partial x_i}\right)$$

$$s_{ij} = \frac{1}{2}\frac{k}{\epsilon_s}\left(\frac{\partial u_i}{\partial x_j} + \frac{\partial u_j}{\partial x_i}\right)$$

For flight Mach number at take-offs and landings, the solution of (4.1) is nearly incompressible. For simplicity we will assume that it is, i.e.

$$\frac{\partial u_j^{(a)}}{\partial x_j} = 0 \tag{4.3}$$

Since the incoming flow is uniform (irrotational) and the fluid is inviscid, the flow remains irrotational. Thus the velocity field is governed by the gradient of a potential Φ.

$$u_i^{(a)} = \frac{\partial \Phi}{\partial x_i} \tag{4.4}$$

Substitution (4.4) into (4.3) yields

$$\frac{\partial^2 u_i^{(a)}}{\partial x_j^2} = 0 \tag{4.5}$$

The variables to be determined by the parabolized equations are p, T, and u_i, ϵ, k. ρ is found by the equation of state.

Let

$$
\begin{aligned}
p &= p^{(a)} + \hat{p} \\
T &= T^{(a)} + \hat{T} \qquad (4.6) \\
u_i &= {u_i}^{(a)} + \hat{u}_i
\end{aligned}
$$

k and ϵ remain the same.

With the variable decomposition as in (4.6), the boundary conditions for the variables are

$$
\begin{bmatrix} \hat{p} \\ \hat{T} \\ \hat{u}_i \\ k \\ \epsilon \end{bmatrix} \rightarrow 0 \qquad (4.7)
$$

away from the jet.

Consider now

$$
\frac{\partial \rho \tau_{ij}}{\partial x_j} = \frac{\partial}{\partial x_j} \Big\{ \frac{2}{3} \rho k \delta_{ij} - \rho \nu_t \left(\frac{\partial \hat{u}_i}{\partial x_j} + \frac{\partial \hat{u}_j}{\partial x_i} + \frac{\partial \hat{u}_i^{(a)}}{\partial x_j} + \frac{\partial \hat{u}_j^{(a)}}{\partial x_i} - \frac{2}{3} \frac{\partial \hat{u}_k}{\partial x_k} \delta_{ij} \right) \Big\} \qquad (4.8)
$$

where (4.3) has been used. If $\rho \nu_t$ is locally a constant, using (4.3) and (4.5), (4.8) becomes

$$
\frac{\partial \rho \tau_{ij}}{\partial x_j} = \frac{2}{3} \frac{\partial \rho k}{\partial x_i} \delta_{ij} - \frac{\partial}{\partial x_j} \Big\{ \rho \nu_t \left(\frac{\partial \hat{u}_i}{\partial x_j} + \frac{\partial \hat{u}_j}{\partial x_i} + - \frac{2}{3} \frac{\partial \hat{u}_k}{\partial x_k} \delta_{ij} \right) \Big\} \qquad (4.9)
$$

This means that the diffusion terms are equal to zero away from the jet.

The parabolized equations for $\hat{p}, \hat{T}$ and $\hat{u}_i$ are found by inserting (4.6) into (4.2) and by dropping $\frac{\partial \hat{p}}{\partial x}$ from the $x-$momentum equation, all the $x-$derivative terms in τ_{ij}, τ^s_{ij} and $\hat{\tau}_{ij}$.

$$\rho = \gamma {M_j}^2 \frac{\hat{p} + p^{(a)}}{\hat{T} + T_\infty}$$

$$(\hat{u} + u^{(a)}) \frac{\partial \hat{u}}{\partial x} = -(\hat{v} + v^{(a)}) \frac{\partial \hat{u}}{\partial y} - \hat{w} \frac{\partial \hat{u}}{\partial z} - \hat{u} \frac{\partial u^{(a)}}{\partial x} - \hat{v} \frac{\partial u^{(a)}}{\partial y}$$

$$+ \frac{\rho - \rho_\infty}{\rho \rho_\infty} \frac{\partial p^{(a)}}{\partial x} - \frac{1}{\rho} \Big[\frac{\partial(\rho \hat{\tau}_{xy})}{\partial y} + \frac{\partial(\rho \hat{\tau}_{xz})}{\partial z} \Big]$$

$$(\hat{u} + u^{(a)}) \frac{\partial \hat{v}}{\partial x} = -(\hat{v} + v^{(a)}) \frac{\partial \hat{v}}{\partial y} - \hat{w} \frac{\partial \hat{v}}{\partial z} - \hat{u} \frac{\partial v^{(a)}}{\partial x} - \hat{v} \frac{\partial v^{(a)}}{\partial y} - \frac{1}{\rho} \frac{\partial \hat{p}}{\partial y}$$

$$+ \frac{\rho - \rho_\infty}{\rho \rho_\infty} \frac{\partial p^{(a)}}{\partial y} - \frac{1}{\rho} \Big[\frac{\partial(\rho \hat{\tau}_{yy})}{\partial y} + \frac{\partial(\rho \hat{\tau}_{yz})}{\partial z} \Big]$$

$$(\hat{u} + u^{(a)}) \frac{\partial \hat{w}}{\partial x} = -(\hat{v} + v^{(a)}) \frac{\partial \hat{w}}{\partial y} - \hat{w} \frac{\partial \hat{w}}{\partial z} - \frac{1}{\rho} \frac{\partial \hat{p}}{\partial z} - \frac{1}{\rho} \Big[\frac{\partial(\rho \hat{\tau}_{zy})}{\partial y} + \frac{\partial(\rho \hat{\tau}_{zz})}{\partial z} \Big]$$

$$(\hat{u} + u^{(a)}) \frac{\partial \hat{T}}{\partial x} = -(\hat{v} + v^{(a)}) \frac{\partial \hat{T}}{\partial y} - \hat{w} \frac{\partial \hat{T}}{\partial z} - (\gamma - 1)(\hat{T} + T_\infty) \Big(\frac{\partial \hat{u}}{\partial x} + \frac{\partial \hat{v}}{\partial y} + \frac{\partial \hat{w}}{\partial z} \Big)$$

$$+ \gamma(\gamma - 1) {M_j}^2 \epsilon + \frac{1}{\rho \sigma_T} \Big[\frac{\partial}{\partial y} (\rho \nu_t \frac{\partial \hat{T}}{\partial y}) + \frac{\partial}{\partial z} (\rho \nu_t \frac{\partial \hat{T}}{\partial z}) \Big] \tag{4.10}$$

$$(\hat{u} + u^{(a)}) \frac{\partial k}{\partial x} = -(\hat{v} + v^{(a)}) \frac{\partial k}{\partial y} - \hat{w} \frac{\partial k}{\partial z} - \epsilon - \tau_{xy} \Big(\frac{\partial \hat{u}}{\partial y} + \frac{\partial u^{(a)}}{\partial y} \Big) - \tau_{xz} \frac{\partial \hat{u}}{\partial z}$$

$$- \tau_{yy} \Big(\frac{\partial \hat{v}}{\partial y} + \frac{\partial v^{(a)}}{\partial y} \Big) - \tau_{yz} \frac{\partial \hat{v}}{\partial z} - \tau_{zy} \frac{\partial \hat{w}}{\partial y} - \tau_{zz} \frac{\partial \hat{w}}{\partial z} + \frac{1}{\rho \sigma_k} \Big[\frac{\partial}{\partial y} (\rho \nu_t \frac{\partial k}{\partial y}) + \frac{\partial}{\partial z} (\rho \nu_t \frac{\partial k}{\partial z}) \Big]$$

$$(\hat{u} + u^{(a)}) \frac{\partial \epsilon_s}{\partial x} = - \frac{C_{\epsilon_1} \epsilon_s}{k} \Big[{\tau^s}_{xy} \Big(\frac{\partial \hat{u}}{\partial y} + \frac{\partial u^{(a)}}{\partial y} \Big) + {\tau^s}_{xz} \frac{\partial \hat{u}}{\partial z} + {\tau^s}_{yy} \Big(\frac{\partial \hat{v}}{\partial y} + \frac{\partial v^{(a)}}{\partial y} \Big)$$

$$+ {\tau^s}_{yz} \frac{\partial \hat{v}}{\partial z} + {\tau^s}_{zy} \frac{\partial \hat{w}}{\partial y} + {\tau^s}_{zz} \frac{\partial \hat{w}}{\partial z} \Big] - (\hat{v} + v^{(a)}) \frac{\partial \epsilon_s}{\partial y} - \hat{w} \frac{\partial \epsilon_s}{\partial z}$$

$$- (C_{\epsilon_2} - C_{\epsilon_3} \chi) \frac{{\epsilon_s}^2}{k} + \frac{1}{\rho \sigma_\epsilon} \Big[\frac{\partial}{\partial y} (\rho {\nu^s}_t \frac{\partial \epsilon_s}{\partial y}) + \frac{\partial}{\partial z} (\rho {\nu^s}_t \frac{\partial \epsilon_s}{\partial z}) \Big]$$

$$(\hat{u} + u^{(a)}) \frac{\partial \hat{p}}{\partial x} = -(\hat{u} + u^{(a)}) \frac{\partial p^{(a)}}{\partial x} - (\hat{v} + v^{(a)}) \Big(\frac{\partial \hat{p}}{\partial y} + \frac{\partial \hat{p}^{(a)}}{\partial y} \Big) - \hat{w} \frac{\partial \hat{p}}{\partial z}$$

$$-(\hat{p}+p^{(a)})\Big(\frac{\partial\hat{u}}{\partial x}+\frac{\partial\hat{v}}{\partial y}+\frac{\partial\hat{w}}{\partial z}\Big)+\frac{\rho}{\gamma M_j^2}\Big((\hat{u}+u^{(a)})\frac{\partial\hat{T}}{\partial x}+(\hat{v}+v^{(a)})\frac{\partial\hat{T}}{\partial y}+w\frac{\partial\hat{T}}{\partial z}\Big)$$

where

$$\nu_t = C_\mu\frac{k^2}{\epsilon+\epsilon_0}$$

$$\nu^s{}_t = C_\mu\frac{k^2}{\epsilon_s+\epsilon_0}$$

$$\hat{\tau}_{ij} = -\nu_t\Big(\frac{\partial\hat{u}_i}{\partial x_j}+\frac{\partial\hat{u}_j}{\partial x_i}-\frac{2}{3}\frac{\partial\hat{u}_k}{\partial x_k}\delta_{ij}\Big)+\frac{2}{3}k\delta_{ij}$$

$$\tau_{ij} = -\nu_t\Big(\frac{\partial u_i}{\partial x_j}+\frac{\partial u_j}{\partial x_i}-\frac{2}{3}\frac{\partial u_k}{\partial x_k}\delta_{ij}\Big)+\frac{2}{3}k\delta_{ij}$$

$$\tau^s{}_{ij} = -\nu^s{}_t\Big(\frac{\partial u_i}{\partial x_j}+\frac{\partial u_j}{\partial x_i}-\frac{2}{3}\frac{\partial u_k}{\partial x_k}\delta_{ij}\Big)+\frac{2}{3}k\delta_{ij}$$

$$\text{all}\quad \frac{\partial}{\partial x}\to 0 \quad \text{in} \quad \tau_{ij}, \qquad \tau^s{}_{ij} \quad \text{and} \quad \hat{\tau}^s_{ij}$$

$$\epsilon = \epsilon_s(1+\alpha M_t^2)$$

$$M_t^2 = \frac{2k}{\hat{T}+T^{(a)}}M_j^2$$

$$\chi = -\frac{1}{4}\Big(\frac{k}{\epsilon_s}\Big)^3\Big[\Big(\frac{\partial\hat{v}}{\partial y}+\frac{\partial v^{(a)}}{\partial y}\Big)\Big(\frac{\partial\hat{u}}{\partial y}+\frac{\partial u^{(a)}}{\partial y}\Big)^2+\frac{\partial\hat{w}}{\partial z}\frac{\partial\hat{u}}{\partial z}\frac{\partial\hat{u}}{\partial z}$$
$$+\Big(\frac{\partial\hat{v}}{\partial z}+\frac{\partial\hat{w}}{\partial y}\Big)\Big(\frac{\partial\hat{u}}{\partial y}+\frac{\partial u^{(a)}}{\partial y}\Big)\frac{\partial\hat{u}}{\partial z}\Big]$$

4.3.2. Computation Boundary Conditions for $\hat{p}, \hat{T}$ and $\hat{u}_i$

Outside the jet, $\hat{u}, \hat{v}$ etc are much smaller than $u^{(a)}, v^{(a)}$ etc. Thus it is sufficient to use the linearized equations. The linearized equations are:

$$u^{(a)}\frac{\partial\hat{u}}{\partial x}+v^{(a)}\frac{\partial\hat{u}}{\partial y}+\hat{u}\frac{\partial u^{(a)}}{\partial x}+\hat{v}\frac{\partial u^{(a)}}{\partial y}=0 \qquad (4.11)$$

$$u^{(a)}\frac{\partial \hat{v}}{\partial x}+v^{(a)}\frac{\partial \hat{v}}{\partial y}+\hat{u}\frac{\partial v^{(a)}}{\partial x}+\hat{v}\frac{\partial v^{(a)}}{\partial y}=-\frac{1}{\rho_\infty}\frac{\partial \hat{p}}{\partial y} \tag{4.12}$$

$$u^{(a)}\frac{\partial \hat{w}}{\partial x}+v^{(a)}\frac{\partial \hat{w}}{\partial y}=-\frac{1}{\rho_\infty}\frac{\partial \hat{p}}{\partial z} \tag{4.13}$$

$$u^{(a)}\frac{\partial \hat{T}}{\partial x}+v^{(a)}\frac{\partial \hat{T}}{\partial y}+(\gamma-1)T_\infty\left(\frac{\partial \hat{u}}{\partial x}+\frac{\partial \hat{v}}{\partial y}+\frac{\partial \hat{w}}{\partial z}\right)=0 \tag{4.14}$$

$$u^{(a)}\frac{\partial \hat{p}}{\partial x}+v^{(a)}\frac{\partial \hat{p}}{\partial y}+\hat{u}\frac{\partial p^{(a)}}{\partial x}+\hat{v}\frac{\partial p^{(a)}}{\partial y}+p_\infty\Big(\frac{\partial \hat{u}}{\partial x}+\frac{\partial \hat{v}}{\partial y}+\frac{\partial \hat{w}}{\partial z}\Big)$$

$$-\frac{\rho_\infty T_\infty}{\gamma M_j^2}(\gamma-1)\left(u^{(a)}\frac{\partial \hat{T}}{\partial x}+v^{(a)}\frac{\partial \hat{T}}{\partial y}\right)=0 \tag{4.15}$$

On eliminating $\left(u^{(a)}\frac{\partial \hat{T}}{\partial x}+v^{(a)}\frac{\partial \hat{T}}{\partial y}\right)$ from (4.15) by using (4.14), and making approximation that $u^{(a)}$ and $v^{(a)}$ are locally constants, i.e. $\frac{\partial u^{(a)}}{\partial x}, \frac{\partial u^{(a)}}{\partial y}, \frac{\partial v^{(a)}}{\partial x}, \frac{\partial v^{(a)}}{\partial y} \approx 0$, it is easy to find

$$u^{(a)}\frac{\partial \hat{u}}{\partial x}+v^{(a)}\frac{\partial \hat{u}}{\partial y}=0 \tag{4.16}$$

$$u^{(a)}\frac{\partial \hat{v}}{\partial x}+v^{(a)}\frac{\partial \hat{v}}{\partial y}=-\frac{1}{\rho_\infty}\frac{\partial \hat{p}}{\partial y} \tag{4.17}$$

$$u^{(a)}\frac{\partial \hat{w}}{\partial x}+v^{(a)}\frac{\partial \hat{w}}{\partial y}=-\frac{1}{\rho_\infty}\frac{\partial \hat{p}}{\partial z} \tag{4.18}$$

$$u^{(a)}\frac{\partial \hat{p}}{\partial x}+v^{(a)}\frac{\partial \hat{p}}{\partial y}+\gamma p_\infty\Big(\frac{\partial \hat{u}}{\partial x}+\frac{\partial \hat{v}}{\partial y}+\frac{\partial \hat{w}}{\partial z}\Big)=0 \tag{4.19}$$

From (4.16) the boundary condition for $\hat{u}$ is

$$\frac{\partial \hat{u}}{\partial x}=-\frac{v^{(a)}}{u^{(a)}}\frac{\partial \hat{u}}{\partial y} \tag{4.20}$$

Also,

$$\hat{u}=G(u^{(a)}y-v^{(a)}x,z) \tag{4.21}$$

where G( ) is an arbitrary function.

To solve equations (4.17), (4.18) and (4.21), let us introduce a potential function ϕ determined by

$$\frac{\partial\phi}{\partial y} = \hat{v}, \quad \frac{\partial\phi}{\partial z} = \hat{w}, \quad p = -\rho_\infty\Big(u^{(a)}\frac{\partial\phi}{\partial x} + v^{(a)}\frac{\partial\phi}{\partial y}\Big) \tag{4.22}$$

(4.22) satisfies (4.17) and (4.18) identically. The governing equation for ϕ is obtained by substituting (4.22) into (4.19)

$$\Big(u^{(a)}\frac{\partial}{\partial x} + v^{(a)}\frac{\partial}{\partial y}\Big)^2\phi - a_\infty^2\Big(\frac{\partial\hat{u}}{\partial x} + \frac{\partial^2\phi}{\partial y^2} + \frac{\partial^2\phi}{\partial z^2}\Big) = 0 \tag{4.23}$$

On finding the asymptotic solution of (4.23) and making use of (4.22) (see Appendix B), one finds the following boundary conditions outside the jet,

$$\begin{aligned}
&u^{(a)}\frac{\partial\hat{u}}{\partial x} + v^{(a)}\frac{\partial\hat{u}}{\partial y} = 0\\
&\Big[u^{(a)}\frac{\partial}{\partial x} + v^{(a)}\frac{\partial}{\partial y} + \frac{a_\infty}{\sqrt{y^2+z^2}}\Big(z\frac{\partial}{\partial z} + y\frac{\partial}{\partial y} + \frac{1}{a_\infty}\Big)\Big]\begin{bmatrix}\hat{p}\\ \hat{T}\end{bmatrix} = 0\\
&u^{(a)}\frac{\partial\hat{w}}{\partial x} + v^{(a)}\frac{\partial\hat{w}}{\partial y} + \frac{a_\infty}{\sqrt{y^2+z^2}}\Big[z\frac{\partial\hat{w}}{\partial z} + y\frac{\partial\hat{w}}{\partial y} + \Big(1 - \frac{z^2}{y^2+z^2}\Big)\hat{w}\\
&\qquad - \frac{yz}{y^2+z^2}(\hat{v} - \frac{v^{(a)}}{u^{(a)}}\hat{u})\Big] + \frac{\hat{w}}{\sqrt{y^2+z^2}} = 0\\
&u^{(a)}\frac{\partial\hat{v}}{\partial x} + v^{(a)}\frac{\partial\hat{v}}{\partial y} + \frac{a_\infty}{\sqrt{y^2+z^2}}\Big[z\frac{\partial\hat{v}}{\partial z} + y\frac{\partial\hat{v}}{\partial y} + \Big(1 - \frac{y^2}{y^2+z^2}\Big)(\hat{v} - \frac{v^{(a)}}{u^{(a)}}\hat{u})\\
&\qquad - \frac{yz}{y^2+z^2}\hat{w}\Big] + \frac{\hat{v} - \frac{v^{(a)}}{u^{(a)}}\hat{u}}{\sqrt{y^2+z^2}} = 0
\end{aligned} \tag{4.24}$$

4.4. Mean Flow Refraction and Reflection from the Wing

To account for reflection from the wing and mean flow refraction effect on the radiated sound, the adjoint Green's function method from Chapter 3 is generalized for installed jets. As discussed in Chapter 3, the locally parallel flow approximation is a reasonable assumption for the jet flow. Two adjoint Green's functions need to be considered. One is for the part of the jet downstream of the trailing edge of the flap. For this Green's function, there is no solid surface to be taken into account. The free jet flow is assumed to extend to infinity in the upward direction. The other is for the part of the jet upstream of the flap trailing edge. For this Green's function the wing/flap forms a solid boundary of the problem.

4.4.1. Adjoint Green's Function Formulation

Let $\bar{u}(y,z)$, $\bar{\rho}(y,z)$ and $\bar{p}(y,z)$ be the mean flow velocity, density and pressure distribution of a jet. Let us consider the time harmonic adjoint Green's function, denoted by a subscript 'a'. Under the assumption of locally parallel mean flow, the equations for the adjoint Green's function are (see ref. [25]):

$$
\begin{aligned}
-i\omega\overline{\rho}u_a - \bar{\rho}\ \overline{u}\frac{\partial u_a}{\partial x} - \gamma\overline{p}\frac{\partial p_a}{\partial x} &= 0 \\
-i\omega\overline{\rho}v_a - \overline{\rho}\ \overline{u}\frac{\partial v_a}{\partial x} + \overline{\rho}u_a\frac{\partial \overline{u}}{\partial y} - \gamma\overline{p}\frac{\partial p_a}{\partial y} - (\gamma-1)p_a\frac{\partial \overline{p}}{\partial y} &= 0 \\
-i\omega\overline{\rho}w_a - \overline{\rho}\ \overline{u}\frac{\partial w_a}{\partial x} + \overline{\rho}u_a\frac{\partial \overline{u}}{\partial z} - \gamma\overline{p}\frac{\partial p_a}{\partial z} - (\gamma-1)p_a\frac{\partial \overline{p}}{\partial z} &= 0 \qquad (4.25) \\
-i\omega p_a - \overline{u}\frac{\partial p_a}{\partial x} - \left(\frac{\partial u_a}{\partial x} + \frac{\partial v_a}{\partial y} + \frac{\partial w_a}{\partial z}\right) &= \frac{1}{2\pi}\delta(\mathbf{x}-\mathbf{x_o})
\end{aligned}
$$

where $\mathbf{x_o}$ is the far field observation point at which jet noise is to be measured.

Outside the jet and the open wind tunnel $\bar{u}$ is zero. It is straightforward to find from (4.25) that p_a satisfies equation (3.21) and the solution is given by (3.22). Let us use the spherical coordinate system shown in Figure 3.1. The far field solution is almost identical to (3.23). The adjoint Green's function, as $R \to \infty$, is

$$\begin{bmatrix} u_a \\ v_a \\ w_a \\ p_a \end{bmatrix} = \frac{-i\omega}{8\pi^2 a_\infty^2 R} \begin{bmatrix} a_\infty \cos\Theta \\ a_\infty \sin\Theta\cos\phi \\ a_\infty \sin\Theta\sin\phi \\ 1 \end{bmatrix} e^{\frac{i\omega}{a_\infty}\left(R - x\cos\Theta - \sin\Theta\cos\phi y - \sin\Theta\sin\phi z\right)} \tag{4.26}$$

In the absence of the jet and under the parallel flow approximation, the mean flow is a function of y alone i.e. $\bar{u} = \bar{u}(y), \bar{\rho} = \bar{\rho}(y), \bar{p} = \bar{p}(y)$. The solution of (4.25) corresponding to an incident wave in the form of (4.26) is

$$\begin{bmatrix} u_a \\ v_a \\ w_a \\ p_a \end{bmatrix} = \begin{bmatrix} \hat{u}_a(y) \\ \hat{v}_a(y) \\ \hat{w}_a(y) \\ \hat{p}_a(y) \end{bmatrix} e^{\frac{i\omega}{a_\infty}\left(R - x\cos\Theta - \sin\Theta\sin\phi z\right)} \tag{4.27}$$

By substitution of (4.27) into (4.25) it is straightforward to derive,

$$\hat{u}_a = \frac{\bar{a}^2 \cos\Theta}{(a_\infty - \overline{u}\cos\Theta)} \hat{p}_a \tag{4.28}$$

$$\hat{w}_a = \frac{\bar{a}^2 \sin\Theta\sin\phi}{(a_\infty - \overline{u}\cos\Theta)} \hat{p}_a \tag{4.29}$$

$$\frac{d\hat{p}_a}{dy} = \frac{-i\omega}{\bar{a}^2}\left(1 - \frac{\bar{u}}{a_\infty}\cos\Theta\right)\hat{v}_a + \left[\frac{\cos\Theta}{(a_\infty - \overline{u}\cos\Theta)}\frac{\partial \bar{u}}{\partial y} - \frac{(\gamma-1)}{\gamma\bar{p}}\frac{\partial \bar{p}}{\partial y}\right]\hat{p}_a \tag{4.30}$$

$$\frac{d\hat{v}_a}{dy} = i\omega\left[\frac{\bar{a}^2(1 - \sin^2\Theta\cos^2\phi)}{a_\infty(a_\infty - \overline{u}\cos\Theta)} - (1 - \frac{\bar{u}}{a_\infty\cos\Theta})\right]\hat{p}_a \tag{4.31}$$

Outside the jet, $\bar{u} = 0, \bar{a} = a_\infty, \bar{p} = p_\infty$, (4.30) and (4.31) become

$$\frac{d\hat{p}_a}{dy} = \frac{-i\omega}{a_\infty^2}\hat{v}_a \tag{4.32}$$

$$\frac{d\hat{v}_a}{dy} = -i\omega\sin^2\Theta\cos^2\phi\hat{p}_a$$

The solution of (4.32) corresponding to the incoming wave is

$$\hat{p}_a^i = \frac{-i\omega}{8\pi^2 a_\infty^2 R} e^{-i\frac{\omega}{a_\infty}\sin\Theta\cos\phi y} \tag{4.33a}$$

$$\hat{v}_a^i = \frac{-i\omega a_\infty \sin\Theta\cos\phi}{8\pi^2 a_\infty^2 R} e^{-i\frac{\omega}{a_\infty}\sin\Theta\cos\phi y}$$

where superscript 'i' denotes the incoming wave.

Solution (4.32) matches (4.26). Another solution of (4.32) is the reflected wave

$$\hat{p}_a^r = Ae^{-i\frac{\omega}{a_\infty}\sin\Theta\cos\phi y} \tag{4.33b}$$

$$\hat{v}_a^r = -Aa_\infty \sin\Theta\cos\phi e^{-i\frac{\omega}{a_\infty}\sin\Theta\cos\phi y}$$

Case (i) Downstream of the flap trailing edge.

We will assume that the free jet extends to $y = \infty$ downstream of the trailing edge of the flap, as shown in the Figure 4.4.

At $y = \infty, \bar{u} = u_f, \bar{a} = a_f, \bar{p} = p_f$. It is easy to find the solution of (4.30) and (4.31)

$$\hat{p}_a^t = e^{i\frac{\omega}{a_f}\left[\frac{a_f^2}{a_\infty^2}(\sin^2\Theta\cos^2\phi - 1) + (1 - \frac{u_f}{a_\infty}\cos^2\Theta)^2\right]^{\frac{1}{2}} y} \tag{4.34}$$

$$\hat{v}_a^t = -a_f \frac{\left[\frac{a_f^2}{a_\infty^2}(\sin^2\Theta\cos^2\phi - 1) + (1 - \frac{u_f}{a_\infty}\cos^2\Theta)^2\right]^{\frac{1}{2}}}{(1 - \frac{u_f}{a_\infty}\cos^2\Theta)}$$

$$\times e^{i\frac{\omega}{a_f}\left[\frac{a_f^2}{a_\infty^2}(\sin^2\Theta\cos^2\phi - 1) + (1 - \frac{u_f}{a_\infty}\cos^2\Theta)^2\right]^{\frac{1}{2}} y}$$

where superscript 't' indicates a transmitted wave.

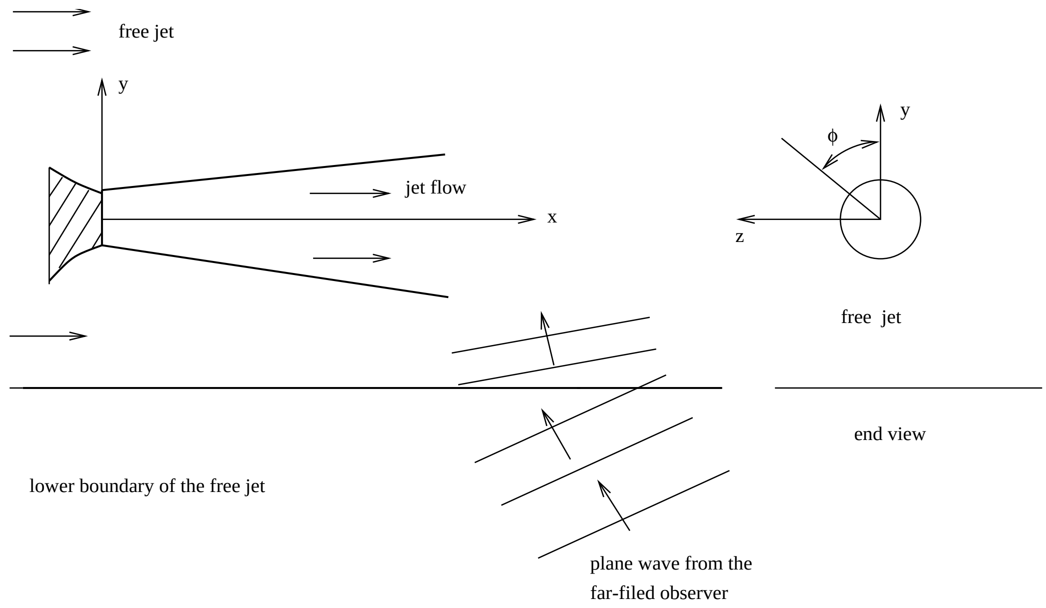

Figure 4.4. Sound scattering problem in the region downstream of the trailing edge of the flap.

In the absence of the jet, the incident wave inside and outside the free jet may be found in three steps:

• Integrate equations (4.30) and (4.31) numerically using (4.33a) as the starting value. Let the solution at $y = \infty$ be $\hat{p}_a = p_1, \hat{v}_a = v_1$.

• Integrate equations (4.30) and (4.31) numerically using (4.33b) as the starting value with $A = 1$. Let the numerical solution at $y = \infty$ be $\hat{p}_a = p_2, \hat{v}_a = v_2$.

At $y = \infty$ the total solution must match the transmitted wave of (4.34). Thus

$$p_1 + Ap_2 = B\hat{p}_a^t \tag{4.35}$$

$$v_1 + Av_2 = B\hat{v}_a^t$$

• Solve (4.35) for A and B to find the entire wave.

Case (ii) Upstream of the flap trailing edge.

Let (n_x, n_y) be the components of the normal on the bottom side of the wing or flap. The boundary condition on the surface of the wing/flap is (see ref. [25])

$$u_a n_x + v_a n_y = 0 \tag{4.36}$$

Equations (4.25) to (4.31) are applicable to the region upstream of the flap trailing edge as well. u_a is related to p_a by (4.28). Therefore the boundary condition (4.36) may be rewritten as

$$\frac{\bar{a}^2 \cos\Theta}{(a_\infty - \overline{u}\cos\Theta)}\hat{p}_a n_x + \hat{v}_a n_y = 0 \tag{4.37}$$

Outside the free jet the incident and reflected waves are given by (4.33a) and (4.33b). In the absence of the jet, the adjoint Green's function satisfies equations (4.30) and (4.31). To find the adjoint Green's function inside the open wind tunnel the following steps may be taken:

• Use (4.33a) as the starting solution and integrate (4.30) and (4.31) numerically, using the solution outside the open wind tunnel as starting value, all the way to the wing/flap. let the solution at the wall be $\hat{p}_a = p_3, \hat{v}_a = v_3$.

• Put $A = 1$ in (4.33b) and use this as the starting solution to integrate (4.30) and (4.31) as in step one until the wall is reached. Let the solution at the wall be denoted by a subscript 4, $\hat{p}_a = p_4, \hat{v}_a = v_4$.

The total solution at the wall is

$$\hat{p}_a = p_3 + Ap_4 \tag{4.38}$$

$$\hat{v}_a = v_3 + Av_4$$

(4.38) must satisfy boundary condition (4.37). Therefore

$$A = -\frac{v_3 n_y + \frac{\bar{a}^2 \cos\Theta n_x p_3}{a_\infty (1 - \frac{\bar{u}}{a_\infty}\cos\Theta)}}{v_4 n_y + \frac{\bar{a}^2 \cos\Theta n_x p_4}{a_\infty (1 - \frac{\bar{u}}{a_\infty}\cos\Theta)}} \tag{4.39}$$

at $y = y_{wall}$

With A determined, the adjoint Green's function is known inside and outside the open wind tunnel.

4.4.2. Numerical Implementation

Under the assumption of the locally parallel flow approximation the solution must have the same $x-$dependence as the incident wave. In other words the approximation (3.24) is valid. By factoring out $e^{-i\frac{\omega}{a_\infty}\cos\Theta x}$ and replacing $-i\omega$ by $\frac{\partial}{\partial t}$ in equations (4.25) to make the equations time dependent, the adjoint Green's function problem becomes a two-dimensional sound scattering problem. The governing equations are

$$\frac{\partial \tilde{v}_a}{\partial t} + \frac{i\omega\overline{u}\cos\Theta}{a_\infty}\tilde{v}_a + \left[\frac{\partial \overline{u}}{\partial y}\frac{\cos\Theta \;\; \bar{a}^2}{(a_\infty - \overline{u}\cos\Theta)} - \frac{\gamma - 1}{\bar{\rho}}\frac{\partial \bar{p}}{\partial y}\right]\tilde{p}_a = \bar{a}^2\frac{\partial \tilde{p}_a}{\partial y}$$

$$\frac{\partial \tilde{w}_a}{\partial t} + \frac{i\omega\overline{u}\cos\Theta}{a_\infty}\tilde{w}_a + \left[\frac{\partial \overline{u}}{\partial z}\frac{\cos\Theta \;\; \bar{a}^2}{(a_\infty - \overline{u}\cos\Theta)} - \frac{\gamma - 1}{\bar{\rho}}\frac{\partial \bar{p}}{\partial z}\right]\tilde{p}_a = \bar{a}^2\frac{\partial \tilde{p}_a}{\partial z} \tag{4.40}$$

$$\frac{\partial \tilde{p}_a}{\partial t} + \frac{i\omega\overline{u}\cos\Theta}{a_\infty}\tilde{p}_a + \frac{i\omega}{a_\infty}\frac{\cos^2\Theta \;\; \overline{a}^2}{(a_\infty - \overline{u}\cos\Theta)}\tilde{p}_a - \frac{\partial}{\partial y}\tilde{v}_a - \frac{\partial}{\partial z}\tilde{w}_a = 0$$

The incident waves are

$$
\begin{aligned}
p &= (p_1 + Ap_2)e^{\frac{i\omega}{a_\infty}\left(R - \sin\Theta \sin\phi z - a_\infty t\right)} \\
v &= (v_1 + Av_2)e^{\frac{i\omega}{a_\infty}\left(R - \sin\Theta \sin\phi z - a_\infty t\right)} \\
w &= (w_1 + Aw_2)e^{\frac{i\omega}{a_\infty}\left(R - \sin\Theta \sin\phi z - a_\infty t\right)}
\end{aligned}
\tag{4.41}
$$

in the region downstream of the trailing edge of the flap and

$$
\begin{aligned}
p &= (p_3 + Ap_4)e^{\frac{i\omega}{a_\infty}\left(R - \sin\Theta \sin\phi z - a_\infty t\right)} \\
v &= (v_3 + Av_4)e^{\frac{i\omega}{a_\infty}\left(R - \sin\Theta \sin\phi z - a_\infty t\right)} \\
w &= (w_3 + Aw_4)e^{\frac{i\omega}{a_\infty}\left(R - \sin\Theta \sin\phi z - a_\infty t\right)}
\end{aligned}
\tag{4.42}
$$

upstream of the trailing edge of the flap.

For a given $\bar{u}(y,z), \bar{\rho}(y,z)$ and $\bar{p}(y,z)$ the sound scattering problem may be solved computationally. For this purpose, (4.40) is discretized according to the 7-point stencil DRP scheme in a rectangular computational domain as shown in Figure 4.5. The upper boundary of the computational domain, y_{top} is taken to be $7D$ in the region downstream of the trailing edge of the flap, and $y_{top} = y_{wing}$ upstream of the trailing edge of the flap. The lower boundary and the width of the computational domain are taken to be $y_{bottom} = 11D, w = 14D$ respectively. This choice assures that waves with Strouhal number greater or equal to 0.05 have at least one wavelength inside the computational domain.

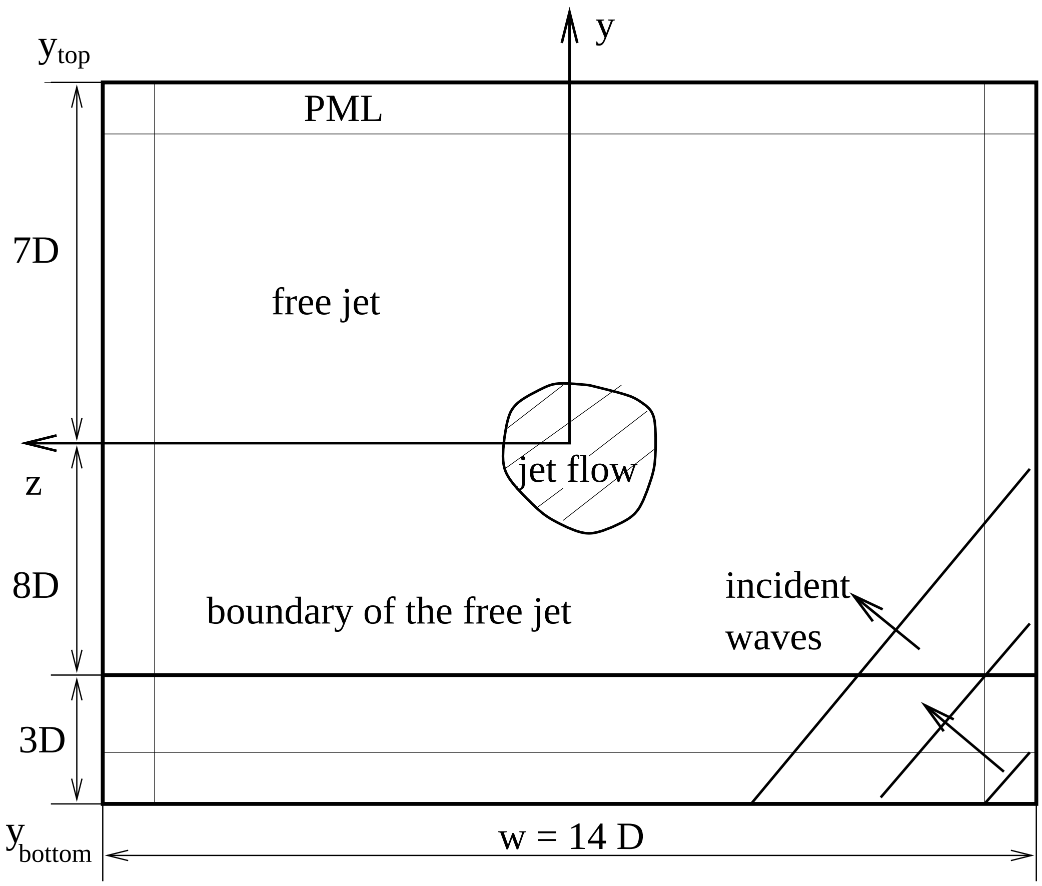

Figure 4.5. Computational domain showing the jet flow, free jet, incident sound wave and the perfectly matched layer (PML) in the region downstream of the trailing edge of the flap.

The free jet is approximated by a Gaussian profile with core length $8D$ and half width $0.7D$. The mesh size is set by the smaller of two criteria. To ensure the DRP scheme has sufficient spatial resolution for the incident and the scattered acoustic waves, no fewer than 7 mesh spacings per acoustic wavelength is used. That is, a finer mesh is automatically used for high frequency waves. To make certain that the refraction of sound by the mixing layer of the jet is accurately computed, a minimum of 8 mesh spacings is used per half-width of the layer. To eliminate spurious numerical waves that may inadvertently be generated at the boundaries of the computational domain, artificial selective damping terms [59], [60] are added to the discretized equations. The artificial selective damping terms damp the short waves without affecting the physical (long) waves. The inverse mesh Reynolds number of the damping terms is given a value of 0.05.

As shown in Figure 4.5, the computational domain is surrounded by a perfectly matched layer (PML). The PML has a thickness of 15 mesh points. In this layer the flow variables are split into two parts: the split variable method [61]. One part of the variables will be assigned the values of the incident wave given by (4.41) and (4.42). The other part is the scattered waves. The scattered waves are damped by the built-in damping of the PML. The layer is called perfectly matched because, in principle, there is no reflected wave back into the computation domain. The construction of the PML is discussed in the Appendix A.

For a given direction of radiation and frequency, the incident wave (4.41) and (4.42)is completely specified. To start the computation, initial conditions are required. In this work, the incident wave is used as the starting condition. The solution is marched in time until a time periodic state is attained. At this time, the maximum absolute value of $\tilde{p}_a$ over a cycle is measured at every point in the jet. This is the absolute value of the adjoint Green's function $|p_a|$ needed for noise computation. The wall boundary condition (4.37) is enforced by the means of the ghost point method [33].

4.5. Calculated Far Field Noise Spectra

Once the mean flow velocity, k and ϵ turbulence quantities and the adjoint Green's function are computed, all of these quantities are substituted into equations (1.1) and (1.2). On performing the volume integration over the noise source region, the radiated noise spectrum in the far field is obtained.

The first step in implementing formula (1.1) and (1.2) is to compute the mean flow using equations (4.10) with the boundary conditions (4.24). To start the calculation at the nozzle exit, it is assumed that the mean flow is surrounded by a thin mixing layer with a Gaussian profile. The half-width of the mixing layer is taken to be 1.5% to 2% of the nozzle diameter. A Mach 0.9 hot jet with the temperature ratio 2.8 is used to model the coaxial jet in the Boeing experiment [30-32].

As expected from Figure 4.3a, in the case of a wing with the flap angle of deflection 0^o, the installed jet differs very little from an isolated circular jet. Due to the positive pressure gradient in the y direction, the installed jet is slightly shifted upward compared to the isolated jet as shown in the Figure 4.6.

Figure 4.7 shows the computed contours of axial velocity component of the installed jet with the flap deployed at 23^o (typical take-off configuration). The contours clearly show the tendency to become more and more nonaxisymmetric. Figures 4.7c and 4.7d show that the jet bends down relative to the jet axis due to the wing/flap induced downwash. This agrees with the experimental observations [30]. Figure 4.8 gives the comparison between levels of k of isolated and installed jets at $x = 5D$ (near the trailing edge of the flap). It is evident that the presence of the wing and flap increases the turbulence intensity. These effects become even more pronounced in the case of the flap deployed at 35^o (typical landing configuration).

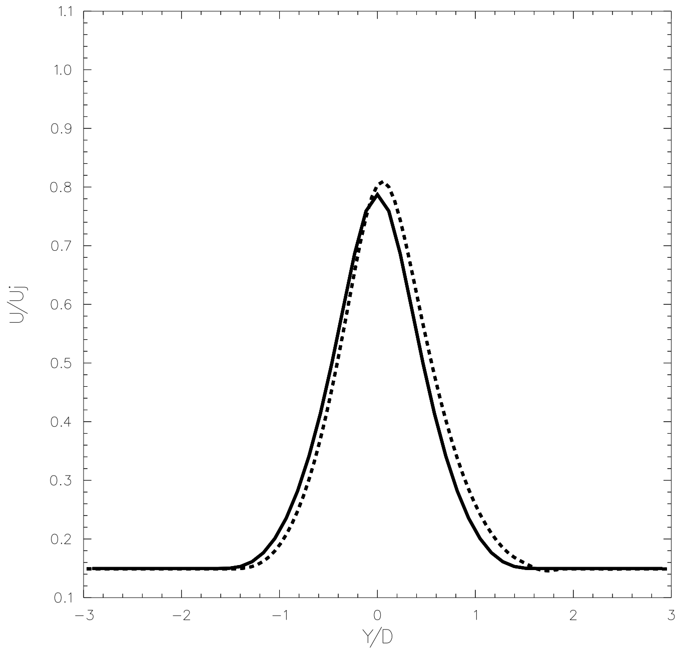

Figure 4.6. Radial velocity profiles. Comparison between isolated jet and the jet in the presence of the wing with flap deflection angle $0^o . x/D = 10.0, Z/D = 0, M_j = 0.9, M_f = 0.2, Tr/T_\infty = 2.8$. ——— isolated jet, - - - - - - - installed jet.

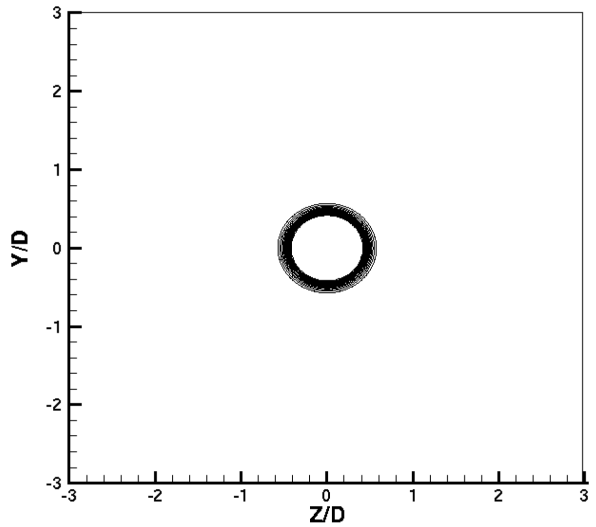

Figure 4.7a. Contours of the axial velocity component of a Mach 0.9, $Tr/T_\infty = 2.8$. installed jet, flap deflection angle 23^o. $M_f = 0.2$. a. $x/D = 1$, b. $x/D = 5$, c. $x/D = 10$, d. $x/D = 20$.

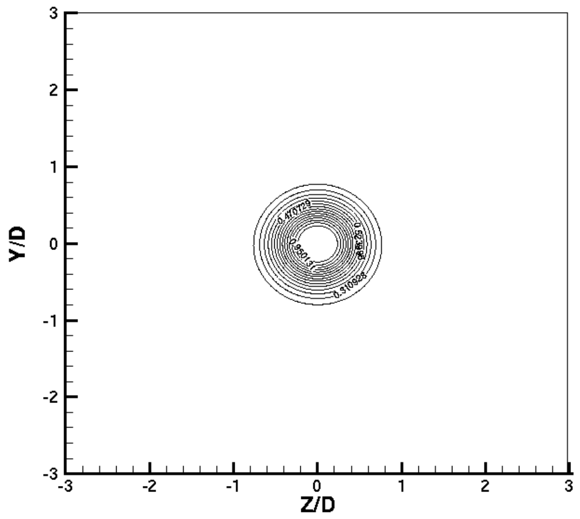

Figure 4.7b. $X/D = 5$.

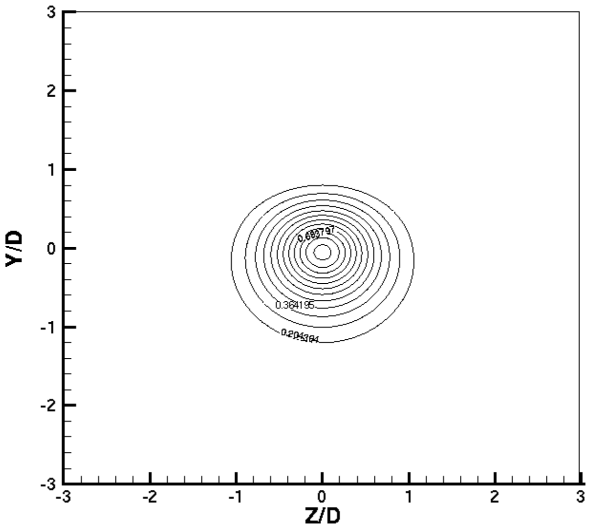

Figure 4.7c. $X/D = 10$.

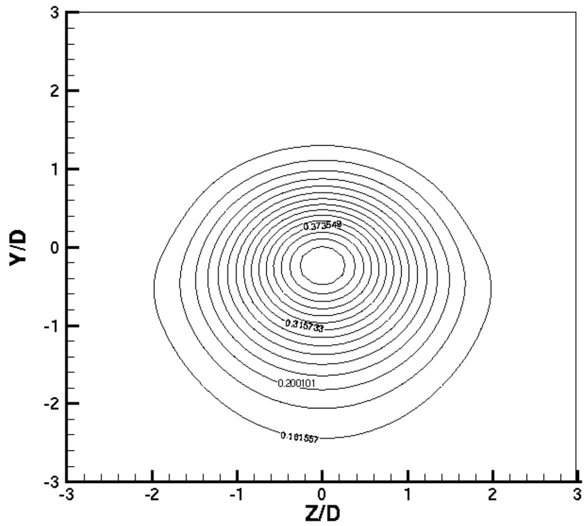

Figure 4.7d. $X/D = 20$.

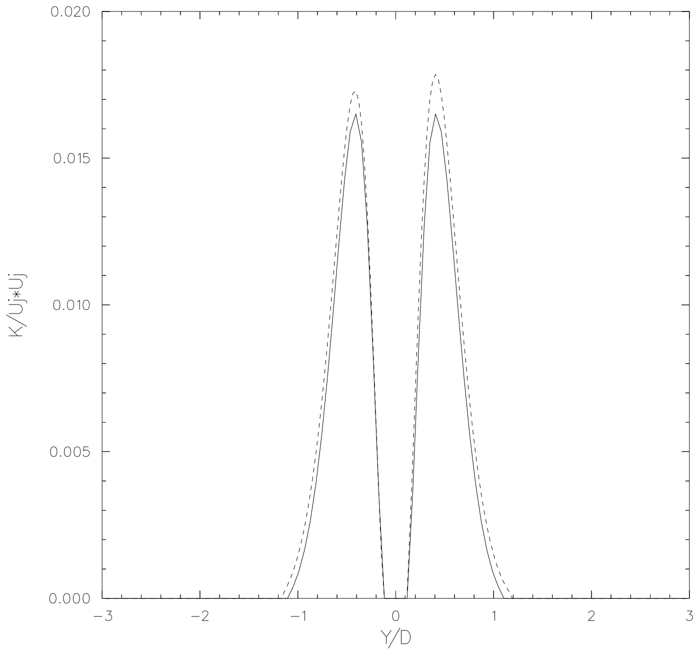

Figure 4.8. Radial profiles of k/u_j^2 Comparison between isolated and installed jets. $M_j = 0.9$, $Tr/T_\infty = 2.8$. $x/D = 5$, $Z/D = 0$. Flap deflection angle 23^o. $M_f = 0.2$. ———— isolated jet, - - - - - - - installed jet.

Figure 4.9 shows calculated noise spectra for the Mach 0.9 jet at a temperature ratio 2.8. The azimuthal angle of the measurement microphone is ϕ is 180^o. There are four curves in the figure. The full curve is the noise spectrum for the isolated jet, the dotted curve is the for the installed jet with the flap deployed at 0^o, the dashed curve is the noise spectrum for the installed jet with the flap deployed at 23^o and the last curve is for the installed jet with the flap at 35^o. Figure 4.9a is the spectra measured in the fly-over plane ($\Theta = 90^o$). Figure 4.9b is the noise radiated in the upstream direction ($\Theta = 120^o$). Figure 4.9c is the noise radiated in the downstream direction ($\Theta = 60^o$). It is quite clear that the noise from installed jets is greatly increased at high frequencies. The noise increase follows monotonically with increasing flap deflection angle. The installation noise dominates in the upstream direction.

Figure 4.10 is for the same jet as Figure 4.9. Here $\Theta = 90^o, \phi = 150^o$. Since the isolated jet is axisymmetric, the full curve in Figure 4.10 is the the same as in Figure 4.9. It is clear that the installed jet is nonaxisymmetric with more noise radiated in $\phi = 150^o$ plane.

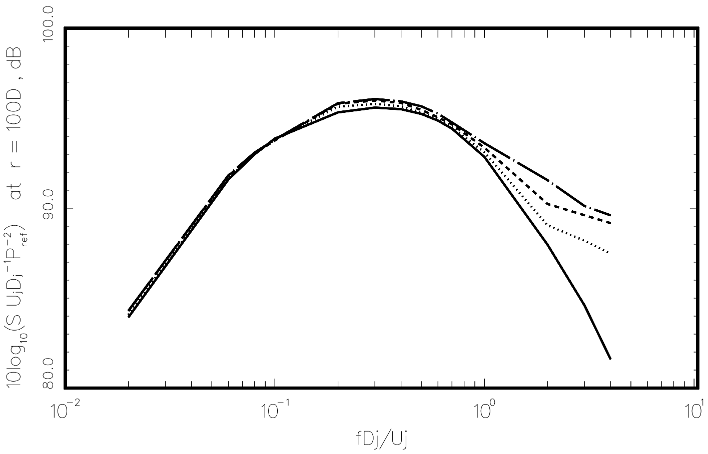

Figure 4.9a. Computed noise spectra of a Mach 0.9, $T_r/T_\infty = 2.8$ jet. $\phi = 180.0^0$. ———— Isolated jet, ... installed jet, flap deflection angle 0^o, - - - - - - - installed jet, flap deflection angle 23^o, — · — · — · — installed jet, flap deflection angle 35^o. a. $\Theta = 90^o$, b. $\Theta = 120^o$, c. $\Theta = 60^o$.

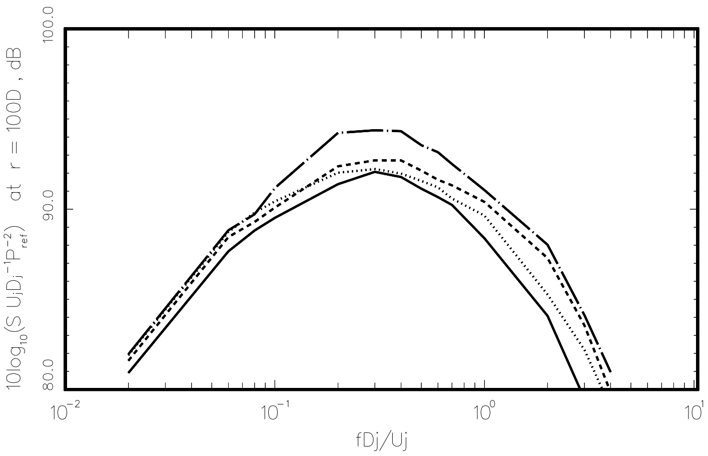

Figure 4.9b. $\Theta = 120^o$.

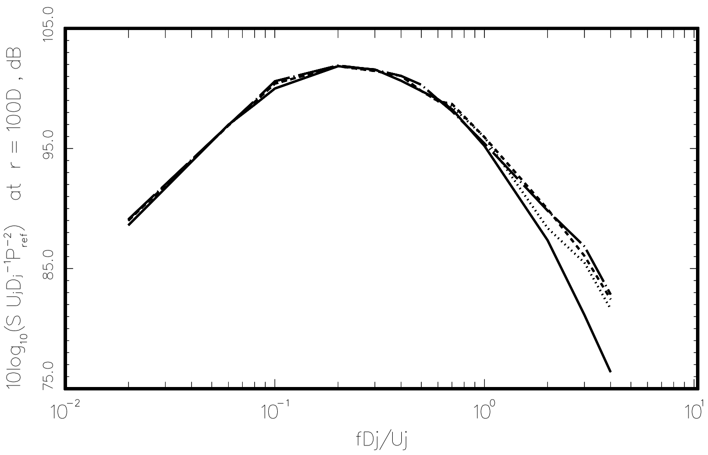

Figure 4.9c. $\Theta = 60^o$.

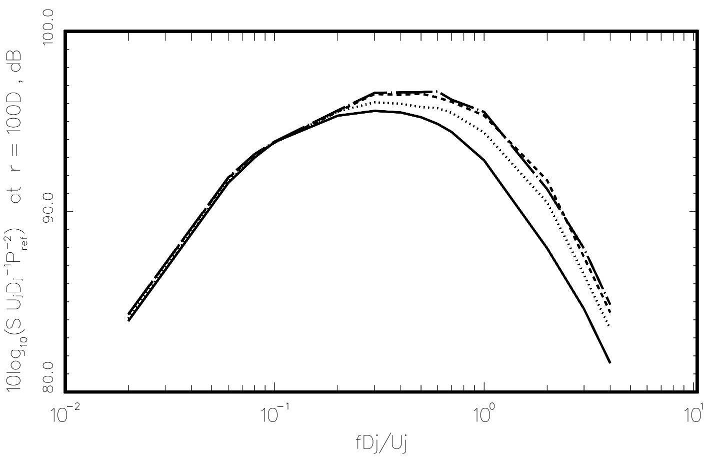

Figure 4.10. Computed noise spectra of a Mach 0.9, $T_r/T_\infty = 2.8$ jet. $\Theta = 90^o, \phi = 150^o$. ———— Isolated jet, ... installed jet, flap deflection angle 0^o, - - - - - - - installed jet, flap deflection angle 23^o, — · — · — · — installed jet, flap deflection angle 35^o.

The jet model that was tested in the Boeing experiment, simulated exhaust geometry of a typical separated flow modern engine with an area ratio 3 and bypass ratio of about 6. Most engines have a small engine cooling vent flow exhausting on the outer surface of the primary nozzle. The flow for this stream was obtained by bleeding a small percentage of primary flow through throttling holes. In contrast, the installed jet model employed in this work, uses a single circular nozzle to model the jet. Therefore it is deemed inappropriate to compare the absolute noise levels of calculated and measured noise spectra. However, the computational model predicts accurately the main installation effects observed in the experiment. The noise increase follows monotonically with increasing flap deflection angle, there is more installed noise in the upstream direction, the installed jet noise is nonaxisymmetric with more noise radiated in $\phi = 150^o$ direction. Also, the △ decibel changes between noise levels at different flap settings agree well with measurements at high Strouhal numbers, Figure 4.11. At low frequencies the experimental data also show an increase in the noise levels, Figure 4.12. It is believed that the low frequency installed noise is generated by the interaction of the large turbulence structures of the jet flow and the flap. The present model considers only the noise from fine-scale turbulence and, therefore, can not reproduce the increase in low frequency noise of installed jets.

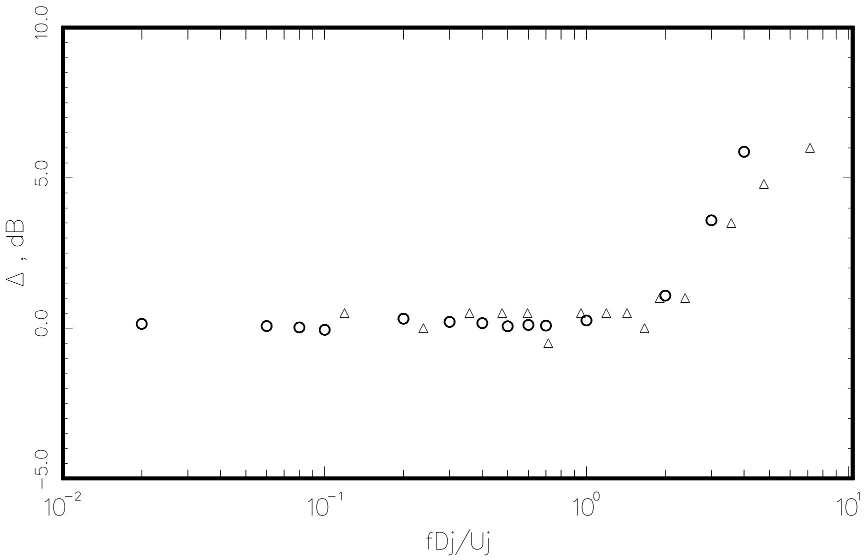

Figure 4.11. Increase in the noise levels due to installation for a Mach 0.9, $T_r/T_\infty = 2.8$ jet. $\Theta = 90^o$, $\phi = 180.0^o$. Flap deflection angle 0^o. ∘ Model prediction, △ data from the experiment [30].

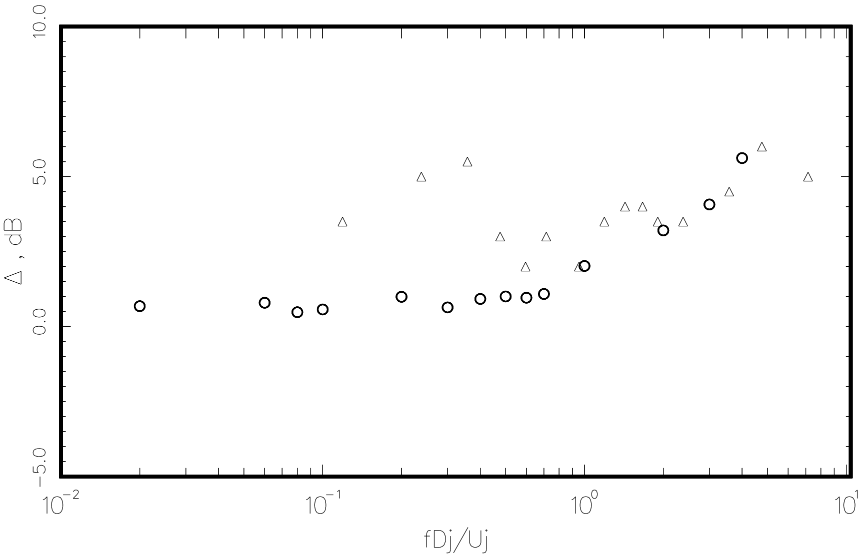

Figure 4.12. Increase in the noise levels due to installation for a Mach 0.9, $T_r/T_\infty = 2.8$ jet. $\Theta = 120^o$, $\phi = 180.0^o$. Flap deflection angle 23^o. $\circ$ Model prediction, $\triangle$ data from the experiment [30].

CHAPTER V

SUMMARY AND CONCLUSIONS

In this work, the effects of simulated forward flight on high speed jet noise from fine-scale turbulence is investigated theoretically. The investigation is systematic, including the effects on the jet mean flow, the jet turbulence, the noise source distribution, as well as the far-field noise spectra in the sideline directions. Comparisons with experimental measurements are carried out in every step, limited only by the lack of data in the literature. Overall, very favorable agreements between theoretical predictions and experiments are found, suggesting that the basic theoretical framework is valid and that the model theory contains the essential physics of sound generation by turbulent shear flow.

The present study finds that forward flight can lead to significant reduction in jet turbulence intensity and noise source strength. This, in turn, leads to considerable reduction in the radiated noise. The reduction is nearly uniform across the entire frequency range of the spectrum. This is important in perceived noise level computation, which is used for aircraft certification.

From the point of view of noise suppression, knowledge of the location of the dominant sources of the jet noise is important. The present investigation reveals that forward flight can move the noise sources over some distance downstream. Any development of a noise suppression device must take this into consideration if it is to remain effective at takeoffs and landings.

The semi-empirical jet noise theory of Tam and Auriault is extended to nonaxisymmetric jets. A set of improved boundary conditions for the parabolized RANS equations is developed. This new set of boundary conditions makes it possible to compute the jet mean flow and the $k - \epsilon$ turbulence quantities using a smaller computation domain. The adjoint Green's function needed to account for mean flow refraction effect is reformulated into the solution of a two-dimensional acoustic scattering problem. It is demonstrated that the solution can be found accurately and efficiently by time marching the solution to a periodic state by the DRP scheme. Good agreements are found between computed noise spectra and experimental measurements.

As a part of the present investigation, a large number of nonaxisymmetric jet noise spectra in the $\Theta = 90^o$ plane have been examined. It appears that the spectra are nearly independent of the azimuthal angle. In the 90^o plane, there is no noise source convection effect as well as mean flow refraction effect. Thus, it appears that fine-scale turbulence noise, by itself, is quite isotropic. In other words, the noise sources behave like monopoles.

For noise radiated in the downstream direction, the nonaxisymmetric mean flow exerts a strong influence on the noise spectrum. For instance, in the case of a rectangular or elliptic jet with large aspect ratio, there is a much thicker shear layer on the smaller dimension sides of the jet. Refraction by the shear layer, reduces the radiation of high frequency sound. This immediately leads to a nonaxisymmetric sound field (at a fixed polar angle) with more noise radiated in the minor axis plane. This is borne out in both the numerical results and experimental measurements.

A mathematical/computational model for prediction of the radiated fine-scale turbulence noise of the installed jets is developed. Parabolized RANS equations are reformulated and modified to compute the turbulent jet flow with the wing/flap flow as the boundary condition outside the jet. A set of boundary conditions for installed jets is developed. The jet noise theory of Tam and Auriault is extended to installed jets. The adjoint Green's function, accounting for mean flow refraction and reflection from the wing, is reformulated into the solution of a two-dimensional acoustic scattering problem. The solution can be found by time marching the variables to a periodic state.

The noise spectra are calculated for various flap settings. The proposed installed jet model captures accurately the main installation effects. The noise increase follows monotonically with increasing flap deflection angle, there is more installed noise in the upstream direction, the installed jet noise is nonaxisymmetric. Good agreement is found between relative levels of computed noise spectra and experimental measurements at hight frequencies. At low frequencies the agreement is not good. It is believed that the low frequency installed noise is generated by the interaction of the large turbulence structures of the jet flow and the flap. The present model considers only the noise from fine-scale turbulence and, therefore, can not reproduce the increase in low frequency noise of installed jets.

APPENDIX A

PERFECTLY MATCHED LAYER ABSORBING BOUNDARY CONDITIONS

Berenger [12] invented the perfectly matched layer (PML) as absorbing boundary condition for computational electromagnetics. Hu [22] applied the idea to acoustic problems. Tam, Auriault and Cambuli [49] showed that in the case of Euler equations with flow normal to the perfectly matched layer, the PML equations have unstable solutions that can, however, be stabilized by the addition of appropriate artificial selective damping. In all the works mentioned, the waves are nondispersive. Equation (3.25) of the adjoint Green's function, however, supports dispersive waves. The purpose of this appendix is to show how a PML absorbing boundary condition can be formulated that will absorb all outgoing dispersive waves of equation (3.25). Furthermore, it will be shown that the PML equations are stable.

Outside the jet, $\bar{u} = 0, \bar{\rho} = \rho_\infty$, equation (3.25) reduces to,

$$\frac{\partial \tilde{v}_a}{\partial t} - \gamma p_\infty \frac{\partial \tilde{p}_a}{\partial y} = 0 \qquad (A.1)$$

$$\frac{\partial \tilde{w}_a}{\partial t} - \gamma p_\infty \frac{\partial \tilde{p}_a}{\partial z} = 0 \qquad (A.2)$$

$$\frac{\partial \tilde{p}_a}{\partial t} + i\omega \cos^2\theta \tilde{p}_a - \frac{1}{\rho_\infty}\left(\frac{\partial \tilde{v}_a}{\partial y} + \frac{\partial \tilde{w}_a}{\partial z}\right) = 0 \qquad (A.3)$$

Let us look for plane wave solutions of (A.1) to (A.3) in the form,

$$\begin{bmatrix} \tilde{v}_a \\ \tilde{w}_a \\ \tilde{p}_a \end{bmatrix} = \begin{bmatrix} \hat{v} \\ \hat{w} \\ \hat{p} \end{bmatrix} e^{i(\alpha y+\beta z-\Omega t)} \tag{A.4}$$

By substitution of (A.4) into (A.1) to (A.3), it is easy to find

$$\hat{v} = -\frac{\alpha}{\Omega}\gamma p_\infty \hat{p} \tag{A.5}$$

$$\hat{w} = -\frac{\beta}{\Omega}\gamma p_\infty \hat{p} \tag{A.6}$$

$$\left(1 - \frac{\omega \cos^2\Theta}{\Omega}\right)\hat{p} + \frac{1}{\rho_\infty}\left(\frac{\alpha}{\Omega}\right)\hat{v} + \frac{1}{\rho_\infty}\left(\frac{\beta}{\Omega}\right)\hat{w} = 0 \tag{A.7}$$

(A.5) to (A.7) are homogeneous equations. For nontrivial solution, the determinant of the coefficient matrix of these equations, when written in a matrix form, must be equal to zero. This gives the dispersion relation that may be simplified to

$$\Omega^2 - \omega\Omega\cos^2\Theta - a_\infty^2(\alpha^2+\beta^2) = 0 \tag{A.8}$$

For a wave of a given frequency Ω, its wavenumbers, which are often referred to as the eigenvalues of the homogeneous system, are given by the roots of (A.8). On solving (A.8) for α, one finds

$$\alpha_\pm = \pm\frac{(\Omega^2 - \omega\Omega\cos^2\Theta - a_\infty^2\beta^2)^{\frac{1}{2}}}{a_\infty} \tag{A.9}$$

By differentiating (A.8) and use (A.9), the group velocity of the acoustic wave in the $x-$direction is found,

$$\frac{\partial\Omega}{\partial\alpha} = \pm\frac{2a_\infty(\Omega^2 - \omega\Omega\cos^2\Theta - a_\infty^2\beta^2)^{\frac{1}{2}}}{2\Omega - \omega\cos^2\Theta} \tag{A.10}$$

The $\pm$ sign in (A.10) corresponds to $\alpha_{\pm}$. Now the group velocity is a function of frequency or wavenumber. Hence, the waves are dispersive.

For $\Omega > 0$, in order that $\alpha_{\pm}$ are real (propagating waves), Ω must be larger than $\omega\cos^2\Theta$. That is the denominator of (A.10) is positive. Thus α_{+} is the left propagating wave (negative group velocity). For $\Omega < 0$, it is the other way around. In other words, for right propagating wave, we have $\frac{\alpha}{\Omega} > 0$ and $\frac{\alpha}{\Omega} < 0$ for left propagating wave.

Now let us consider perfectly matched layer (1) of Figure 3.2. On following standard PML formulation, the governing equations and variables in the layer (1) are:

$$\tilde{v}_a = v_1, \qquad \tilde{w}_a = w_2, \qquad \tilde{p}_a = p_1 + p_2 \tag{A.11}$$

$$\frac{\partial v_1}{\partial t} + \sigma v_1 - \gamma p_\infty \frac{\partial (p_1 + p_2)}{\partial y} = 0 \tag{A.12}$$

$$\frac{\partial w_2}{\partial t} - \gamma p_\infty \frac{\partial (p_1 + p_2)}{\partial z} = 0 \tag{A.13}$$

$$\frac{\partial p_1}{\partial t} + \sigma p_1 - \frac{1}{\rho_\infty}\frac{\partial v_1}{\partial y} = 0 \tag{A.14}$$

$$\frac{\partial p_2}{\partial t} + i\omega\cos^2\theta(p_1 + p_2) - \frac{\partial w_2}{\partial z} = 0 \tag{A.15}$$

Plane wave solutions of (A.12) to (A.15) that match the frequency and traverse wavenumbers of wave solution (A.4) of the adjoint equations at the PML interface have the form

$$\begin{bmatrix} v_1 \\ w_2 \\ p_1 \\ p_2 \end{bmatrix} = \begin{bmatrix} \hat{v}_1 \\ \hat{w}_2 \\ \hat{p}_1 \\ \hat{p}_2 \end{bmatrix} e^{i(\kappa y + \beta z - \Omega t)} \tag{A.16}$$

By substitution of (A.16) into (A.12) to (A.15), it is straightforward to derive,

$$\hat{v}_1 = -\frac{\kappa}{(\Omega + i\sigma)}\gamma p_\infty(\hat{p}_1 + \hat{p}_2) \tag{A.17}$$

$$\hat{w}_2 = -\frac{\beta}{\Omega}\gamma p_\infty(\hat{p}_1 + \hat{p}_2) \qquad (A.18)$$

$$\left(1 - \frac{\omega \cos^2\Theta}{\Omega}\right)(\hat{p}_1 + \hat{p}_2) + \frac{1}{\rho_\infty}\frac{\kappa}{(\Omega + i\sigma)}\hat{v} + \frac{1}{\rho_\infty}\left(\frac{\beta}{\Omega}\right)\hat{w} = 0 \qquad (A.19)$$

Just as in the case of algebraic system (A.5) to (A.7), (A.17) to (A.19) for an eigenvalue problem with κ as the eigenvalue. On comparing the two eigenvalue systems, it is clear that they are identical; same eigenvalue and eigenfunction. The wavenumbers of the two problems are related by

$$\frac{\alpha}{\Omega} = \frac{\kappa}{\Omega + i\sigma}$$

or

$$\kappa = \alpha + i\sigma\frac{\alpha}{\Omega} \qquad (A.20)$$

The fact that the eigenfunctions of the two system are the same allows the incident wave to be completely transmitted without reflection at the PML interface. The transmitted wave has the $y-$dependence of the form

$$e^{i\kappa y} = e^{i\alpha y - \sigma\frac{\alpha}{\Omega y}} \qquad (A.21)$$

Since $\frac{\alpha}{\Omega} > 0$ for the right propagating wave, the transmitted wave is damped as it propagates through the PML.

Finally, to show that the PML equations are stable, it is easy to find that the dispersion relation of equations (A.11) to (A.15) is

$$F \equiv \left(\Omega^2 - \omega\Omega\cos^2\Theta - \frac{a_\infty^2\kappa^2\Omega^2}{(\Omega + i\sigma)}\right) = a_\infty^2\beta^2 \qquad (A.22)$$

It can be shown using the definition of F defined by (A.22) that the upper half Ω-plane is mapped into the entire complex $F-$plane except the positive real axis.

Since $a_\infty^2\beta^2 > 0$, the right side of (A.22) is real and positive, it follows that there is no solution of (A.22) with Ω in the upper half $\Omega-$plane. This ensures that the system of PML equations has no unstable solution.

APPENDIX B

BOUNDARY CONDITIONS FOR INSTALLED JETS

In (4.23) $\hat{u}$ is known, given by(4.21). The solution of (4.23) consists of two parts, the homogeneous and the nonhomogeneous solution. The nonhomogeneous equation (4.23) may be rewritten as

$$\Big(u^{(a)}\frac{\partial}{\partial x}+v^{(a)}\frac{\partial}{\partial y}\Big)^2\phi-a_\infty^2\Big(\frac{dG(u^{(a)}y-v^{(a)}x,z)}{dx}+\frac{\partial^2\phi}{\partial y^2}+\frac{\partial^2\phi}{\partial z^2}\Big)=0 \qquad (B.1)$$

Let

$$\phi=\tilde{\phi}+\frac{v^{(a)}}{u^{(a)2}}\int^{u^{(a)}y-v^{(a)}x}G(\xi)d\xi \qquad (B.2)$$

where $\tilde{\phi}$ is the homogeneous solution. By substitution of (B.2) into (B.1) it is easy to find

$$\Big(u^{(a)}\frac{\partial}{\partial x}+v^{(a)}\frac{\partial}{\partial y}\Big)^2\tilde{\phi}-a_\infty^2\Big(\frac{\partial^2\tilde{\phi}}{\partial y^2}+\frac{\partial^2\tilde{\phi}}{\partial z^2}\Big)=0 \qquad (B.3)$$

and

$$\hat{v}=\frac{\partial\tilde{\phi}}{\partial y}+\frac{v^{(a)}}{u^{(a)2}}\hat{u} \qquad (B.4)$$

$$\hat{w}=\frac{\partial\tilde{\phi}}{\partial z} \qquad (B.5)$$

$$\hat{p}=-\rho_\infty\left(u^{(a)}\frac{\partial\tilde{\phi}}{\partial x}+v^{(a)}\frac{\partial\tilde{\phi}}{\partial y}\right) \qquad (B.6)$$

To find the asymptotic solution of (B.3), let us make a change of variables.

$$\xi=x,\qquad \eta=-\frac{v^{(a)}}{u^{(a)2}}x+y,\qquad z=z \qquad (B.7)$$

Thus (B.3) becomes

$$(u^{(a)})^2\frac{\partial^2\tilde{\phi}}{\partial\xi^2}-a_\infty^2\Big(\frac{\partial^2\tilde{\phi}}{\partial\eta^2}+\frac{\partial^2\tilde{\phi}}{\partial z^2}\Big)=0 \qquad (B.8)$$

Let $R^2=\eta^2+z^2$, (B.8) may be rewritten in the form

$$(u^{(a)})^2\frac{\partial^2\tilde{\phi}}{\partial\xi^2}-a_\infty^2\Big(\frac{\partial^2\tilde{\phi}}{\partial R^2}+\frac{1}{R}\frac{\partial\tilde{\phi}}{\partial R}\Big)=0 \qquad (B.9)$$

For large $R, \tilde{\phi}$ of (B.9) is given by

$$\tilde{\phi}=\frac{F(\xi-\frac{u^{(a)}}{a_\infty}R)}{R^{\frac{1}{2}}}+... \qquad (B.10)$$

By substituting (B.10) into (B.6), it is straightforward to find

$$\hat{p}=-\rho_\infty u^{(a)}\frac{F'\left(x-\frac{u^{(a)}}{a_\infty}\sqrt{(y-\frac{v^{(a)}}{u^{(a)}}x)^2+z^2}\right)}{\sqrt{(y-\frac{v^{(a)}}{u^{(a)}}x)^2+z^2}} \qquad (B.11)$$

By means of the above formula it is easy to find

$$u^{(a)}\frac{\partial\hat{p}}{\partial x}+v^{(a)}\frac{\partial\hat{p}}{\partial y}+a_\infty\left[\frac{z}{\sqrt{(y-\frac{v^{(a)}}{u^{(a)}}x)^2+z^2}}\frac{\partial\hat{p}}{\partial z}+\frac{(y-\frac{v^{(a)}}{u^{(a)}}x)}{\sqrt{(y-\frac{v^{(a)}}{u^{(a)}}x)^2+z^2}}\frac{\partial\hat{p}}{\partial y}\right]+$$

$$\frac{\hat{p}}{\sqrt{(y-\frac{v^{(a)}}{u^{(a)}}x)^2+z^2}}=0 \qquad (B.12)$$

(B.12) is the boundary condition for $\hat{p}$. Since the assumption $u^{(a)}, v^{(a)}$ are constant is not exactly true, it is recommended to use the following instead

$$\Big[u^{(a)}\frac{\partial}{\partial x}+v^{(a)}\frac{\partial}{\partial y}+\frac{a_\infty}{\sqrt{y^2+z^2}}\Big(z\frac{\partial}{\partial z}+y\frac{\partial}{\partial y}+\frac{1}{a_\infty}\Big)\Big]\hat{p}=0 \qquad (B.13)$$

By substituting (B.3), (B.4), (B.5) and (B.6) into (4.14), one finds

$$u^{(a)}\frac{\partial\hat{T}}{\partial x}+v^{(a)}\frac{\partial\hat{T}}{\partial y}+\frac{(\gamma-1)T_\infty}{a_\infty}\left(u^{(a)}\frac{\partial\tilde{\phi}}{\partial x}+v^{(a)}\frac{\partial\tilde{\phi}}{\partial y}\right)=0 \qquad (B.14)$$

Or $\hat{T} \sim \tilde{\phi}$. Therefore $\hat{T}$ satisfies the same boundary condition (B.13) as $\hat{p}$.

Since $\tilde{\phi}$ and $\hat{p}$ have the same form, $\tilde{\phi}$ also satisfies (B.13) i.e.

$$\Big[u^{(a)}\frac{\partial}{\partial x} + v^{(a)}\frac{\partial}{\partial y} + \frac{a_\infty}{\sqrt{y^2+z^2}}\Big(z\frac{\partial}{\partial z} + y\frac{\partial}{\partial y} + \frac{1}{a_\infty}\Big)\Big]\tilde{\phi} = 0 \qquad (B.15)$$

By differentiating (B.15) with respect to z, and making use of (B.4) and (B.5), it is easy to find

$$u^{(a)}\frac{\partial \hat{w}}{\partial x} + v^{(a)}\frac{\partial \hat{w}}{\partial y} + \frac{a_\infty}{\sqrt{y^2+z^2}}\Big[z\frac{\partial \hat{w}}{\partial z} + y\frac{\partial \hat{w}}{\partial y} + \Big(1 - \frac{z^2}{y^2+z^2}\Big)\hat{w}$$

$$-\frac{yz}{y^2+z^2}(\hat{v} - \frac{v^{(a)}}{u^{(a)}}\hat{u})\Big] + \frac{\hat{w}}{\sqrt{y^2+z^2}} - \frac{z\tilde{\phi}}{(y^2+z^2)^{3/2}} = 0 \qquad (B.16)$$

The last term can be dropped, as it is a higher order term. The boundary condition for $\hat{w}$ is

$$u^{(a)}\frac{\partial \hat{w}}{\partial x} + v^{(a)}\frac{\partial \hat{w}}{\partial y} + \frac{a_\infty}{\sqrt{y^2+z^2}}\Big[z\frac{\partial \hat{w}}{\partial z} + y\frac{\partial \hat{w}}{\partial y} + \Big(1 - \frac{z^2}{y^2+z^2}\Big)\hat{w}$$

$$-\frac{yz}{y^2+z^2}(\hat{v} - \frac{v^{(a)}}{u^{(a)}}\hat{u})\Big] + \frac{\hat{w}}{\sqrt{y^2+z^2}} = 0 \qquad (B.17)$$

By differentiating (B.15) with respect to y and proceeding as above, one finds

$$u^{(a)}\frac{\partial \hat{v}}{\partial x} + v^{(a)}\frac{\partial \hat{v}}{\partial y} + \frac{a_\infty}{\sqrt{y^2+z^2}}\Big[z\frac{\partial \hat{v}}{\partial z} + y\frac{\partial \hat{v}}{\partial y} + \Big(1 - \frac{y^2}{y^2+z^2}\Big)(\hat{v} - \frac{v^{(a)}}{u^{(a)}}\hat{u})$$

$$-\frac{yz}{y^2+z^2}\hat{w}\Big] + \frac{\hat{v} - \frac{v^{(a)}}{u^{(a)}}\hat{u}}{\sqrt{y^2+z^2}} = 0 \qquad (B.18)$$

REFERENCES

[1] Smith, M. J. T., *Aircraft Noise*, Cambridge University Press, 1989.

[2] Lighthill, M.J., "Jet Noise," *AIAA Journal*, Vol. 1, no. 7, 1963, pp. 1507–1517.

[3] Lombardo, D., *Advanced Aircraft Systems*, McGraw-Hill, 1993.

[4] Tam, C.K.W., "Supersonic Jet Noise," *Annual Review of Fluid Mechanics*, Vol. 27, 1995, pp. 17–43.

[5] Tam, C.K.W., "Jet Noise Generated by Large-Scale Coherent Motion," *Aeroacoustics of Flight Vehicles: Theory and Practice, Vol. 1: Noise Source*, ed. Hubbard, H.H., NASA RP-1258, 1991, pp. 311-390.

[6] Tam, C.K.W., and Tanna, H.K., "Shock Associated Noise of Supersonic Jets from Convergent-Divergent Nozzles," *Journal of Sound and Vibration*, Vol. 81, no. 3, 1982, pp. 337–358.

[7] Tam, C.K.W., Seiner, J.M., and Yu, J.C., "On the Relationship Between Broadband Shock Associated Noise and Screech Tones," *AIAA Paper 84-2276*, 1984.

[8] Lighthill, M.J. "On Sound Generated Aerodynamically: I. General Theory," *Proc. Roy. Soc. London Ser. A,* 211, 1952, pp. 564-581.

[9] Lighthill, M.J. "On Sound Generated Aerodynamically: II. Turbulence as a Source of Sound," *Proc. Roy. Soc. London Ser. A,* 222, 1954, pp. 1-32.

[10] Lilley, G.M. "Jet Noise Classical Theory and Experiments," In *Aeroacoustics of Flight Vehicles: Theory and Practice,* Vol. 1, ed. H.H. Hubbard, 1991, pp.211-289. NASA RP-1258.

[11] Tam, C.K.W. "Jet Noise Generated by Large-Scale Coherent Motion," In *Aeroacoustics of Flight Vehicles: Theory and Practice,* Vol. 1, ed. H.H. Hubbard, 1991, pp.311-390. NASA RP-1258.

[12] Berenger, J.P., "A Perfectly Matched Layer for the Absorption of Electro-

magnetic Waves", *Journal of Computational Physics,* Vol. 114, 1994, pp. 185-200.

[13] Tam, C.K.W. "Jet Noise: Since 1952," *Theoret. Comput. Fluid Dynamics,* 10, 1998, pp. 393-405.

[14] Brown, G.L. & Roshko, A. "On Density Effects and Large Structure in Turbulent Mixing Layers," *J. Fluid Mech.,* 64, 1974, pp. 775-816.

[15] Crow, S.C. & Champagne, F.H. "Orderly Structure in Jet Turbulence," *J. Fluid Mech.,* 48, 1971, pp. 547-591.

[16] Tam, C.K.W. & Burton, D.E. "Sound Generated by Instability Waves of Supersonic Flows Part 2: Axisymmetric Jets," *J. Fluid Mech.,* 138, 1984, pp. 249-295.

[17] Troutt, T.R., and McLaughlin, D.K. "Experiments on the Flow and Acoustic Properties of a Moderate Reynolds Number Supersonic Jet," *J. Fluid Mech.,* 116, 1982, pp. 123-156.

[18] Tam, C.K.W. & Chen, P. "Turbulent Mixing Noise from Supersonic Jets," *AIAA Journal,* 32, 1994, pp. 1774-1780.

[19] Dahl, M.D., Papamoschu, D. & Hixon, R. "Supersonic Coaxial Jets: Noise Predictions and Measurements," AIAA Paper 98-2294, 1998.

[20] Tam, C.K.W., Golebiowski, M. & Seiner, J.M. "On the Two Components of Turbulent Mixing Noise from Supersonic Jets," AIAA Paper 96-1716, May 1996.

[21] Tam, C.K.W. "Influence of Nozzle Geometry on the Noise of High-Speed Jets," *AIAA Journal,* Vol. 36, No. 8, 1998, pp. 1396-1400.

[22] Hu, F.Q., "On Absorbing Boundary Conditions for Linearized Euler Equations by a Perfectly Matched layer", *Journal of Computational Physics,* Vol. 129, 1996, pp. 201-219.

[23] Tam, C.K.W., and Auriault, L., "Jet Mixing Noise from Fine Scale Turbulence," *AIAAJournal*, Vol. 37. No. 2, 1999, pp. 145-153.

[24] Thies, A.T. and Tam, C.K.W., "Computation of Turbulent Axisymmetric and Nonaxisymmetric Jet Flows using the $k-\epsilon$ Model," *AIAA Journal,* Vol. 34, No.2, Feb. 1996, pp. 309-316.

[25] Tam, C.K.W., and Auriault, L., "Mean Flow Refraction Effects on Sound Radiated from Localized Sources in a Jet," *Journal of Fluid Mechanics,* Vol. 370, 1998, pp. 149-174.

[26] Redy, N.N. & Tanna, H.K. 1980 "Installation Effects on Jet Noise in Flight," AIAA Paper 80-1044.

[27] Wang,M.E. "Wing Effect on Jet Noise Propagation," AIAA Paper 80-1047, 1980.

[28] Stevens, R.C.K., Bryce, W.D. & Szewczyk, V.M. "Model and Full-Scale Studies of the Exhaust Noise From a Bypass Engine in Flight," AIAA Paper 83-0751, 1983.

[29] Mead, C.J. & Strange, P.J.R. "Under-Wing Installation Effects on Jet Noise at Sideline," AIAA Paper 98-2208, 1998.

[30] Shivashankara, B.N. & Blackner, A.M. "Installed Jet Noise", AIAA Paper 97-1601, 1997.

[31] Bhat, T.R.C. & Blackner, A.M. "Installed Jet Noise Prediction Model for Coaxial Jets," AIAA Paper 98-0079, 1998.

[32] Blackner, A.M. & Bhat, T.R.C. "Installation Effects on Coaxial Jet Noise - an Experimental Study," AIAA Paper 98-0080, 1998.

[33] Kurbatskii, K.A. and Tam, C.K.W. "Cartesian Boundary Treatment of Curved Walls for High-Order Computational Aeroacoustics Finite Difference Schemes," *AIAA Journal,* Vol. 35, pp. 133-140, January 1997.

[34] Tanna, H.K., and Morris, P.J., "In-Flight Simulation Experiments on Turbulent Jet Mixing Noise," *Journal of Sound and Vibration,* Vol. 53, 1977, pp. 389-405.

[35] Larson, R. S., McColgan, C.J., and Packman, A.B., "Jet Noise Source Modification Due to Forward Flight," *AIAA Journal,* Vol. 16, No. 3, 1978, pp. 225-232.

[36] Yu, J.C., and Dixon, N.R., "Experimental Study of Sound Radiation from Subsonic Jet in Simulated Motion," *AIAA Journal,* Vol. 18, No. 4, 1980, pp. 427-443.

[37] Tam, C.K.W., Fang, J., and Kurbatskii, K.A. "Nonhomogeneous Radiation

and Outflow Boundary Conditions Simulating Incoming Acoustic and Vorticity Waves for Exterior Computational Aeroacoustics Problems", *International J. Numer. Methods in Fluids,* Vol. 26, pp. 1107-1123, 1998.

[38] Cocking, B.J., "A Prediction Method for the Effects of Flight on Subsonic Jet Noise," *Journal of Sound and Vibration,* Vol. 53, 1977, pp. 435-453.

[39] Stone, J.R., "On the Use of Relative Velocity Exponents for Jet Engine Exhaust Noise," NASA TM 78873, 1978.

[40] Michalke, A., and Michel, U., "Relation Between Static and In-Flight Directivities of Jet Noise," *Journal of Sound and Vibration,* Vol. 63, 1979, pp. 602-605.

[41] Michalke, A., and Michel, U., "Prediction of jet Noise from Static Tests," *Journal of Sound and Vibration,* Vol. 67, 1979, pp. 341-367.

[42] Tam, C.K.W. and Webb, J.C., "Dispersion-Relation-Preserving Finite Difference Schemes for Computational Acoustics," *Journal of Computational Physics,* Vol. 107, Aug. 1993, pp. 262-281.

[43] Plumblee, H.E., "Effects of Forward Velocity on Turbulent Jet Mixing Noise," NASA CR-2702, 1976.

[44] Lau, J.C., "A Study of the Structure of the Coannular Jet," Lockheed-Georgia Co., Rept. LG80 ER0017, Marietta, GA, 1980.

[45] Morris, P.J., "Turbulence Measurements in Subsonic and Supersonic Axisymmetric Jets in a Parallel Stream," *AIAA Journal,* Vol. 14, No. 10, 1976, pp. 1468-1475.

[46] Tanna, H.K., Tester, B.J., and Lau, J.C., "The Noise and Flow Characteristics of Inverted-Profile Coannular Jets," NASA CR-158995, 1979.

[47] Fisher, M.J., Harper-Bourne, M., and Glegg, S.A.L., "Jet Engine Noise Source Location: the Polar Correlation Technique,", *AIAA Journal,* Vol. 51, 1977, pp. 23-54.

[48] Tester, B.J., and Fisher, M.J., "Engine Noise Source Breakdown: Theory, Simulation and Results," AIAA Paper 81-2040, Oct. 1981.

[49] Tam, C.K.W., Auriault, L. and Cambuli, F., "Perfectly matched Layer as an Absorbing Boundary Condition for the Linearized Euler Equations in Open

and Ducted Domains," *Journal of Computational Physics,* Vol. 144, 1998, pp. 213-234.

[50] Goldstein, M.E., "The Low Frequency Sound from Multipole Sources in Axisymmetric Shear Flows," *Journal of Fluid Mechanics,* Vol. 70, 1975, pp. 595-604.

[51] Goldstein, M.E., "The Low Frequency Sound from Multipole Sources in Axisymmetric Shear Flows, Part 2" *Journal of Fluid Mechanics,* Vol. 75, 1976, pp. 17-28.

[52] Balsa, T.F., "The Far Field of High Frequency Convected Singularities in Sheared Flows with an Application to jet Noise Prediction," *Journal of Fluid Mechanics,* Vol. 74, 1976, pp. 193-208.

[53] Goldstein, M.E., "High Frequency Sound Emission from Moving Point Multipole Sources Embedded in Arbitrary Transversely Sheared Mean Flows," *Journal of Sound and Vibration,* Vol. 80, 1982, pp. 499-522.

[54] Durbin, P.A., "High Frequency Green's Function for Aerodynamic Noise in Moving Media, Part I: General Theory," *Journal of Sound and Vibration,* Vol. 91, 1983, pp. 519-525.

[55] Durbin, P.A., "High Frequency Green's Function for Aerodynamic Noise in Moving Media, Part II: Noise from a Spread Jet," *Journal of Sound and Vibration,* Vol. 91, 1983, pp. 529-538.

[56] Khavaran, A. and Krejsa, E.A. "Propagating of High Frequency Jet Noise Using Geometric Acoustics," AIAA paper 93-0147, 1993.

[57] Khavaran, A. and Krejsa, E.A. "Refraction of High Frequency jet Noise in an Arbitrary Jet Flow," AIAA paper 94-0139, 1994.

[58] Khavaran, A., "Role of Anisotropy in Turbulent Mixing Noise," *AIAA Journal,* Vol. 37, July 1999, pp. 832-841.

[59] Tam, C.K.W., "Computational Aeroacoustics: Issues and Methods," *AIAA Journal,* Vol. 33, Oct 1995, pp. 1788-1796.

[60] Tam, C.K.W., Webb, J.C. and Dong, Z., "A Study of the Short Wave Components in Computational Acoustics," *Journal of Computational Acoustics,* Vol. 1, Mar. 1993, pp. 1-30.

[61] Tam, C.K.W., "Advances in Numerical Boundary Conditions for Computational Aeroacoustics," *Journal of Computational Acoustics,* Vol. 6, Dec. 1998, pp. 377-402.

[62] Seiner, J.M., Ponton, M.K., Jansen, B.J., and Lagen, N.T., "The Effects of Temperature on Supersonic Jet Noise Emission," AIAA Paper 92-2046, May 1992.

[63] Tam, C.K.W. and K.B.M.Q. Zaman, "Subsonic Jet Noise from Non-Axisymmetric and Tabbed Nozzles," AIAA Journal, Vol. 38, No. 4, 2000, pp. 592-599.

[64] Way, D.J. and Turner, B.A., "Model Tests Demonstrating Under-Wing Installation Effects on Engine Exhaust Noise," AIAA Paper 80-1048, AIAA 6^{th} Aeroacoustics Conference, Hartford, Connecticut, June 1980.

[65] Sengupta, G., "Analysis of Jet-Airplane Interaction Noise," AIAA Paper 83-0783, AIAA 8^{th} Aeroacoustics Conference, Atlanta, Georgia, April 1983.

[66] Miller, W.R., "Flight Effects for Jet-Airframe Interaction Noise," IAA Paper 83-0784, AIAA 8^{th} Aeroacoustics Conference, Atlanta, Georgia, April 1983.

[67] Brown, W.H. and Ahuja, K.K., "Jet and Wing/Flap Interaction Noise," IAA Paper 84-2362, AIAA/NASA 9^{th} Aeroacoustics Conference, Williamsburg, Virginia, October 1984.

[68] Norum, T.D., and Brown, M.C., "Simulated High Speed Flight Effects on Supersonic Jet Noise," AIAA Paper 93-4388, Oct. 1993.

BIOGRAPHICAL SKETCH

Nikolai N. Pastouchenko was born on March 09, 1972 in Kostroma, Russia. He received a Master's degree in Applied Mathematics from Moscow Engineering Physics Institute in February, 1996. He entered the Florida State University in the Summer of 1996, receiving a Ph.D. in Applied and Computational Mathematics in October, 2001.